The Dynamic Response of a 3D Mussel Dropper in Waves

The construction of a 3D numerical model for a series of connected pendulums

K.E. Huijgen

Delft University of Technology

TUDelft

Deltares

The Dynamic Response of a 3D Mussel Dropper in Waves

The construction of a 3D numerical model for a series of connected pendulums

by

K.E. Huijgen

to obtain the degree of Master of Science in Marine Technology
at the Delft University of Technology,
to be defended publicly on Thursday February 15, 2024 at 14:00.

An electronic version of this thesis is available at `https://repository.tudelft.nl/`.

Cover: https://essentialsmagazine.com.au/category/food-tech/

TUDelft

Abstract

Offshore mussel cultivation is gaining popularity, with the longline technique emerging as a popular method for cultivation. The longline technique entails multiple backbones from which mussel lines that loop around it are suspended and which are kept afloat by buoys. Overdulve Offshore Services designed the Cees Leenaars, a semi-submersible mussel farm that employs the longline method for mussel cultivation. However, the configuration of the longlines and the offshore location of the farm introduce several challenges. The mussel will be exposed to high loads due to wind, current, and waves. Therefore, the question remains if the flow through the mussel farm will be sufficient to provide nutrients to the mussels. Hence, it is of importance to model the behaviour of the mussel droppers in waves.

The model will be constructed by first reviewing the motion of a single 3D pendulum, followed by the motion of a double 3D pendulum. For both situations the Lagrangian method is used to construct the equations of motion. Semi-Implicit Euler is used as integration scheme for the discretization of time. The results provide insights into the chaotic and complex characteristics of pendulums.

Thereafter, a model for a string will be constructed and this model is eventually expanded to a model for a mussel dropper by adding constraints to the last pendulum of the string. The method used for these models was different than for the model for a single and double pendulum due to instability issues. For the string Newton's second law was used to determine the equations of motion, since using this method made it easier to apply external forces and constraints to the system. Instead of a semi-implicit integration scheme an implicit one was used, resulting in an improved stability of the system. Due to the switch from semi to a fully implicit integration scheme, a nonlinear solver was build to solve the set of nonlinear equations at every time step. Later on, it was noticed that the implicit scheme accounted for too much numerical damping. In order to reduce the numerical damping, the Crank-Nicolson method combined with the θ method was applied.

After constructing the model, an experiment was conducted for validating the model and for determining the damping coefficient of the system, which was still unknown. The experiment consisted of a physical model of the dropper and a camera which recorded the motion of the physical model. A code was written to determine the position of the pendulums in each frame and these positions were calculated relative to the angle each pendulum made with the horizontal axis. The experimental setup was reconstructed by the numerical model and compared in order to determine a value for the linear and quadratic damping coefficients. The model overdamped the amplitude of the motion right after the dropper was released from its equilibrium position. This could be due to numerical damping, due to errors in the experiment or due to a faulty translation of the experiment to the model. The linear and quadratic damping were determined to be $b_{linear} = 0.002 \ [kg/s]$ and $b_{quadratic} = 0.001 \ [kg]$. This provides the numerical model with not enough damping to let the motion die out, but it better represents the behaviour of the dropper for larger motions. These coefficients were found to be most suitable because from an engineering perspective it is safer to underestimate the damping in the system and assume higher amplitudes of the motion.

The nonlinear behavior of the mussel dropper is represented by phase space plots that show irregular trajectories and patterns.

Lastly, the 3D model is used to simulate a mussel dropper in waves, as was the aim of this research. The dimensions of the mussel dropper are chosen to represent a real-life mussel dropper. The sea state to which the mussel dropper is subject will be one occurring every once in 25 year in the North Sea. The mussel dropper is simulated using seventeen pendulums. One pendulum is reviewed to determine the response of the mussel dropper. The time signal of this pendulum and the response spectrum of the pendulum show how the pendulum reacts to the incoming waves. A phase space plot is constructed to visualize the chaotic and complex behavior of the mussel dropper in waves.

i

Preface

When I contacted Peter Wellens, telling him that I wanted to combine my knowledge on hydrodynamics with biological aspects for my master thesis, he immediately told me that he knew just the right thesis subject, mussel farms. From that moment on I started working on my master thesis, gathering knowledge on offshore mussel cultivation, while enhancing my scientific skills. The result is this thesis report before you, with as topic: "The Dynamic Response of a Single Mussel Dropper". This thesis is written to obtain the master's degree in Marine Technology with the specialization of Ship Hydrodynamics at the University of Technology Delft.

First of all, I want to thank Peter Wellens for his supervision during my thesis and for offering the opportunity to work on a subject of my liking. You had the ability to respark my enthusiasm when it was sometimes lacking during the process. You were always available for questions and for a brainstorm session. Thank you for your time and support.

I also would like to thank Peter Wellens for introducing me to Deltares, where I had the ability to share my experiences with other graduating students in fields similar to hydrodynamics.

Furthermore, I would like to thank Pascal Chabot for making it possible for me to conduct experiments at the towing tank. I made the request for an experiment quite late, but due to your fast response and immediate help I was able to finish in time. Also, I would like to thank Peter Poot for providing me the tools to conduct my experiment and his help setting it up.

I would also like to thank my family and roommates for their support throughout the whole process. And finally, but certainly not least, I want to give special thanks to my boyfriend for being a listening ear, for asking the right questions and for all the helpful discussions. Thank you for the afternoons studying and looking over my shoulder.

K.E. Huijgen
Rotterdam, March 2024

Contents

List of Figures

List of Tables

Nomenclature

Abbreviations

Abbreviation	Definition
OOS	Overdulve Offshore Services
E-L	Euler-Lagrange
NR	Newton-Raphson

Symbols

Symbol	Definition	Unit
g	Gravitational acceleration	[m/s^2]
m_n	Mass of nth pendulum	[kg]
L_n	Length of nth pendulum	[m]
N	Total number of pendulums	[-]
I	Moment of inertia	[kg m^2]
$\mathbf{r}_n$	Position vector of n$^t h$ pendulum	[m]
θ_N	Polar angle of Nth pendulum	[rad]
ϕ_N	Azimuth angle of Nth pendulum	[rad]
$\dot{\theta}_N$	Polar angular velocity of nth pendulum	[rad/s]
$\dot{\phi}_N$	Azimuth angular velocity of nth pendulum	[rad/s]
$\ddot{\theta}_N$	Polar angular acceleration of nth pendulum	[rad/s^2]
$\ddot{\phi}_N$	Azimuth angular acceleration of nth pendulum	[rad/s^2]
T	Tension of the nth pendulum	[N]
x_n	X-coordinate of the nth pendulum	[m]
y_n	Y-coordinate of the nth pendulum	[m]
z_n	Z-coordinate of the nth pendulum	[m]
$\dot{x}_n$	Velocity in x-direction of the nth pendulum	[m/s]
$\dot{y}_n$	Velocity in y-direction of the nth pendulum	[m/s]
$\dot{z}_n$	Velocity in z-direction of the nth pendulum	[m/s]
$\ddot{x}_n$	Acceleration in x-direction of the nth pendulum	[m/s^2]
$\ddot{y}_n$	Acceleration in y-direction of the nth pendulum	[m/s^2]
$\ddot{z}_n$	Acceleration in z-direction of the nth pendulum	[m/s^2]
v_n	Total velocity of the nth pendulum	[m/s^2]
b_l	Linear damping coefficient	[kg/s]
b_q	Quadratic damping coefficient	[kg]
L	Lagrangian	[J]
T	Kinetic energy	[J]
V	Potential energy	[J]
D	Dissipation function	[kg m$^2/s^2$]
Q	Generalized force	[N m]
q	Generalized coordinate	[rad]
F_x	Force in x-direction	[N]
F_y	Force in y-direction	[N]
F_z	Force in z-direction	[N]
F_b	Damping force	[N]
F_w	Wave force	[N]

Symbol	Definition	Unit
E_x	External force applied in x-direction	[N]
E_y	External force applied in y-direction	[N]
E_z	External force applied in z-direction	[N]
M	Mass matrix	[kg m^2
C	Damping matrix	[kg m^2 rad/s]
G	Potential vector	[kg m^2/s^2]
t	Time	[s]
dt	Time step	[s]
γ	Weight factor for Crank-Nicolson	[-]
J	Jacobian matrix	
Y_k	Vector containing the unknowns	
$F(Y_k)$	Function vector	
D_x	Horizontal distance in x-direction between the dropper	[m]
D_y	Horizontal distance in y-direction between the dropper	[m]
D_z	Vertical distance between the dropper	[m]
M_{tot}	Total mass of the mussel dropper	[kg]
Φ_w	Velocity potential wave	[m^2/s]
η_a	Wave amplitude	[m]
ω	Wave frequency	[rad/s]
μ	Wave direction	[rad]
λ	Wave length	[m]
ϵ_w	Phase of a wave	[rad]
h	Water depth	[m]
k	Wave number	[rad/m]
ρ	Water density	[kg/m^3]
D_{cyl}	Diameter cylinder	[m]
C_D	Drag coefficient	[-]
C_M	Inertia coefficient	[-]
C_A	Added mass coefficient	[-]
u_x	Wave velocity in x-direction	[m/s]
u_y	Wave velocity in y-direction	[m/s]
u_z	Wave velocity in z-direction	[m/s]
$\dot{u}_x$	Wave acceleration in x-direction	[m/s^2]
$\dot{u}_y$	Wave acceleration in y-direction	[m/s^2]
$\dot{u}_z$	Wave acceleration in z-direction	[m/s^2]

1

Introduction

In this chapter the subject of the research will be presented, followed by a small overview of the literature found on the subject. From the literature, a gap in the existing knowledge is determined and it will be explained why it would be advantageous to fill this knowledge gap. The main research and sub-objectives that are constructed will be presented. Next, a description on how to reach the main and sub-objectives is provided, followed by the outline of this thesis report.

1.1. Overdulve Offshore Services

This study examines a longline mussel farm, named "Cees Leenaars", that was designed by Overdulve Offshore Services, further referred to as OOS. The Cees Leenaars is designed to be located offshore and will be placed within the confines of the windpark Borssele 3, located in the North Sea. The Cees Leenaars is designed as a semi-submersible platform so it can endure the harsh environmental conditions present in the North Sea. OOS has joined forces with Deltares to conduct research and experiments on the feasibility of this semi-submersible mussel farm. This collaboration has the potential to make a substantial contribution to the domain of offshore aquaculture.

The semi-submersible mussel farm will make use of longline cultivation to produce mussels. Instead of having the two outer points of a longline anchored to the seabed, as is the conventional method, one end of the line is anchored to the seabed while the other end is attached to the semi-submersible platform. The longlines are submerged to protect them from environmental conditions such as wind and waves. The Cees Leenaars will be designed with a system to efficiently bring in and process the mussel lines in order to improve the production process. The aim of OOS is to make the Cees Leenaars completely self-sufficient. Solar panels, wind turbines, and tidal turbines will provide the platform with the energy to operate. OOS expects this mussel farm to increase the mussel production to the extent that there are more mussels than are demanded. This overshoot in mussels can be used for meat replacement, for example, burgers made of mussels.
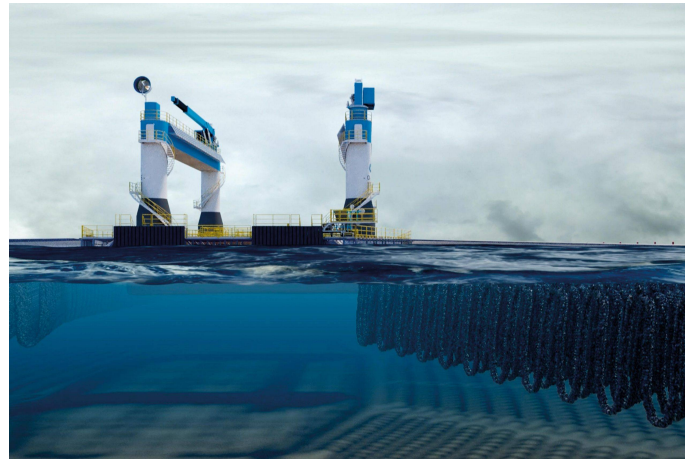
Figure 1.1: The Cees Leenaars, a semi-submersible platform to serve as an offshore mussel farm. The design is made by OOS and must be able to withstand harsh environmental conditions. The Cees Leenaars will apply longline mussel cultivation and is designed to be self-sufficient. Retrieved from International [13]

1.2. Literature

Literature is reviewed to become more familiar with the process of longline mussel cultivation. Even though offshore mussel cultivation is relatively new, some research has already been conducted on the subject. Reviewing the literature, factors are found that are considered to be important when it comes to the feasibility of such a farm. The most important ones being that the mussels within the farm are provided with enough nutrients, and that the structure of a longline can withstand harsh environmental conditions without losing too many mussels.

1.2.1. Offshore Mussel Cultivation

Aquaculture is one of the fastest growing production industries in the world, providing almost half of the world's fish food supply from marine sources [4]. As described by O'Donncha, James, and Ragnoli [21], the growth of aquaculture is commonly referred to as the Blue Revolution. Since capture fisheries have not been able to keep up with the increase in demand of fish consumption, the shortfall has been met by increasing marine farming of finfish, shellfish, and seaweed. Among the different species cultivated, around 8% of the shellfish production consists of mussel cultivation. Mussels are a non-fed species, meaning that they filter their food directly from the surrounding water. In the Dutch part of the North Sea, mainly the blue mussel (Mytilus edulis) is produced [15]. As the global population continues to grow, there is an increasing demand for protein sources. Due to their high nutritional value, mussels have become a popular option for to satisfy this increased demand. However, competition for coastal space limits the expansion of inshore mussel cultivation [4]. In response to this limitation, a shift to offshore mussel farming has been proposed as a solution, offering numerous advantages such as high hydrodynamic areas, increased production capacity, and reduced ecological impact. Furthermore, offshore environments have better water quality with continuous favourable oxygen conditions, lower nutrients and lower primary productivity reducing the risks of exposure to biotoxins and low exposure to diseases, parasites or terrestrial sources of contamination such as pollutants and pesticides [4].

1.2.2. Longline Mussel Cultivation

There exist multiple types of mussel farming, primarily classified as either "off-bottom" or "bottom" cultivation. In the case of bottom cultivation, the mussels are typically dredged from their natural subtidal or intertidal beds and transported to regions more conducive to their growth. However, this practice exposes mussels to potential threats from natural predators such as crabs and starfish. With off-bottom cultivation these predators have less chance of succeeding.

Off-bottom cultivation is also referred to as suspended cultivation. Raft culture, pole culture and longline culture are various techniques of off-bottom mussel cultivation. In the case of raft culture, a rigid structure that is kept afloat by buoys is placed in the water. This structure serves as a platform from which mussel ropes are suspended. Pole culture, also known as Bouchots, is characterized by poles

that are driven into the seabed. From these poles a rope is suspended on which mussels will grow. The last technique refers to a system of lines, known as the backbone, from which evenly spaced ropes that continuously loop around the line are suspended. The backbone is kept afloat by buoys positioned at regular intervals and attached to the seabed by anchors. The suspended ropes that loop from the backbone are known as "mussel droppers" on which the mussels will grow, as was described by [4].

Plew [22] states that a typical longline farm encompasses an expansive area of at least 100 hectares and accommodates over 200 longlines, each with a length ranging between 120 to 150 meters. The average length of the mussel droppers tends to vary between 5 and 30 meters, depending on factors like water depth and nutrient availability [31].
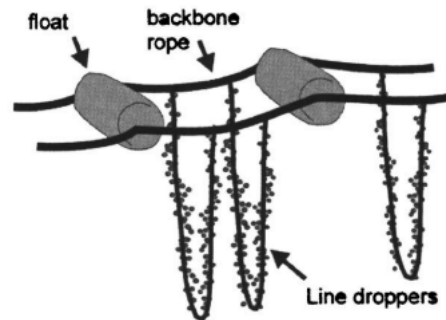
Figure 1.2: A part of a longline, consisting of a backbone rope kept afloat by buoys, from which mussel droppers are suspended. The mussel droppers are suspended as a loop between the backbone. Retrieved from Stevens et al. [30]

1.2.3. Mussel Production
The juvenile stage of mussels is defined as spat. For mussel production this spat must be collected. The spat is procured through a process of collecting naturally occurring spat from the water or the controlled production of spat within shellfish hatcheries. Once the spat reaches a size of approximately 10 millimeters, the spat is suitable to be placed within mussel socks, where the mussels can further grow and develop. Mussels consume phytoplankton, a source of nutrients including nitrogen and phosphorus, in order to grow. An advantage is that the mussels clean the surrounding water by consuming the phytoplankton present in the ocean. The mussels need several months within the sockets to grow and attain the right size for harvest. A complete growth cycle of a mussel is approximately 2 to 3 years. The rate of growth of the mussels depends on environmental conditions, nutrient availability, and the presence of natural predators.

1.2.4. Flow within Mussel Farm
A mussel farm can be defined as a large porous structure that exerts a notable influence on the hydrodynamics of the surrounding environment. The presence of a mussel farm introduces partial obstruction of the water flow which causes distortion of the flow and the current patterns. These occurrences give rise to phenomena such as velocity shears, mixing layers and small-scale turbulence which can significantly impact the supply of essential nutrients and, consequently, the carrying capacity of the mussel farm [4]. Carrying capacity represents the potential maximum production the mussel cultivation can maintain in relation to the food resources available [26]. In this context, carrying capacity depends on the level of nutrients that can reach the mussels located in the farm. This in term depends on the structural configuration of the farm, the orientation of the farm with respect to currents and waves, the density of the longlines and droppers, the distribution of the mussels and other environmental conditions specific to the farm's location [4].

A high density of the mussel droppers within the farm can induce friction between the droppers, leading to reduced current velocities within the farm. Consequently, mussels that are situated at the center of the farm might experience a limited influx of nutrients. Stevens et al. [31] found that the current flow within a farm might be as low as 25% of the external flow surrounding the farm. Due to the decelerated flow, the mussels positioned at the forefront of the current uptake a significant portion of the nutrients before the current reaches the mussels downstream. This ultimately results in diminished mussel growth rates [32].

   The mussel droppers play a significant role in how the water flow dynamics are shaped within the farm. For example, as described by Plew [22], when the longlines are placed under an angle the droppers may interfere with one another. This interference can lead to phenomena like sheltering and wake interference which causes a decay of the current velocity within the farm. Also, the drag caused by the droppers determines the flow within the farm. The drag experienced by a longline is dependent upon factors such as line length, dropper spacing, dropper dimensions and the alignment of the longline relative to the flow direction, as described by Plew [22]. He constructed a velocity model that can estimate the energy dissipation rate of the farm, thereby helping in the determination of the farm's carrying capacity.

1.2.5. Structural Failures

Successful mussel production not solely depends upon the mussel growth rate, but is also influenced by structural vulnerabilities. Examples of these vulnerabilities are anchor failure, rope breakage, line entanglement, buoy implosion, and mussel fall-off [11]. These structural failures are often induced by environmental forces, including wind and waves. Among these forces, the most substantial loading on a longline is due to the pretensioning of the line and the current-induced drag, according to Stevens et al. [30]. In offshore environments, the loads on the farm can be increased due to the influence of waves and strong currents. Waves can cause snap-loads which may lead to line breakage and mussel fall-off. Furthermore, the sustained high loads imposed by waves can lead to fatigue and thereby amplifying the risk of rope breakage, anchor failure and buoy implosion.
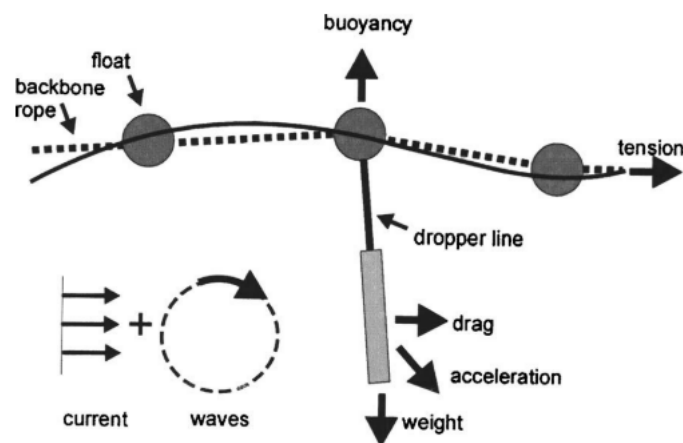
Figure 1.3: An example of the loads and forces on a longline. The backbone experiences buoyancy, tension and a force due to the weight of the mussel dropper. The mussel dropper experiences drag due to current and waves. Retrieved from Stevens et al. [30]

1.3. Knowledge Gap

Reviewing the literature on longline mussel farms, the following observations were made.

- Considerable research has been conducted on the drag of droppers in a steady flow, as well as research on the dynamics of an individual longline ([17], [24], [25], [11]). However, research on the dynamics of an individual dropper is limited.

- Plew [22], Stevens et al. [31], and Landmann et al. [18] have researched the hydrodynamic coefficients of a single dropper and the flow surrounding it. In most of these studies, some simplifications were made. A common simplification was to model droppers as cylinders. In the case where the mussels are attached to suspended lines, this simplification is reasonable since the form of a line is close to that of a cylinder. However, in the case of mussel droppers being loops, the simplification of droppers as cylinders is less appropriate.

- Another simplification found in most studies is that the mussel droppers were modelled as smooth surfaced cylinders having an evenly distributed weight. In reality, the surface of a dropper is very

rough due to the mussels attached to it. The mussels will attach randomly to the dropper and grow at different rates, so no mussel will be exactly the same. This means that the diameter of the dropper is not uniform, but varies over the length. Moreover, this results in an uneven weight distribution and will consequently have an effect on the motion of the dropper. The only instance where droppers were not modelled as cylinders were during physical experiments, such as in the study of Landmann et al. [18]. However, in their physical experiment, the droppers were also suspended lines and not loops. Concluding, there is very little research on droppers as loops.

- Landmann et al. [18] states that the characteristic diameter of the dropper has a significant influence on the hydrodynamic coefficients, and thus an unevenly distributed dropper loop cannot be simulated as a homogeneous flexible cylinder. Therefore, studying the modeling of a dropper that is as physically accurate as possible is crucial to investigate the effect of droppers on flow and dropper dynamics more precisely.

- Stevens et al. [30] describe the dynamics and kinematics of a longline by means of an experiment and recommend a numerical model that will help in determining the response of the longline in waves and current. They describe a longline in waves to be comparable to the steady and oscillating forcing of a sequence of cylinderlike elements suspended from a connected array of floats.

1.4. Main and Sub Objectives
Reviewing the literature and knowledge gaps found, the following research objective is constructed:

The construction of a 3D numerical model of the dynamic response of a mussel dropper in waves.

The goal of this research is to model a mussel dropper as accurately as possible. So, the mussel dropper will be modelled as a deformable loop instead of a rigid cylinder. The model must be able to predict the motion of a mussel dropper when subject to a force. The lumped mass method will be applied to model the mussel dropper as a series of masses connected by massless strings. This is resemblant to a series of connected pendulums. By adjusting the masses at the different nodes, the mass distribution of the dropper can be altered into a nonuniform mass distribution, thus better representing reality. The model must become applicable for different scenarios, meaning that the model should be able to determine the motion of a dropper for different configurations of the dropper.

The following sub-objectives have been constructed in order to reach the main objective.

1. Construct an analytical description of the mussel dropper.
2. Construct a numerical model of the mussel dropper.
3. Conduct an experiment for validation of the model.
4. Compare the results of the numerical model and the experiment to determine the damping coefficient of the dropper.
5. Model the response of the loop when subject to a wave force.

1.5. Motivation
In order to realise the goals and objectives set by OOS, as outlined in section 1.1, it is important that the mussel farm operates at optimal efficiency. This entails ensuring an adequate supply of nutrients to reach the mussels across the entire farm while also considering the impact of wave and current loads to accurately predict failures of the farm. To achieve these objectives, it is of importance to have a comprehensive understanding of the behaviour of the dropper lines within a farm.

While several models and experiments have been constructed to describe longline behaviour, there is not yet a numerical model that accurately estimates the dynamics of a longline. Moreover, existing studies typically model the mussel droppers as cylinders, thereby not capturing their actual behaviour. And the actual behaviour is needed to determine the performance of the mussel farm in an offshore environment. Therefore, a numerical model estimating the behaviour in waves, without the usual simplifications, is needed.

A more accurate model of a single mussel dropper is relevant for scientific reasons as well as for society. When the motion of a single dropper is better understood, it can help to more accurately predict the flow around a dropper and the changes of collision of droppers, line entanglement and mussel fall-off. Better predicting these events can reduce the risk of them occurring, which will result in more efficient mussel farms and a higher production rate. Also, when the motion of one dropper is modelled, the model can more easily be expanded to a longline and eventually to even a whole farm. An accurate model can thus increase the mussel production and help to meet the increased demand for seafood production.

1.6. Methodology

The mussel dropper is a flexible line and in order to analyse the motion of this flexible line, the lumped mass method is applied. Since the lumped mass method divides the dropper into massless segments between two lumped masses, it can be seen as a series of connected pendulums. So, in order to construct the model, a number of pendulums will be connected to each other and eventually the outer end of the last pendulum will be fixed in space, so that the line represents a loop.

In order to construct a numerical model, first an analytical description of the model is made. The dropper is divided into a series of discrete elements, each representing a segment of the dropper. The outer ends of a segment are called nodes. The mass of each segment will be concentrated at the two nodes surrounding it, and so constructing the lumped masses. At each node the force equilibrium is constructed and the equations of motion are determined. The result is a set of differential equations that describe the dynamics of the dropper. Backward Euler time integration is used to discretise the equations and Newton-Raphson will be used to solve the set of nonlinear equations.

The model will be piece-wise constructed. This means that first a 2D model of a pendulum will be made, thereafter a 2D model of a double pendulum and lastly a 2D model for a series of pendulums. Then the model will be adjusted so that the outer node of the connected pendulums is fixed in space. When this is accomplished the same will be done for 3D.

Since the damping coefficient of the dropper is unknown and not something that can be easily calculated, an experiment must be conducted to determine this coefficient. Also, an experiment is needed to validate the constructed model. The results of the experiment will be compared to the results of the model. Then, the damping coefficient of the numerical model will be adjusted so that the motion of the numerical model dampens out in the same time duration as that of the experiment.

Finally, a wave force will be applied to the numerical model. A sea state occuring in the North Sea will be considered. Then, the motion of the mussel dropper when subject to this wave will be analysed.

1.7. Thesis Outline

In chapter 2, some characteristics of a simple pendulum will be discussed and an analytical description of the simple pendulum is provided together with information on the construction of the numerical model for the simple pendulum. In the next chapter 3, the same will be done for a double pendulum. Thereafter, in chapter 4, an analytical description of a string of pendulums and the construction of the numerical model for the string is presented. The model for the string of pendulums is expanded into a model for a mussel dropper in chapter 5. The mussel dropper in waves is discussed in chapter 6. Next, the conducted experiment for validating the 2D model is presented in chapter 7. The results that are generated by the numerical model and the experiment are shown and analysed in chapter 8. The conclusions that are drawn from the results are presented in chapter 9. Finally, recommendations on how to further continue this research are to be found in chapter 10.

2

Pendulum

The mussel dropper will be modelled as a string of connected pendulums. In order to construct this string, first the behaviour and characteristics of a single pendulum must be researched. In this chapter general information on a pendulum will be provided. The forces acting on a single pendulum are presented and it is discussed how damping affects the motion of the pendulum. The equation of motion for a 3D simple pendulum will be derived using the Euler-Lagrange equation. A numerical model is constructed using semi-implicit Euler. At last, the numerical model for the 3D simple pendulum will be verified by reconstructing a conical motion of the pendulum.

2.1. General Information

According to Russel [27], a simple pendulum is defined as a piece of mass that is attached to a frictionless pivot point by a massless string. The mass at the end of the string is commonly called the pendulum bob. When the pendulum is released from a certain height, it will start swinging with an amplitude θ_0 and show a periodic motion. The mass of the pendulum bob exerts a gravitational force on the pendulum, pulling it down. Due to the weight of the pendulum bob there is tension in the string of the pendulum. The net force of the tension and weight of the pendulum is called the restoring force, since this force tries to bring the pendulum back to its vertical position. However, this is an idealised situation, in reality there are also other forces acting on the pendulum. There is also a frictional force present due to the pivot point of the pendulum, where surfaces come together. This friction is neglected in the continuation of this research as simplification. Furthermore, viscous damping can occur due to for example air or water resistance.

In figure 2.1 the forces acting on a simple pendulum in 3D are shown. The tension is directed into the massless string, the gravitational force is pointed downwards, external forces can be applied in all three directions, and the dissipative force is directed against the positive direction of the motion.

(a) Forces acting on the simple pendulum in the xz plane.   (b) Forces acting on the simple pendulum in the xy plane.
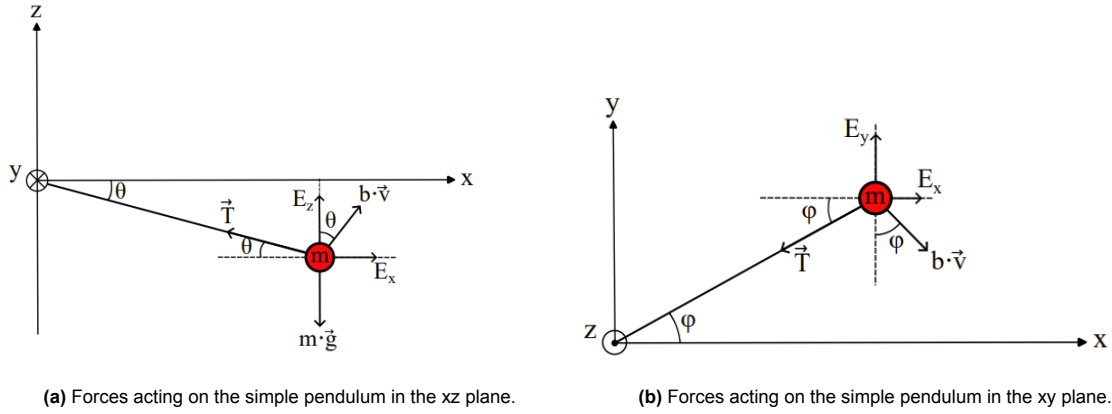
Figure 2.1: A representation of the forces acting on a simple pendulum in two different views. The weight of the mussel droppers causes a downward force, the string connecting the pendulum bob and the pivot point experiences tension, which is directed inline with and inward to the string. The damping of the motion is caused by a dissipative force directed opposite to the motion. An external force can be applied to the pendulum in x, y, and z direction.

The motion of the pendulum can be analysed by plotting the angle of the motion over time. When the motion is linear, the pendulum can be seen as a harmonic oscillator and the angle can be analytically determined using equation (2.1). Here, θ_0 is the amplitude of the motion, which is the displacement of the pendulum bob with respect to the vertical axis, and ω is the angular frequency of the motion. If the amplitude is small, the motion is said to be linear and the small angle approximation can be used. When the amplitude of the motion increases, numerical methods are needed to determine the angle over a period of time.

$$\theta(t) = \theta_0 \, cos(\omega \, t) \tag{2.1}$$

$$\omega = \frac{2\pi}{T} \tag{2.2}$$

The frequency tells something about the number of complete oscillations the pendulum makes in a given unit of time. In equation (2.2), T is the period of the motion, which is defined as the time it takes for the pendulum to complete one full cycle. For small angles, the period can be linearised and is independent of the amplitude. For larger amplitudes, the small angel approximation no longer applies, and the situation becomes nonlinear. When the pendulum does not experience any friction or damping and is released from a certain height, the pendulum will start to oscillate at a constant period and have a constant frequency. Then the period and frequency at which the pendulum then starts to oscillate are called the natural period and frequency. For a simple pendulum, only subject to gravitational force, the natural frequency is equal to equation (2.3). In this equation g represents the gravitational acceleration and L is the length of the pendulum string.

$$\omega_n = \sqrt{\frac{g}{L}} \tag{2.3}$$

2.1.1. Damping
As stated before, the pendulum can be subject to dissipative forces that cause damping, resulting in a decrease in its amplitude over time. These dissipative forces can take the form of viscous or frictional forces, which may include air resistance or resistance due to water. These drag forces are assumed to be linearly proportional to the angular velocity of the pendulum, as described by Dao et al. [8]. The equation for the drag force is shown in (2.4), where b is defined as the damping coefficient and the velocity of the pendulum v is equal to the angular velocity $\dot{\theta}$ times the length of the pendulum string L. The damping coefficient is a parameter that indicates the level of damping present in the pendulum. The coefficient determines the rate at which the amplitude of the oscillation decreases over time.

$$F_D = b \, v = L\dot{\theta} \tag{2.4}$$

The damping coefficient b can be determined using the critical damping coefficient b_{cr} (2.5) and the damping ratio ζ (2.6). The critical damping coefficient is a specific value of the damping coefficient at which the pendulum is critically damped. This coefficient indicates the threshold between underdamping and overdamping. The damping ratio shows the impact of damping on the pendulum's behaviour. When $\zeta > 1$ the pendulum is overdamped. In this state, the pendulum moves slowly toward its equilibrium position without oscillating back and forth. When the damping coefficient is low, thus $\zeta < 1$, the pendulum is underdamped. When underdamped, the pendulum will reach its equilibrium position more quickly. However, it does so while oscillating and overshooting its equilibrium position. The pendulum is critically damped when $\zeta = 1$, i.e. when the damping coefficient is equal to the critical damping coefficient. The critical damping coefficient is defined as the minimum value of the damping coefficient that prevents oscillation. In that case, the pendulum returns to its equilibrium position the quickest and without any oscillation [8]. The critical damping coefficient is a single degree of freedom system, having an equation of motion of the form $m\ddot{x} + b\dot{x} + kx = 0$, is shown in (2.5). In this equation m is the mass of the system and k is the stiffness coefficient. The behaviour of the three damping regimes is shown in figure 2.2.

$$b_{cr} = 2\sqrt{k\,m} \tag{2.5}$$

$$\zeta = \frac{b}{b_{cr}} \tag{2.6}$$
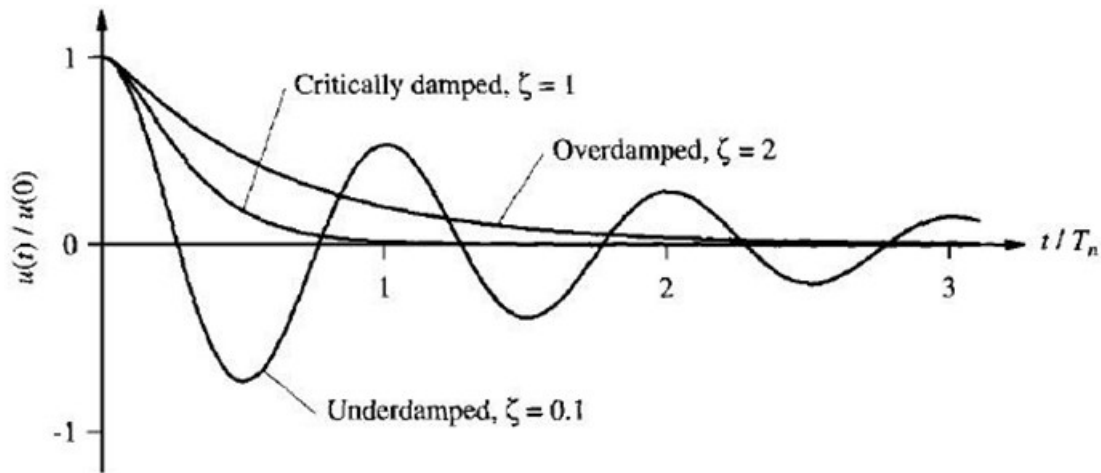
Figure 2.2: The behaviour of an overdamped, an underdamped and a critically damped system over time. Retrieved from Chopra [6]

2.1.2. Equation of Motion

The equation of motion for a single pendulum can be derived using Newton's second rotational law, which states that the sum of the torques around the pivot point is equal to the product of the moment of inertia and the angular acceleration, see equation (2.7). The torque τ is defined as the moment a force causes on the object. Since the tension acting on the string is perpendicular to the angular motion, this force has no contribution to the rotational motion. For the case when there are no external forces exerted on the pendulum, the equation of motion becomes as presented in (2.8). In this equation the moment of inertia is equal to the moment of inertia of a point mass, which is $I = m\,L^2$ and k is the restoring force coefficient, which is equal to $k = m\,g\,L$ and represents the proportionality between the displacement of the system from its equilibrium position and the force that is exerted to bring it back to this equilibrium position.

$$I\ddot{\theta} = \sum \tau \tag{2.7}$$

$$I\ddot{\theta} + b\,L\,\dot{\theta} - k\cos(\theta) = 0 \tag{2.8}$$

Adding external forces in respectively x- and y-direction, F_x and F_y, to the system results in (2.9). The product of the amplitude of the forces and the arm of the forces from the pivot point are directed against the motion of the pendulum, and therefore are negative.

$$I\,\ddot{\theta} + b\,L\,\dot{\theta} - k\,cos(\theta) = -F_x\,L\,sin(\theta) - F_y\,L\,cos(\theta) \tag{2.9}$$

2.2. Analytical Description

The information provided in this chapter has been for a 2D pendulum, but in order to use the pendulum to construct a 3D model of a dropper, a simple pendulum must also be presented in 3D. Generally, spherical coordinates are used to describe the position of the pendulum in three-dimensional space. So, instead of using Cartesian coordinates (x, y, z), the system is described using (r, θ, ϕ). In this system, r represents the radial distance from the origin of the system to the position of the pendulum bob. In this research, the arm length is not variable but fixed at a constant length L. The angle θ represents the polar angle, which is the angle the pendulum makes with respect to the positive vertical axis. The polar angle ranges from zero to π. The angle ϕ represents the azimuth angle, which is the angle the pendulum makes in the xy-plane relative to the x-axis. The azimuth angle ranges from zero to 2π. The configuration of the spherical pendulum is shown in figure 2.3
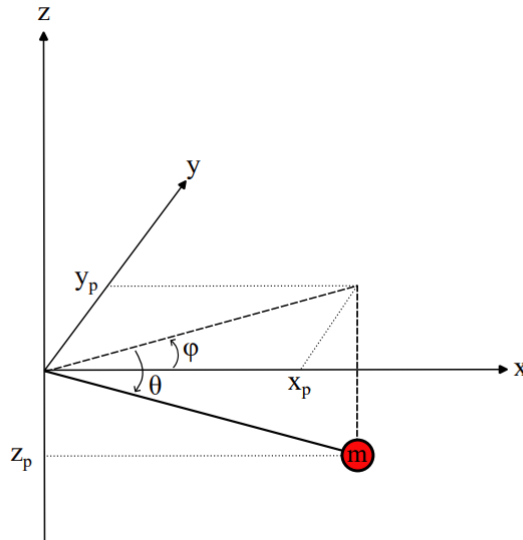
Figure 2.3: The coordinates of the simple pendulum in 3D. The polar angle θ is the angle the pendulum makes with respect to the positive vertical axis and is defined as positive when the angle is clockwise. The azimuth angle ϕ is the angle the pendulum makes in the horizontal plane relative to the positive x-axis. The positive direction of the angle is defined as counterclockwise.

Using spherical coordinates, the x, y and z position of the pendulum can be expressed as shown in (2.10), (2.11) and (2.12).

$$x = L\,cos(\theta)\,cos(\phi) \tag{2.10}$$

$$y = L\,cos(\theta)\,sin(\phi) \tag{2.11}$$

$$z = -L\,sin(\theta) \tag{2.12}$$

2.2.1. Equation of Motion

Since the equation of motion for a 3D pendulum becomes a bit more complex, alternative methods to the Newtonian method were researched. The Lagrangian and Hamiltonian method are both also suitable methods to determine the equation of motion of a 3D pendulum. According to Morin [20] employing the Lagrangian method is more convenient than incorporating Newton's second law when

it comes to problems involving multiple variables. He shows that if the Euler-Lagrange equation is true for one set of coordinates, then the equation is also true for a set of spherical coordinates. Lagrangian mechanics express the equations of motion in terms of generalised coordinates, which can simplify the expression. The Lagrangian method uses the kinetic and potential energy of the system to derive the equation of motion, while Newton mechanics is a vectorial method. In this case, Lagrangian method is used to derive the equation of motion of the 3D pendulum.

$$\frac{d}{dt}(\frac{\partial L}{\partial \dot{q}}) - \frac{\partial L}{\partial q} = 0 \tag{2.13}$$

$$L = T - V \tag{2.14}$$

$$T = \frac{1}{2}\,m\,v^2 \tag{2.15} \qquad\qquad V = m\,g\,z \tag{2.16}$$

The Lagrangian method involves constructing the Euler-Lagrange (E-L) equations (2.13) to represent the equation of motion of the pendulum. These equations rely on the Lagrangian (2.14), which is defined as the kinetic energy T (2.15), where the velocity is equal to $v^2 = \dot{x}^2 + \dot{y}^2 + \dot{z}^2$, minus the potential energy V (2.16) of the system.

Following this method, two equations of motion are constructed for the single 3D pendulum, shown in (2.17) and (2.18).

$$\frac{d}{dt}\left(\frac{\partial L}{\partial \dot{\theta}}\right) - \frac{\partial L}{\partial \theta} = m\,L^2\,\ddot{\theta} - m\,L^2\,cos(\theta)\,sin(\theta)\dot{\phi}^2 + m\,g\,L\,cos(\theta) = 0 \tag{2.17}$$

$$\frac{d}{dt}(\frac{\partial L}{\partial \dot{\phi}}) - \frac{\partial L}{\partial \phi} = m\,L^2\,cos^2(\theta)\,\ddot{\phi} - 2\,m\,L^2\,cos(\theta)\,sin(\theta)\dot{\theta}\,\dot{\phi}^2 = 0 \tag{2.18}$$

Euler-Lagrange including Damping
The Lagrangian method is based on the energy within the system. However, the total equation of motion for the pendulum must also include non-conservative forces such as damping and driving forces. These external forces are added to the Euler-Lagrange equation by using d'Alembert's principle, the total equation of motion becomes than as shown in (2.19). In this equation D represents the Rayleigh dissipation function, which accounts for the dissipative forces in the system. The parameter Q represents other generalised forces in the system. The letter j indicates the generalised coordinate q considered. The generalised coordinates are equal to the degrees of freedom of the system. The E-L equation must be solved for every generalised coordinate. For the 3D pendulum the set of generalised coordinates is equal to $q = (\theta, \phi)$.

$$\frac{d}{dt}(\frac{\partial L}{\partial \dot{q}_j}) - \frac{\partial L}{\partial q_j} + \frac{\partial D}{\partial \dot{q}_j} = Q_j \tag{2.19}$$

To account for linear damping in the system, the Rayleigh dissipation function (2.20) is employed. This function can be used to determine the generalised drag force and can then be applied in the Euler-Lagrange equation. The number of particles considered is indicated by n, which in this thesis will indicate the number of pendulums in the system.

$$D = \frac{1}{2}\sum_{n=1}^{N} b_n v_n^2 \tag{2.20}$$

In this equation b is the damping coefficient and v_n is the generalised velocity of the nth pendulum. The dissipative force the system experiences is equal to the velocity gradient of the Rayleigh dissipation function (2.21). Substituting the dissipative force into the equation for generalised forces results in expression 2.22.

$$\mathbf{F}^f = -\nabla_v D \tag{2.21}$$

$$Q_j^f = \sum_{n=1}^{N} \mathbf{F}_n^f \frac{\partial \mathbf{r}_n}{\partial q_j} = \sum_{n=1}^{N} \mathbf{F}_n^f \frac{\partial \dot{\mathbf{r}}_n}{\partial \dot{q}_j} = -\sum_{n=1}^{N} \nabla_{v_n} D \frac{\partial \dot{\mathbf{r}}_n}{\partial \dot{q}_j} = -\frac{\partial D}{\partial \dot{q}_j} \tag{2.22}$$

Since the velocity of the pendulum in direction of the polar angle is equal to $v_\theta = L\,\dot{\theta}$ and the velocity in direction of the azimuth angle is equal to $v_\phi = L\,cos(\theta)\,\dot{\phi}$, the damping contributions to the equations of motion become:

$$\frac{\partial D}{\partial \dot{\theta}} = b\,L^2\,\dot{\theta} \tag{2.23}$$

$$\frac{\partial D}{\partial \dot{\phi}} = b\,L^2\,cos^2(\theta)\,\dot{\phi} \tag{2.24}$$

Euler-Lagrange including External Forces
In the original Euler-Lagrange equation, external forces are not taken into account, instead generalised forces are presented to include these forces in the equation of motion. The equation for a generalised force is presented in equation 2.25. Where **F** is a vector containing the amplitude of the forces in 3D, r is the position vector of the pendulum in 3D and q_j is the generalised coordinate. The generalised forces for the 3D pendulum are shown in (2.26) and (2.27).

$$Q_j = \sum_{n=1}^{N} \mathbf{F}_n \frac{\partial \mathbf{r}_n}{\partial q_j} \tag{2.25}$$

$$Q_\theta = \begin{bmatrix} F_x \\ F_y \\ F_z \end{bmatrix} \begin{bmatrix} -L\,sin(\theta)\,cos(\phi) \\ -L\,sin(\theta)\,sin(\phi) \\ -L\,cos(\theta) \end{bmatrix} \tag{2.26}$$

$$Q_\phi = \begin{bmatrix} F_x \\ F_y \\ F_z \end{bmatrix} \begin{bmatrix} -L\,cos(\theta)\,sin(\phi) \\ L\,cos(\theta)\,cos(\phi) \\ 0 \end{bmatrix} \tag{2.27}$$

Complete Euler-Lagrange Equations
Filling in equations (2.17), (2.23) and (2.26) for the equation of theta and (2.18), (2.24) and (2.27) in (2.19) provides the complete equations of motion as presented in (2.28) and (2.29).

$$\frac{d}{dt}\left(\frac{\partial L}{\partial \dot{\theta}}\right) - \frac{\partial L}{\partial \theta} + \frac{\partial D}{\partial \dot{\theta}} = m\,L^2\,\ddot{\theta} - m\,L^2\,cos(\theta)\,sin(\theta)\dot{\phi}^2 + m\,g\,L\,cos(\theta) + b\,L^2\,\dot{\theta}$$
$$= -F_x\,L\,sin(\theta)\,cos(\phi) - F_y\,L\,sin(\theta)\,sin(\phi) - F_z\,L\,cos(\theta) \tag{2.28}$$

$$\frac{d}{dt}\left(\frac{\partial L}{\partial \dot{\phi}}\right) - \frac{\partial L}{\partial \phi} + \frac{\partial D}{\partial \dot{\phi}} = m\,L^2\,cos^2(\theta)\,\ddot{\phi} - 2\,m\,L^2\,cos(\theta)\,sin(\theta)\dot{\theta}\,\dot{\phi}^2 + b\,L^2\,cos^2(\theta)\,\dot{\phi}$$
$$= -F_x\,L\,cos(\theta)\,sin(\phi) + F_y\,L\,cos(\theta)\,cos(\phi) \tag{2.29}$$

These equations can be rewritten into expressions for the second derivatives of the angles, (2.30) and (2.31).

$$\ddot{\theta} = \frac{1}{m\,L^2}\left(m\,L^2\,cos(\theta)\,sin(\theta)\dot{\phi}^2 - m\,g\,L\,cos(\theta) - b\,L^2\,\dot{\theta} - F_x\,L\,sin(\theta)\,cos(\phi) - F_y\,L\,sin(\theta)\,sin(\phi) - F_z\,L\,cos(\theta)\right)$$
$$\tag{2.30}$$

$$\ddot{\phi} = \frac{1}{m\,L^2\,cos^2(\theta)}\left(2\,m\,L^2\,cos(\theta)\,sin(\theta)\dot{\theta}\,\dot{\phi}^2 - b\,L^2\,cos^2(\theta)\,\dot{\phi} - F_x\,L\,cos(\theta)\,sin(\phi) + F_y\,L\,cos(\theta)\,cos(\phi)\right)$$
$$\tag{2.31}$$

2.3. Numerical Method

After the equations of motion for the 3D pendulum are derived, a numerical method is used to determine the behaviour over time. In this research Euler's method is used as the numerical method to solve the equations of motion.

2.3.1. Euler's method

Euler's method is a numerical method used to estimate the solution to a first-order differential equation of the form $\frac{dy}{dt} = f(x,t)$. This method approximates a tangent line at multiple time steps to estimate the graph of the solution of $y(t)$.
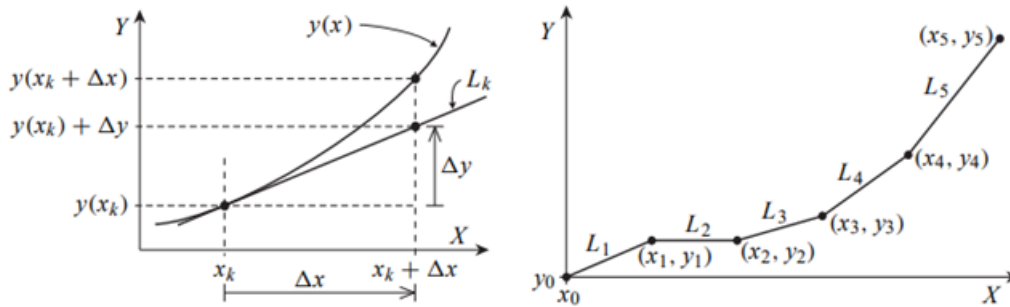
Figure 2.4: A visual representation of how explicit Euler approximates the solution of a first-order differential equation of the form $\frac{dy}{dt} = f(x,t)$. Retrieved from *Euler's numerical method* [10]

In figure 2.4, it is shown how Euler's method operates. The real solution is given by $y(x)$. Now, consider a point on the graph, namely $(x_k, y(x_k))$. A tangential straight line is used to estimate the next point on the graph $(x_k + \delta x, y(x_k + \delta x))$. The next value $y(x_k + \delta x)$ is approximately equal to $y(x_k) + \delta y$. The slope of the tangent line is equal to $\frac{dy}{dx} = f(x_k, y(x_k))$. Using this, δy is determined to be equal to $\delta y = \delta x f(x_k, y(x_k))$. Furthermore, $y(x_k)$ is usually expressed as an approximation, namely y_k. The estimated next step on the graph of the solution is then calculated using equation 2.32.

$$y(x_k)\delta x \approx y(x_k) + \delta x \, f(x_k, y_k) \tag{2.32}$$

The Euler's method as described, is commonly referred to as explicit, or forward Euler. In addition, there are multiple variations to this method. One variation is implicit, also referred to as backward Euler. The core principle of the explicit method involves using the current solution to approximate the solution at the next time step. Using an implicit method, the solution at the next time step is determined using information of the next time step, resulting in a nonlinear equation. Semi-implicit Euler combines both methods, applying explicit Euler to one differential equation and implicit to the other. All three methods will be applied in the case of the double pendulum.

The explicit method is a conditionally stable one. This entails that the size of the time step is critical to obtain stability. The time step must be sufficiently small, otherwise, the solution can become unstable and grow over time. Implicit Euler, however, is unconditionally stable, meaning that stability is not influenced by the time step. Even though this method is unconditionally stable, the time step does still affect the accuracy of the solution. Implicit Euler tends to dampen initial errors, which can result in a decrease of the amplitude of the solution over time. Because semi-implicit Euler combines both methods, it balances the potential growth in the solution that can occur due to the explicit method by offsetting it with the decrease in the solution associated with the implicit method.

At each time step, a small error occurs because the estimated value is most likely not equal to the exact solution. This error is quantified as the difference between the computed value y_k and the true value $y(x_k)$ and known as the local truncation error. The local truncation error for all three methods is equal to $O(h^2)$, defining these methods as first-order methods.

The integration scheme of the explicit Euler method is shown in (2.33). The solution at the next time step $(i + 1)$ is determined by information on the current time step. For implicit Euler, the solution at the next time step is determined by information on the next time step, as can be seen in its integration scheme in (2.34).

$$y_{i+1} = y_i + dt\, f(t_i, y_i) \tag{2.33}$$

$$y_{i+1} = y_i + dt\, f(t_{i+1}, y_{i+1}) \tag{2.34}$$

All three methods were reviewed to determine the motion of the double pendulum. Each method has its own advantages and disadvantages. The accuracy of the numerical model, the stability, and the computational time are some factors that determine which method is most efficient. For the single 3D pendulum, semi-implicit Euler was determined to be the most efficient method.

2.3.2. Semi-Implicit Euler

Semi-Implicit Euler can be applied to a set of differential equations. This method is a combination of explicit and implicit Euler, where implicit Euler is applied to the first differential equation and explicit Euler is applied to the second differential equation (2.35). In these equations, dt is defined as the time step and i indicates the time iteration.

$$\begin{aligned} y'_{i+1} &= y'_i + dt\, f(t_i, y_i) \\ y_{i+1} &= y_i + dt\, y'_{i+1} \end{aligned} \tag{2.35}$$

The integration scheme can then be determined using equations (2.30), (2.31) and (2.35). These equations are used to determine the motion over time. The model requires an initial guess and the time step as input.

$$\begin{aligned} \theta_{i+1} &= \theta_i + dt\, \dot{\theta}_i \\ \dot{\theta}_{i+1} &= \dot{\theta}_i + dt\, (\frac{1}{m\,L^2}\, (m\,L^2\, cos(\theta_i)\, sin(\theta_i)\dot{\phi_i}^2 - m\,g\,L\,cos(\theta_i) - b\,L^2\,\dot{\theta}_i) - \\ & F_x\,L\,sin(\theta_i)\,cos(\phi_i) - F_y\,L\,sin(\theta_i)\,sin(\phi_i) - F_z\,L\,cos(\theta_i)) \end{aligned} \tag{2.36}$$

$$\begin{aligned} \phi_{i+1} &= \phi_i + dt\, \dot{\phi}_i \\ \dot{\phi}_{i+1} &= \dot{\phi}_i + dt\, (\frac{1}{m\,L^2\,cos^2(\theta_i)}\, (2\,m\,L^2\,cos(\theta_i)\,sin(\theta_i)\dot{\theta}_i\,\dot{\phi_i}^2 - b\,L^2\,cos^2(\theta_i)\,\dot{\phi}_i) \\ & - F_x\,L\,cos(\theta_i)\,sin(\phi_i) + F_y\,L\,cos(\theta_i)\,cos(\phi_i)) \end{aligned} \tag{2.37}$$

2.3.3. Verification: The Conical Pendulum

A conical pendulum is a variation on the simple pendulum. The pendulum has a fixed chord length and moves at a constant speed. The name of the conical pendulum is originated from the motion the pendulum exhibits. The pendulum bob traces a circular or elliptical path, creating the appearance of a cone.

The angular frequency the pendulum needs in order to make the conical motion can be derived from the fact that in order for the pendulum to draw a constant elliptical trajectory, the contribution of the gravitational force in the tangential direction to the motion in xy plane must be equal to the centrifugal force. The angular frequency in ϕ direction must be equal to $\dot{\phi} = \sqrt{\frac{g}{Lcos\theta}}$, as described by Cross [7]. In order to verify the model of the simple 3D pendulum, the angular frequency needed to obtain a conical motion is used as input for the model. The initial conditions are provided in table 2.1 and as can be seen in figure 2.5 the pendulum indeed shows a conical motion. The pendulum's path does not trace a perfect circle, this is due to non-linearity in the motion.

When damping is added to the system, the amplitude of both angles should decrease over time. Applying a damping coefficient of 0.2 to the system shows indeed a decay of the motion over time, see figure 2.6.

Initial conditions single 3D model		
L	1	$[m]$
m	1	$[kg]$
θ_0	$\frac{\pi}{8}$	$[rad]$
ϕ_0	0	$[rad]$
$\dot{\theta}_0$	0	$[rad/s]$
$\dot{\phi}_0$	3.0105	$[rad/s]$
dt	0.05	$[s]$
t_{end}	40	$[s]$
b_l	0 & 0.2	$[-]$
F_x	0	$[N]$
F_y	0	$[N]$
F_z	0	$[N]$

Table 2.1: The initial conditions for the simulation of a single 3D pendulum which is supposed to make a conical motion. One simulation is done without and one simulation is done with damping.
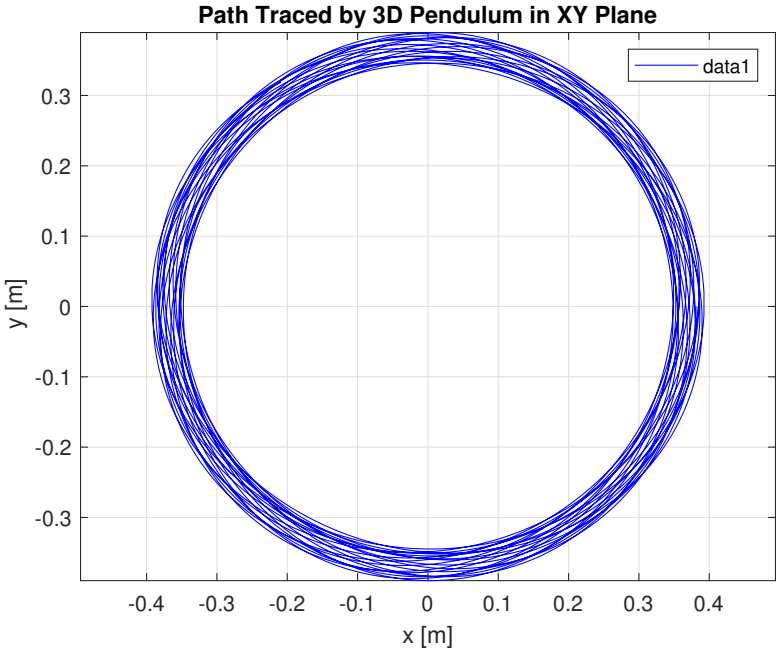
Figure 2.5: A plot of the trajectory drawn by the 3D pendulum experiencing a conical motion without damping. The x-axis shows the x-position of the pendulum at a moment in time. The y-axis shows the y-position of the pendulum at a moment in time.
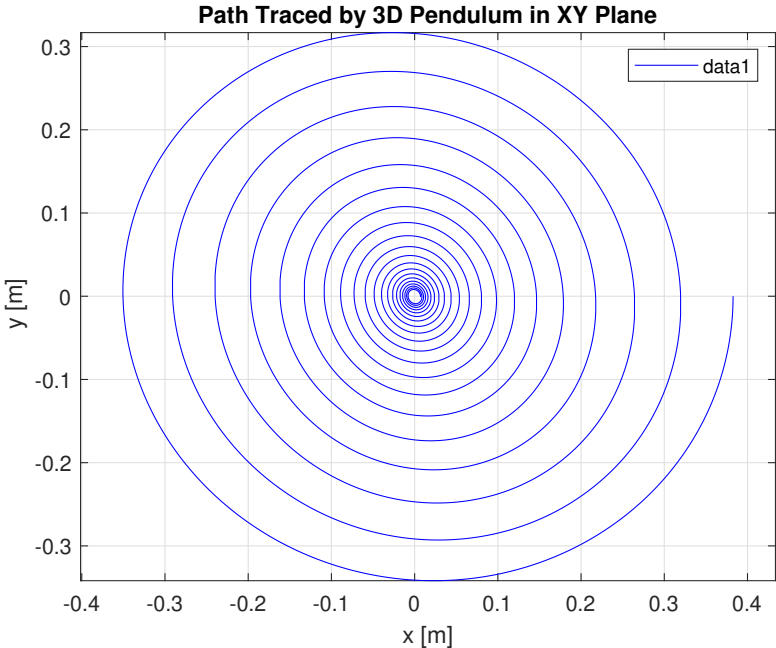
Figure 2.6: A plot of the trajectory drawn by the 3D pendulum experiencing a conical motion with damping. The x-axis shows the x-position of the pendulum at a moment in time. The y-axis shows the y-position of the pendulum at a moment in time. Due to damping the path drawn by the pendulum reduces, moving the pendulum back to it's rest position.

3

Double Pendulum

In this chapter the equations of motion for a double pendulum are derived using the Euler-Lagrange equation. A numerical model is constructed using semi-implicit Euler. At last, two simulations are described, one where the double pendulum experiences a periodic motion and one where it experiences a chaotic motion.

3.1. General Information

When two pendulums are connected, a double pendulum is created. The double pendulum is a popular way to gain insight into chaos. Chaotic motion means that the system behaves unpredictably. Jørgensen and Fath [14] describe chaos as the irregular and unpredictable time evolution of many non-linear and complex linear systems. A double pendulum exhibits two normal modes: one in which the pendulums are in phase and another where they are out of phase.

That a double pendulum can show either a periodic or a chaotic motion is researched by Sarkar, Kumar, and Khastgir [28]. The periodic motion can be either oscillatory or rotational. Furthermore, Sarkar, Kumar, and Khastgir [28] concluded that when the masses of the double pendulum are unequal, the motion becomes multi-periodic for small amplitudes and chaotic for large amplitudes.

The equations of motion for a double pendulum are coupled nonlinear differential equations. As opposed to the simple pendulum, these equations cannot be linearised as the small angle approximation is not valid for this system. Due to the chaotic nature of the double pendulum, a small change in the initial conditions can lead to a completely different motion.
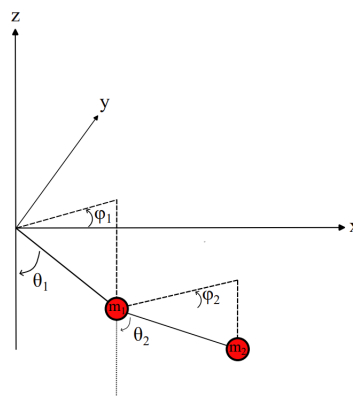
Figure 3.1: The double pendulum depicted in a space-fixed coordinate system. The first pendulum is fixed to the origin of the coordinate system. The second pendulum is attached to the first pendulum and the polar and azimuth angle of the second pendulum are defined as the angle the second pendulum makes with respect to the first pendulum. The coordinates of the second pendulum are equal to the sum of the distance the first and second pendulum make in x, y, and z direction.

3.2. Analytical Description

To achieve the equations of motion for a double pendulum, the Lagrangian method as described in chapter 2 is applied. The definition of θ_n is now chosen as the angle between the vertical axis and the pendulum instead of the horizontal axis. The position of the pendulum bobs are described by (3.1) and (3.2).

$$\mathbf{r}_1 = \begin{bmatrix} L_1\,sin(\theta_1)\,cos(\phi_1) \\ L_1\,sin(\theta_1)\,sin(\phi_1) \\ -L_1\,cos(\theta_1) \end{bmatrix} \tag{3.1}$$

$$\mathbf{r}_2 = \mathbf{r}_1 + \begin{bmatrix} L_2\,sin(\theta_2)\,cos(\phi_2) \\ L_2\,sin(\theta_2)\,sin(\phi_2) \\ -L_2\,cos(\theta_2) \end{bmatrix} \tag{3.2}$$

The system has now a set of four generalised coordinates, namely $\mathbf{q} = (\theta_1, \phi_1, \theta_2.\phi_2)$. So, there will be four equations of motion in total, one Euler-Lagrange equation for every generalised coordinate.

The Lagrangian is now dependent on the kinetic and potential energy of the first and the second pendulum (4.1). The total kinetic energy for the double pendulum is equal to equation (3.4). The total potential energy for the double pendulum is equal to equation (3.5).

$$L = \sum T - \sum V \tag{3.3}$$

$$\sum T = T_1 + T_2 = \frac{1}{2}m_1\,(\dot{x}_1^2 + \dot{y}_1^2 + \dot{z}_1^2) + \frac{1}{2}m_2\,(\dot{x}_2^2 + \dot{y}_2^2 + \dot{z}_2^2) \tag{3.4}$$

$$\sum V = V_1 + V_2 = m_1\,g\,z_1 + m_2\,g\,z_2 \tag{3.5}$$

This results in Lagrangian as provided in equation (3.6).

$$
\begin{aligned}
L = &\frac{1}{2}\,(m_1 + m_2)\,L_1^2\,\dot{\theta}_1^2 + \frac{1}{2}\,(m_1 + m_2)\,L_1^2\,\dot{\phi}_1^2\,sin^2(\theta_1) + \frac{1}{2}\,m_2\,L_2^2\,\dot{\theta}_2^2 + \frac{1}{2}\,m_2\,L_2^2\,\dot{\phi}_2^2\,sin^2(\theta_2) \\
&+ m_2 L_1 L_2 \dot{\theta}_1 \dot{\theta}_2 (cos(\theta_1)cos(\theta_2)cos(\phi_1 - \phi_2) + sin(\theta_1)sin(\theta_2)) + m_2 L_1 L_2 \dot{\theta}_1 \dot{\phi}_2 cos(\theta_1)sin(\theta_2)sin(\phi_1 - \phi_2) \\
&+ m_2 L_1 L_2 \dot{\phi}_1 \dot{\theta}_2 sin(\theta_1)cos(\theta_2)sin(\phi_2 - \phi_1) + m_2 L_1 L_2 \dot{\phi}_1 \dot{\phi}_2 sin(\theta_1)sin(\theta_2)cos(\phi_1 - \phi_2) \\
&+ (m_1 + m_2)\,g\,L_1\,cos(\theta_1) + m_2\,g\,L_2\,cos(\theta_2)
\end{aligned}
\tag{3.6}
$$

Generalised Forces

Each pendulum bob can be excited by an external force. Therefore a force $E_1 = [E_{x_1}, E_{y_1}, E_{z_1}]^T$ is introduced, which is applied to the first pendulum bob, and a force $E_2 = [E_{x_2}, E_{y_2}, E_{z_2}]^T$ is introduced, which is applied to the second pendulum bob, see figure 4.2. The equation for the generalised forces as presented in (2.25) becomes the sum of the two forces times the partial derivative of their position vector over the generalised coordinate (3.7).

$$Q_j = \mathbf{F}_1\frac{\partial \mathbf{r}_1}{\partial q_j} + \mathbf{F}_2\frac{\partial \mathbf{r}_2}{\partial q_j} \tag{3.7}$$

Damping

Using the equation as provided in (2.20), the dissipation function of the double pendulum becomes equal to equation (3.8). Where the velocity squared of the first pendulum is equal to $v_1^2 = \dot{x}_1^2 + \dot{y}_1^2 + \dot{z}_1^2$ and the velocity squared of the second pendulum is equal to $v_2^2 = \dot{x}_2^2 + \dot{y}_2^2 + \dot{z}_2^2$

$$D = \frac{1}{2}b\,v_1^2 + \frac{1}{2}b\,v_2^2 \tag{3.8}$$

(a) Forces acting on the double pendulum in xz plane.

(b) Forces acting on the double pendulum in xy plane.
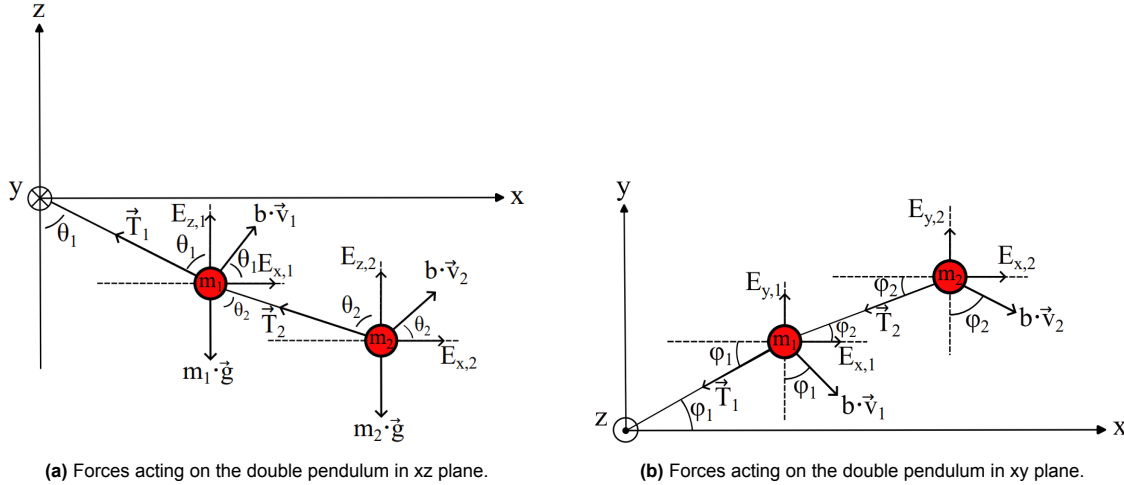
Figure 3.2: A representation of the forces acting on a double pendulum in two different views. Each pendulum experiences a gravitational force, a dissipative force due to its motion and external forces can be applied to both pendulums. The first pendulum bob is now attached to two strings, therefore it experiences a tension from the first string and the second string.

3.2.1. Equation of Motion

Using the equations for the Lagrangian (3.6), the generalised forces (3.7) and the dissipation function (3.8), the total equations of motion for the double pendulum can be constructed by substituting these equations and the generalised coordinates q into the Euler-Lagrange equation. This results in four equations of motion, one for every generalised coordinate, which will have the form of respectively (3.9), (3.11), (3.10) and (3.12).

$$\frac{d}{dt}\left(\frac{\partial L}{\partial \dot{\theta}_1}\right) - \frac{\partial L}{\partial \theta_1} + \frac{\partial D}{\partial \dot{\theta}_1} = Q_{\theta_1} \quad (3.9) \qquad \frac{d}{dt}\left(\frac{\partial L}{\partial \dot{\theta}_2}\right) - \frac{\partial L}{\partial \theta_2} + \frac{\partial D}{\partial \dot{\theta}_2} = Q_{\theta_2} \quad (3.10)$$

$$\frac{d}{dt}\left(\frac{\partial L}{\partial \dot{\phi}_1}\right) - \frac{\partial L}{\partial \phi_1} + \frac{\partial D}{\partial \dot{\phi}_1} = Q_{\phi_1} \quad (3.11) \qquad \frac{d}{dt}\left(\frac{\partial L}{\partial \dot{\phi}_2}\right) - \frac{\partial L}{\partial \phi_2} + \frac{\partial D}{\partial \dot{\phi}_2} = Q_{\phi_2} \quad (3.12)$$

The complete equations of motion can be found in appendix A. The resulting set of equations are coupled. Meaning that the equations of motion for the generalised coordinates of the first pendulum are dependent on the generalised coordinates of the second pendulum, and vice versa. Due to this coupling, the behaviour of a double pendulum becomes quite complex. To give better insight in how the equations are coupled, the set of equations is written into matrix form (3.13), the complete equation can be found in appendix A. In this equation q_1 represents the generalised coordinates of the first pendulum and q_1 of the second pendulum. Matrices M and C, as well as the vectors G and Q are all functions of the generalised coordinates q. The matrix components $M_{12}, M_{21}, C_{12}, C_{21}$ represent the couple terms of the two pendulums.

$$\left[\begin{array}{c|c} \mathbf{M}_{11} & \mathbf{M}_{12} \\ \hline \mathbf{M}_{21} & \mathbf{M}_{22} \end{array}\right] \begin{bmatrix} \ddot{\mathbf{q}}_1 \\ \ddot{\mathbf{q}}_2 \end{bmatrix} + \left[\begin{array}{c|c} \mathbf{C}_{11} & \mathbf{C}_{12} \\ \hline \mathbf{C}_{21} & \mathbf{C}_{22} \end{array}\right] \begin{bmatrix} \dot{\mathbf{q}}_1 \\ \dot{\mathbf{q}}_2 \end{bmatrix} + \begin{bmatrix} \mathbf{G}_1 \\ \mathbf{G}_2 \end{bmatrix} = \begin{bmatrix} \mathbf{Q}_1 \\ \mathbf{Q}_2 \end{bmatrix} \quad (3.13)$$

3.3. Numerical Method

Just as for the the numerical model of the simple pendulum, the semi-implicit Euler method as described in chapter 2 is used to construct a numerical model for the double pendulum. To construct the integration scheme, the vector q containing the generalised coordinates is used.

$$\mathbf{q}_{i+1} = \mathbf{q}_i - dt\, \dot{\mathbf{q}}_{i+1} \quad (3.14)$$

$$\dot{\mathbf{q}}_{i+1} = \dot{\mathbf{q}}_i - dt\, \ddot{\mathbf{q}}_i \quad (3.15)$$

The second derivative of the generalised coordinates can be obtained by rewriting the matrix equation as provided in (3.13).

$$\ddot{\boldsymbol{q}}_i = \boldsymbol{M}_i^{-1}\left(\boldsymbol{Q}_i - \boldsymbol{G}_i - \boldsymbol{C}_i\,\dot{\boldsymbol{q}}_i\right) \tag{3.16}$$

Division by zero
Considering the equations of motion for ϕ_1 and ϕ_2 as shown in appendix A, it can be noticed that in the numerical scheme, these equations include a $\frac{1}{sin(\theta)}$ term. That means that when θ gets close to zero, this term will become infinite. This leads to not-a-number values in the numerical model and therefore division by zero must be avoided. The limit of this term when θ reaches zero must be found and incorporated into the model. L'Hopital's rule (3.17) is applied to find the limit.

$$\lim_{x\to 0}\frac{f(x)}{g(x)} = \lim_{x\to 0}\frac{f'(x)}{g'(x)} \tag{3.17}$$

From this rule follows that the limit of $\frac{1}{sin(\theta)}$ is equal to the limit of $\frac{0}{cos(\theta)}$, which is equal to zero. That means that when θ gets close to zero, the term becomes zero. In order to apply this in the numerical model, an if-statement is added saying that if $sin(\theta) < e^{-6}$ then all division by $sin(\theta)$ terms in the equations become zero. The risk is that the accuracy of the model is decreased due to this statement. However, this is unavoidable since a division by zero is not possible in numerical models.

3.3.1. Periodic Motion vs. Chaos
A small verification of the model for the double pendulum is executed by the fact that a completely deterministic system can have chaotic dynamics as well as linear dynamics [2]. If the double pendulum exhibits motions as expected, then the model can be expanded to a series of connected pendulums. The model for the double pendulum was tested for two situations, namely one where the double pendulum exhibits a periodic motion, for which the initial conditions can be found in table 3.1, and one where the double pendulum shows chaotic behaviour, for which the initial conditions are presented in table 3.2. In both situation there was no damping present and no external forces at work. The time step had to be very small, see table 3.1 and 3.2, otherwise the model would become unstable.

In figure 3.3 a 3D scatter plot is constructed of the double pendulum with the initial conditions as described in the table below. Both pendulums follow a regular pattern and moved in-phase with each other. The initial angle and velocity of the system was given was not large enough to result in more complex behaviour.

Initial conditions double 3D model		
L_1	1	$[m]$
L_2	1	$[m]$
m_1	1	$[kg]$
m_2	1	$[kg]$
θ_{1_0}	$\frac{\pi}{4}$	$[rad]$
ϕ_{1_0}	0	$[rad]$
$\dot{\theta}_{1_0}$	0	$[rad/s]$
$\dot{\phi}_{1_0}$	0.3	$[rad/s]$
θ_{2_0}	$\frac{\pi}{4}$	$[rad]$
ϕ_{2_0}	0	$[rad]$
$\dot{\theta}_{2_0}$	0	$[rad/s]$
$\dot{\phi}_{2_0}$	0.3	$[rad/s]$
dt	$3.33\,10^{-5}$	$[s]$
t_{end}	50	$[s]$
b_l	0	$[-]$
F_1	0	$[N]$
F_2	0	$[N]$

Table 3.1: The initial conditions of a simulation of a double pendulum experiencing a periodic motion. The double pendulum is released from an certain height and is given a small velocity in the direction of the azimuth angle.
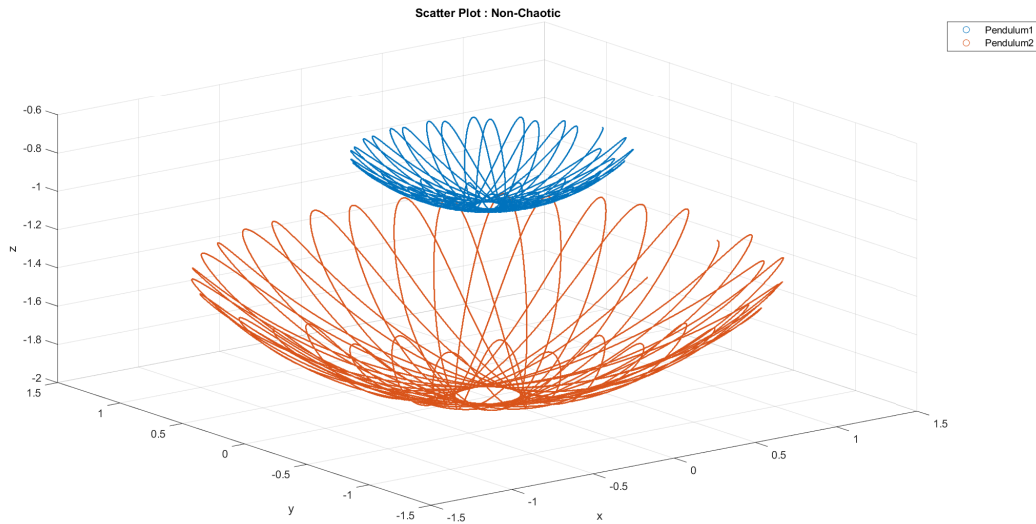
Figure 3.3: A 3D scatter plot of the simulation of a double pendulum experiencing a periodic motion. The plot shows the regular trajectory of both pendulums.

For the second set of initial conditions, the double pendulum did experience chaotic behaviour. Comparing figure 3.4 to figure 3.3, it can be seen that the pendulum now no longer shows a periodic motion, but the trajectories are now completely unpredictable. The initial angle θ and initial velocity in ϕ direction of the system were enlarged and the initial angular velocity in θ direction was now also given a value. This display of chaos is presented in a more orderly manner in figure 3.5 and 3.6.

Initial conditions double 3D model		
L_1	1	$[m]$
L_2	1	$[m]$
m_1	1	$[kg]$
m_2	0.2	$[kg]$
θ_{1_0}	$\frac{\pi}{2}$	$[rad]$
ϕ_{1_0}	0	$[rad]$
$\dot{\theta}_{1_0}$	$-\frac{\pi}{2}$	$[rad/s]$
$\dot{\phi}_{1_0}$	$\frac{\pi}{6}$	$[rad/s]$
θ_{2_0}	$\frac{\pi}{2}$	$[rad]$
ϕ_{2_0}	0	$[rad]$
$\dot{\theta}_{2_0}$	$-\frac{\pi}{2}$	$[rad/s]$
$\dot{\phi}_{2_0}$	$\frac{\pi}{6}$	$[rad/s]$
dt	$3.33\,10^{-5}$	$[s]$
t_{end}	50	$[s]$
b_l	0	$[-]$
F_1	0	$[N]$
F_2	0	$[N]$

Table 3.2: The initial conditions of a simulation of a double pendulum experiencing chaos. The double pendulum is released from a certain height and is given a velocity in the direction of the azimuth angle and the polar angle. The masses are given different values.
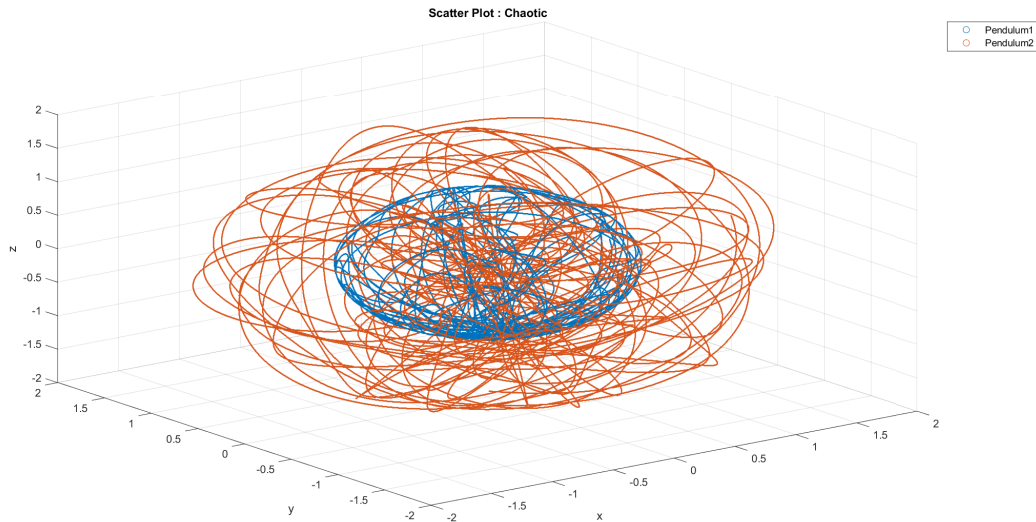
Figure 3.4: A 3D scatter plot of the simulation of a double pendulum experiencing chaos. The plot shows the irregular trajectory and complex behaviour of both pendulums.

Phase Space

In these figures the phase space for θ of the first pendulum and second pendulum are shown. The first situation, the periodic one, is compared to the second situation, the chaotic one. A phase space plot is constructed by plotting the angular velocity over the angular displacement. In the figures for the periodic motion, a regular pattern is observed. Since there is no damping or external forces present in the system, there is no energy leaving or added to the system. That is confirmed by the fact that the phase space plots consist of closed curves.

The phase space diagrams of the chaotic motion are much more irregular than the periodic ones. Still, energy is also for this motion conserved, as the plot consists again of only closed curves.
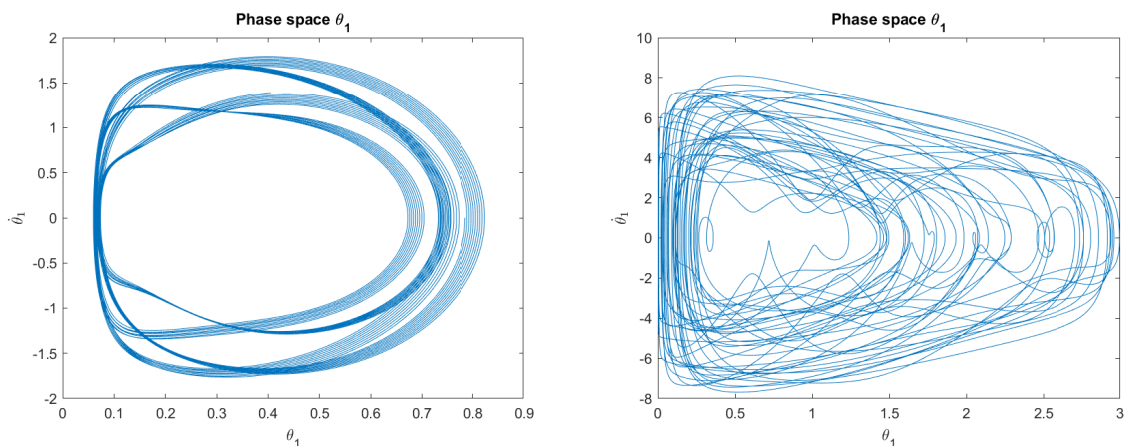
(a) Phase Space of the polar angle of the first pendulum in the simulation of the double pendulum experiencing a periodic motion.

(b) Phase Space of the polar angle of the first pendulum in the simulation of the double pendulum experiencing chaos.

Figure 3.5: The phase space plots of the polar angle of the first pendulum in the periodic and chaos simulation of the double pendulum. The x-axis shows the angle θ_1 and the y-axis shows the angular velocity $\dot{\theta}_1$. The plot for the periodic motion shows a regular pattern while the chaotic motion shows an irregular pattern containing multiple loops and spirals.
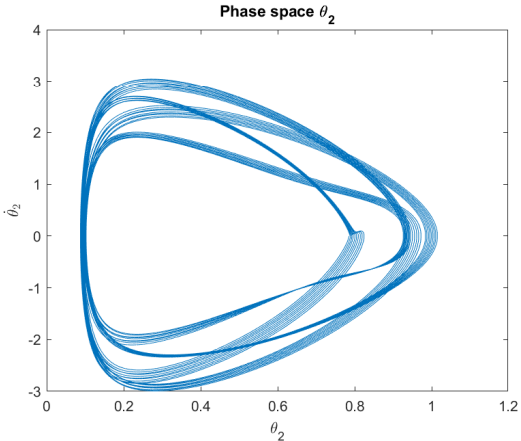
(a) Phase Space of the polar angle of the second pendulum in the simulation of the double pendulum experiencing a periodic motion.
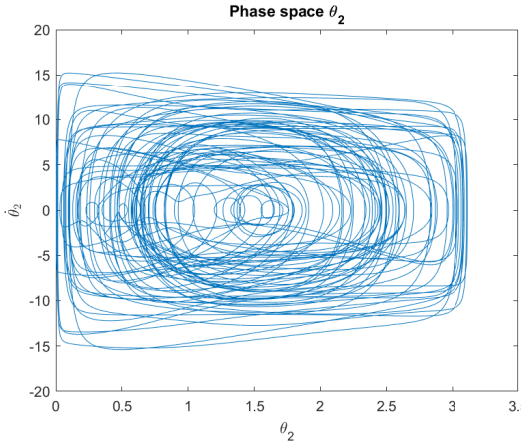
(b) Phase Space of the polar angle of the second pendulum in the simulation of the double pendulum experiencing chaos.

Figure 3.6: The phase space plots of the polar angle of the second pendulum in the periodic and chaos simulation of the double pendulum. The x-axis shows the angle θ_2 and the y-axis shows the angular velocity $\dot{\theta}_2$. The plot for the periodic motion shows a regular pattern while the chaotic motion shows an irregular pattern containing multiple loops and spirals.

4

String of Pendulums

After discussing the double pendulum, the model is extended to simulate a string of pendulums. In this chapter, the equations of motion in general form for a string of pendulums using Newton's second law will is described. Next is elaborated on the application of implicit Euler to construct the numerical model. Lastly, the nonlinear solver that was required to simulate the behaviour of a string of pendulums is presented.

4.1. String of Pendulums

After constructing the model for a double pendulum, the model is expanded to model a string of pendulum. A string of pendulums consists of a number of N pendulums that are connected to each other. By determining the equations of motion of a double pendulum, the terms that account for coupling between two pendulums were discovered. The coupling terms between the first and second pendulum of the string are of the same form as the coupling terms that occur between the second and third pendulum of the string, and so on [12]. With this information the equations of motion for a string of pendulum can be constructed in a general form.

The construction of the model for the string of pendulums was done by following the same steps as constructing the model for the double pendulum, but by applying other methods. Instead of the Lagrangian method the Newtonian method was used for constructing this model. The Newtonian method was also applied by Kim, Lee, and Yoo [16], who analysed the behaviour of a flexible hose in water by dividing the hose into nodal points and determining the equations of motion at each node. For the string of pendulums, it proved that the Newtonian method gave more clear insights on the forces at play and their orientations than using the Lagrangian method. Therefore, this method was found to be more easy to use for adding external forces and damping and adding constraints. Also, due to stability issues, an implicit integration scheme was used instead of semi-implicit. Later on in this section a more elaborated on these changes of method will be explained.
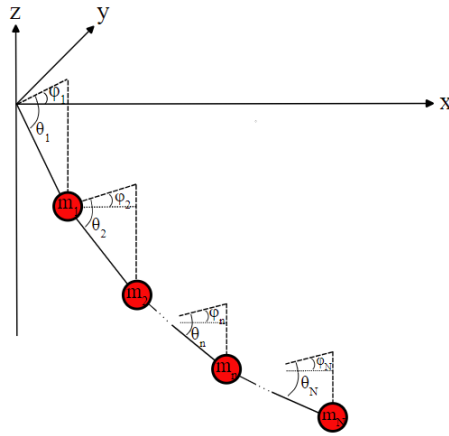
Figure 4.1: The configuration of a series of connected pendulums, ranging from 1 to N. The first pendulum is again fixed in the origin of the space-fixed coordinate system. Each pendulum has a mass and a polar and azimuth angle it makes relative to the previous pendulum.

The string consists of a variable number of N pendulums. The lengths and masses of each pendulum are described by the vectors (4.1) and (4.2). The letter n is used to indicate which pendulum is considered and N represents the final pendulum.

$$L = [L_1 \ L_2 \ ... \ L_n \ ... \ L_N]^T \tag{4.1}$$

$$m = [m_1 \ m_2 \ ... \ m_n \ ... \ m_N]^T \tag{4.2}$$

The position of each pendulum is described by the equations (4.3), (4.4), and (4.5).

$$x_n = x_{n-1} + L_n cos(\theta_n) cos(\phi_n) \tag{4.3}$$

$$y_n = y_{n-1} + L_n cos(\theta_n) sin(\phi_n) \tag{4.4}$$

$$z_n = z_{n-1} - L_n sin(\theta_n) \tag{4.5}$$

4.2. Analytical Description

The Newtonian method is applied to analytically describe the string of pendulums. The Newtonian method is based on Newton's second law, which states that the acceleration of an object is dependent on the mass of the object and the forces acting on the object. Newton's second law is used to construct the equations of motion at each pendulum bob, denoted by $\boldsymbol{n}$. Where $\boldsymbol{F}_n = [F_{x_n}, F_{y_n}, F_{z_n}]^T$ and $\boldsymbol{a}_n = [a_{x_n}, a_{y_n}, a_{z_n}]^T$.

$$\sum \boldsymbol{F}_n = m_n \boldsymbol{a}_n \tag{4.6}$$

(a) Forces acting on the string of pendulums in xz plane.

(b) Forces acting on the string of pendulums in xy plane.
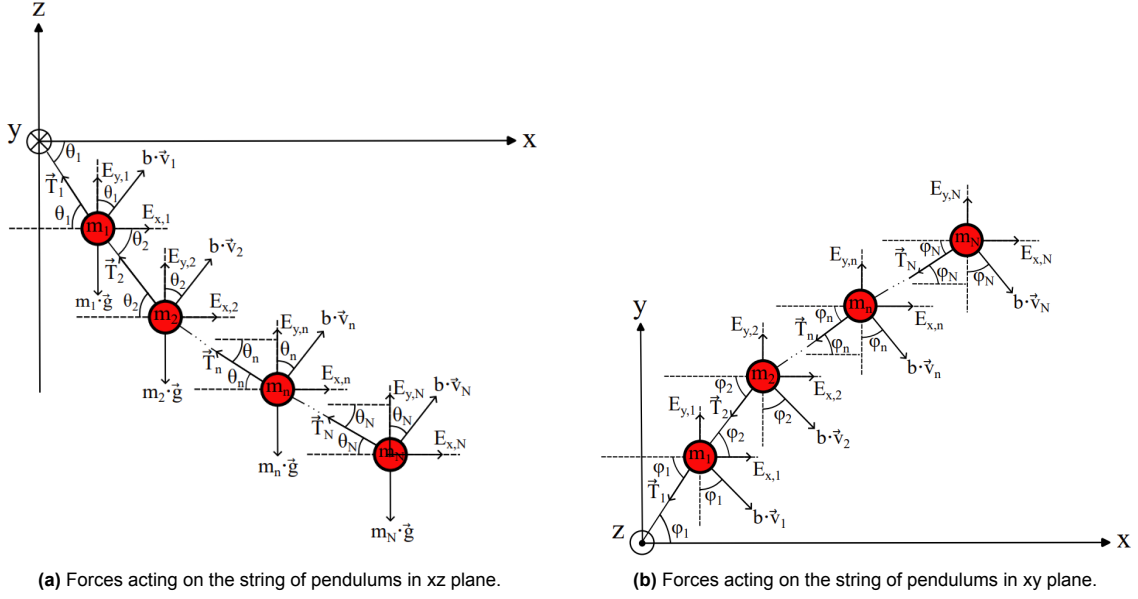
Figure 4.2: A representation of the forces acting on a string of pendulums in two different views. Each pendulum experiences a gravitational force, a dissipative force due to its motion, and external forces can be applied to the pendulums. Each pendulum bob has a tension force pulling on it from both sides expect for the last pendulum N, which is only subject to one tension force

4.2.1. Static Equilibrium

When the system is in static equilibrium it is at rest. This means that each node must have an acceleration which is equal to zero, so the sum of the forces must be equal to zero. Since there is no motion, there is no damping force at play during static equilibrium. Solving the equations for static equilibrium (4.7), (4.8) and (4.9) results in the initial values of the system.

$$\sum F_{x_n} = T_{n+1}cos(\theta_{n+1})cos(\phi_{n+1}) - T_n cos(\theta_n)cos(\phi_n) + E_{x_n} = 0 \tag{4.7}$$

$$\sum F_{y_n} = T_{n+1}cos(\theta_{n+1})sin(\phi_{n+1}) - T_n cos(\theta_n)sin(\phi_n) + E_{y_n} = 0 \tag{4.8}$$

$$\sum F_{z_n} = T_n sin(\theta_n) - T_{n+1}sin(\theta_{n+1}) + E_{z_n} = 0 \tag{4.9}$$

Since the last pendulum in the string has no other pendulum attached to it, the equations of static equilibrium for the last pendulum become:

$$\sum F_{x_N} = -T_n cos(\theta_n)cos(\phi_n) + E_{x_n} = 0 \tag{4.10}$$

$$\sum F_{y_N} = -T_n cos(\theta_n)sin(\phi_n) + E_{y_n} = 0 \tag{4.11}$$

$$\sum F_{z_N} = T_n sin(\theta_n) + E_{z_n} = 0 \tag{4.12}$$

4.2.2. Equations of motion

When the system is out of its static equilibrium, dynamical behaviour is observed, in this case the acceleration does have a value. When the acceleration has a value, damping is introduced to the motion.

Damping

Two types of damping are taken into account, linear and quadratic damping. Linear damping b_l is proportional to the velocity of the pendulum and quadratic damping b_q is proportional to the velocity squared of the pendulum. The total dissipative force contribution due to damping can be found in general form in equation (4.13), and in equation (4.14) the vectorial equation is presented.

$$\boldsymbol{F}_{b_n} = b_l \, \boldsymbol{v}_n + b_q \, \boldsymbol{v}_n^2 \tag{4.13}$$

$$\begin{bmatrix} F_{b_n,x} \\ F_{b_n,y} \\ F_{b_n,z} \end{bmatrix} = b_l \begin{bmatrix} \dot{x}_n \\ \dot{y}_n \\ \dot{z}_n \end{bmatrix} + b_q \begin{bmatrix} \dot{x}_n^2 \\ \dot{y}_n^2 \\ \dot{z}_n^2 \end{bmatrix} \tag{4.14}$$

The velocity of each pendulum is described by the time derivative of their positions, as described in equations (4.15), (4.16), and (4.17). These equations are substituted into equation (4.14) to determine the damping into x, y and z direction.

$$\dot{x}_n = \dot{x}_{n-1} - L_n sin(\theta_n)cos(\phi_n)\dot{\theta}_n - L_n cos(\theta_n)sin(\phi_n)\dot{\phi}_n \tag{4.15}$$

$$\dot{y}_n = \dot{y}_{n-1} - L_n sin(\theta_n)sin(\phi_n)\dot{\theta}_n + L_n cos(\theta_n)cos(\phi_n)\dot{\phi}_n \tag{4.16}$$

$$\dot{z}_n = \dot{z}_{n-1} - L_n cos(\theta_n)\dot{\theta}_n \tag{4.17}$$

Acceleration

The acceleration of each node in the x, y, and z direction is determined by taking the second time derivative of the position of the node in spherical coordinates. The acceleration of each pendulum is presented in equations (4.18), (4.19), and (4.20). Due to the dependence of the position of pendulum n on the position of the previous pendulum, the accelerations are coupled. This again results in a coupled set of nonlinear equations of motion.

$$\begin{aligned} \ddot{x}_n = \ddot{x}_{n-1} &- L_n sin(\theta_n)cos(\phi_n)\ddot{\theta}_n - L_n cos(\theta_n)sin(\phi_n)\ddot{\phi}_n - L_n cos(\theta_n)cos(\phi_n)\dot{\theta}_n^2 \\ &- L_n cos(\theta_n)cos(\phi_n)\dot{\phi}_n^2 + 2L_n sin(\theta_n)sin(\phi_n)\dot{\theta}_n\dot{\phi}_n \end{aligned} \tag{4.18}$$

$$\begin{aligned} \ddot{y}_n = \ddot{y}_{n-1} &- L_n sin(\theta_n)sin(\phi_n)\ddot{\theta}_n + L_n cos(\theta_n)cos(\phi_n)\ddot{\phi}_n - L_n cos(\theta_n)sin(\phi_n)\dot{\theta}_n^2 \\ &- L_n cos(\theta_n)sin(\phi_n)\dot{\phi}_n^2 + 2L_n sin(\theta_n)cos(\phi_n)\dot{\theta}_n\dot{\phi}_n \end{aligned} \tag{4.19}$$

$$\ddot{z}_n = \ddot{z}_{n-1} - L_n cos(\theta_n)\ddot{\theta}_n + L_n sin(\theta_n)\dot{\theta}_n^2 \tag{4.20}$$

Total Equation of Motion

Using Newton's second law (4.6), the equations of motion per node are determined and presented in (4.21), (4.22) and (4.23). Where E represents the external force applied in x, y or z direction. $\boldsymbol{F}_b$ represents the damping force, which is opposed to the positive direction of the pendulum motion.

$$m_n \ddot{x}_n = \sum F_{x_n} = T_{n+1}cos(\theta_{n+1})cos(\phi_{n+1}) - T_n cos(\theta_n)cos(\phi_n) + E_{x_n} - F_{b_n,x} \tag{4.21}$$

$$m_n \ddot{y}_n = \sum F_{y_n} = T_{n+1}cos(\theta_{n+1})sin(\phi_{n+1}) - T_n cos(\theta_n)sin(\phi_n) + E_{y_n} - F_{b_n,y} \tag{4.22}$$

$$m_n \ddot{z}_n = \sum F_{z_n} = T_n sin(\theta_n) - T_{n+1}sin(\theta_{n+1}) + E_{z_n} - F_{b_n,z} \tag{4.23}$$

The equations of motion for the last node N become as presented in

$$m_N \ddot{x}_N = \sum F_{x_N} = -T_n cos(\theta_N)cos(\phi_N) + E_{x_N} - F_{b_N,x} \tag{4.24}$$

$$m_N \ddot{y}_N = \sum F_{y_N} = -T_N cos(\theta_N)sin(\phi_N) + E_{y_N} - F_{b_N,y} \tag{4.25}$$

$$m_N \ddot{z}_N = \sum F_{z_N} = T_N sin(\theta_N) + E_{z,N} - F_{b_N,z} \tag{4.26}$$

4.3. Numerical Method

This section introduces the numerical method used to discretise the equations for the string of pendulums, as well as the construction of the nonlinear solver designed to solve the set of nonlinear equations resulting from the discretisation.

4.3.1. Implicit Euler

For the single and double pendulum models, a semi-implicit integration scheme was used since this took less computational effort and provided enough stability. For a string of pendulums, the motion becomes even more complex than for the double pendulum, enlarging the change of numerical instability. Therefore, an implicit integration scheme in the form of (4.27) is used, enhancing the stability of the system.

$$y_{i+1} = y_i + dt\, f(t_{i+1}, y_{i+1}) \tag{4.27}$$

Using implicit Euler, the angles are discretised as follows;

$$\frac{\theta_{i+1} - \theta_i}{dt} = \dot{\theta}_{i+1} \tag{4.28}$$

$$\frac{\phi_{i+1} - \phi_i}{dt} = \dot{\phi}_{i+1} \tag{4.29}$$

$$\frac{\dot{\theta}_{i+1} - \dot{\theta}_i}{dt} = \ddot{\theta}_{i+1} \tag{4.30}$$

$$\frac{\dot{\phi}_{i+1} - \dot{\phi}_i}{dt} = \ddot{\phi}_{i+1} \tag{4.31}$$

For each pendulum there are five unknowns, namely θ_{i+1}, $\dot{\theta}_{i+1}$, ϕ_{i+1}, $\dot{\phi}_{i+1}$, and T_{i+1}. This means that 5 equations per pendulum are required to determine these unknowns. The set of equations per pendulum are presented below. The equations (4.32) and (4.33) are to update the velocity of the polar and azimuth angle. The other three equations (4.34), (4.35), and (4.36) represent the equations of motion and the equations (4.30) and (4.31) are substituted for the values of the accelerations of the polar and azimuth angle .

$$f_{1_n} = \frac{\theta_{n,i+1} - \theta_{n,i}}{dt} - \dot{\theta}_{n,i+1} = 0 \tag{4.32}$$

$$f_{2_n} = \frac{\phi_{n,i+1} - \phi_{n,i}}{dt} - \dot{\phi}_{n,i+1} = 0 \tag{4.33}$$

$$f_{3_n} = m_n\, \ddot{x}_{n,i+1} - \sum F_{x_{n,i+1}} = 0 \tag{4.34}$$

$$f_{4_n} = m_n\, \ddot{y}_{n,i+1} - \sum F_{y_{n,i+1}} = 0 \tag{4.35}$$

$$f_{5_n} = m_n\, \ddot{z}_{n,i+1} - \sum F_{z_{n,i+1}} = 0 \tag{4.36}$$

4.3.2. Nonlinear Solver

For each pendulum, this set of nonlinear equations must be solved at each time iteration to find a solution to the unknowns. A nonlinear solver is required to solve these equations. Matlab has an installed function "fsolve" which can apply three different algorithms to solve a system of nonlinear equations. However, fsolve approximates the Jacobian matrix required to solve the system, numerically. This is less robust than determining the Jacobian analytically. Determining the analytical Jacobian may increase stability and can improve the accuracy of the solution. However, constructing the Jacobian analytically also makes it more sensitive to calculation errors.

In this case, a nonlinear solver is constructed without the use of fsolve, but by applying Newton-Raphson. Newton-Raphson is an iterative method that must be employed at each time iteration to solve the set of nonlinear equations. Newton-Raphson is a numerical method that iteratively searches for the right values of the set of unknowns. The equations used to solve the unknowns must be transformed into a root finding problem by rewriting them into the form of $f(q_{i+1}) = 0$, as has been done in the equations (4.32) to (4.36).

Since there is not one but multiple nonlinear equations, the multivariate Newton-Raphson method must be applied (B.19).

$$Y_{k+1} = Y_k - J^{-1} F(Y_k) \tag{4.37}$$

Here k is the iteration of Newton-Raphson. Multiple iterations are executed to eventually find the right roots for the set of equations. J is the Jacobian, which is a matrix that consists of the partial derivatives of the functions with respect to the different variables. Equation B.19 must be solved at every time step. To use Newton-Raphson, initial conditions must be set. Next, root finding is used to compute the values for y at the next iteration. Thereafter, the obtained values will be substituted into the function vector and through root finding the values of y at the next iteration are found, and so on [29]. This process is repeated until the stopping criterion is met, which is equal to $|F(Y_k)| < \epsilon$. In this case, an epsilon of $\epsilon = 10^{-10}$ is applied.

In this case, the vector Y for each pendulum is represented by $Y = [\theta_{i+1}\ \dot{\theta}_{i+1}\ \phi_{i+1}\ \dot{\phi}_{i+1}\ T_{i+1}]^T$. The function vector consists of the functions described in the previous section $F = [f_1\ f_2\ f_3\ f_4\ f_5]^T$. The Jacobian of this system is equal to equation (4.38). For some scenarios the Jacobian became singular which caused the model to fail. A singular matrix means that the determinant of the Jacobian was close to zero or enormously large. This problem could be evaded by choosing a smaller time step or by changing the initial conditions.

$$J = \begin{bmatrix} \frac{\partial f_1}{\partial \theta_{i+1}} & \frac{\partial f_1}{\partial \dot{\theta}_{i+1}} & \frac{\partial f_1}{\partial \phi_{i+1}} & \frac{\partial f_1}{\partial \dot{\phi}_{i+1}} & \frac{\partial f_1}{\partial T_{i+1}} \\ \frac{\partial f_2}{\partial \theta_{i+1}} & \frac{\partial f_2}{\partial \dot{\theta}_{i+1}} & \frac{\partial f_2}{\partial \phi_{i+1}} & \frac{\partial f_2}{\partial \dot{\phi}_{i+1}} & \frac{\partial f_2}{\partial T_{i+1}} \\ \frac{\partial f_3}{\partial \theta_{i+1}} & \frac{\partial f_3}{\partial \dot{\theta}_{i+1}} & \frac{\partial f_3}{\partial \phi_{i+1}} & \frac{\partial f_3}{\partial \dot{\phi}_{i+1}} & \frac{\partial f_3}{\partial T_{i+1}} \\ \frac{\partial f_4}{\partial \theta_{i+1}} & \frac{\partial f_4}{\partial \dot{\theta}_{i+1}} & \frac{\partial f_4}{\partial \phi_{i+1}} & \frac{\partial f_4}{\partial \dot{\phi}_{i+1}} & \frac{\partial f_4}{\partial T_{i+1}} \\ \frac{\partial f_5}{\partial \theta_{i+1}} & \frac{\partial f_5}{\partial \dot{\theta}_{i+1}} & \frac{\partial f_5}{\partial \phi_{i+1}} & \frac{\partial f_5}{\partial \dot{\phi}_{i+1}} & \frac{\partial f_5}{\partial T_{i+1}} \end{bmatrix} \tag{4.38}$$

For every pendulum attached to the string, the system of equations grows. The total function vector will have a size of $F_{tot} = [5\,N, 1]$, as will the vector containing the unknowns $Y_{tot} = [5\,N, 1]$. The Jacobian matrix will grow in size by also a factor of 5, resulting in $J_{tot} = (5\,N, 5\,N)$. The general form of the function vector can be found in appendix B.

5

The Mussel Dropper

To model a mussel dropper, the string of pendulums constructed in the previous chapter must be fixed at its outer node. The outer end of the string is fixed by adding constraints to the last pendulum. The changes made to the model in order to obtain a mussel dropper are discussed in this chapter. Furthermore, the application of the Crank-Nicolson method is explained and a time convergence analysis of the model is performed.
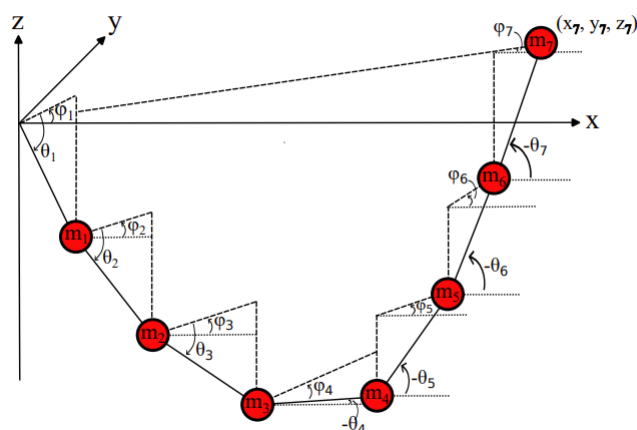
Figure 5.1: The configuration of a string of pendulums where the last pendulum is fixed at the coordinates (x_N, y_N, z_N). The polar angle is now defined as positive when the rotation is counterclockwise.

5.1. Analytical Description

In this section a analytical description of the static equilibrium and the dynamic state of the mussel dropper are described. Since the mussel dropper is described by a series of connected pendulums, the flexibility of the mussel dropper is taken into account. Knysh et al. [17] has conducted a research to numerically model a submerged longline. However, the droppers are modelled using the cantilever beam model, which indicates a rigid structure. A string of pendulums can better capture the deformability and curvature of a mussel dropper.

5.1.1. Static Equilibrium

For the mussel dropper in static equilibrium, the equations (4.7), (4.8), and (4.9) again represent the system in rest. But since the last pendulum is now fixed in space, the equations for the last pendulum (4.10) to (4.12), are replaced with the necessary boundary conditions for that pendulum. There is

a constraint on the x position of the last pendulum (5.1), which states that the x position of the last pendulum must be equal to the sum of the x positions of all the previous pendulums. The same is true for the y and z positions of the last pendulum, resulting in the boundary conditions as shown in equations (5.2) and (5.3).

$$x_N = \sum L_N \cos(\theta_N) \cos(\phi_N) \tag{5.1}$$

$$y_N = \sum L_N \cos(\theta_N) \sin(\phi_N) \tag{5.2}$$

$$z_N = \sum -L_N \sin(\theta_N) \tag{5.3}$$

In static equilibrium, the mussel dropper represents a catenary curve. Therefore, the equations for a catenary curve, see appendix C , are applied to find an initial guess for the tensions and positions of the system at rest. Input needed to determine the tensions and positions at rest are the distances between the first and final node in x and y direction, and the vertical distance between the first and final node. Each pendulum bob represents a node in the curve. The total number of nodes is equal to N+1, accounting for the origin where there is no pendulum bob. Also, the total mass and length of the dropper are required. The initial guess from the catenary curve equations help solve the equations of static equilibrium, which again serves as an initial guess for the actual time integration.

5.1.2. Equation of Motion
The equations of motion of the mussel dropper are again described by the equations as provided in chapter 4, (4.21) to (4.23). Again, the equations of motion for the last pendulum are now replaced by the equations for the boundary conditions, so (4.24) to (4.26) are replaced with equations (C.4) to (C.6).

5.2. Numerical Method
In this section is described how Crank-Nicolson is applied to the numerical model and how this adjusted the nonlinear solver. Also, a time convergence analysis for the numerical model is performed.

5.2.1. Crank-Nicolson
For the string of pendulums, implicit Euler was applied due to its advantages concerning the stability of the model. However, implicit Euler adds a large amount of numerical damping to the model. Due to the large amount of numerical damping, the motion of the mussel dropper came to a stop quickly. The numerical damping had to be reduced, so that the physical damping in the equations of motion could be used to find the right amount of damping. A way to reduce numerical damping is to use a smaller time step. However, this vastly increases the computation time. To reduce the numerical damping and still obtain a high level of stability, the Crank-Nicolson method is applied 5.2.
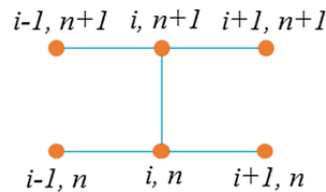
Figure 5.2: A representation of the Crank-Nicolson scheme, which is the weighted average between an explicit and implicit scheme and is obtained when $\gamma = 0.5$. Crank-Nicolson provides better stability than a fully explicit method, and has less numerical damping than a fully implicit method. Retrieved from Liu [19]

The Crank-Nicolson method is a method for numerically solving partial differential equations. This method applies discretisation in both time and space and then combines implicit and explicit terms to achieve a weighted average. Combining Crank-Nicolson with the θ-method gives the opportunity to alter the value of this weight, making the scheme either more implicit or more explicit. Since θ is already used as the identification of the polar angel in this research, the letter γ is used. When $\gamma = 1$ the scheme

is completely implicit and when $\gamma = 0$ the scheme is completely explicit. When $\gamma = \frac{1}{2}$ the original Crank-Nicolson scheme is obtained. In this method, γ is a parameter that determines the weighting between the implicit and explicit contributions. The integration scheme combining Crank-Nicolson and the θ-method is shown in equation (5.4). In this scheme, u represents the vector containing the angles, angular velocities, and tension for each pendulum.

$$\frac{u_{i+1} - u_i}{dt} = \gamma\, f(t_{i+1}, u_{i+1}) + (1 - \gamma)\, f(t_i, u_i) \tag{5.4}$$

Using this Crank-Nicolson method and applying a γ parameter less than 1 can already reduce the amount of numerical damping. To reduce the numerical damping as much as possible, the ideal value for γ would be 0.5. However, applying this value did not result in a stable model, therefore the parameter was set to $\gamma = 0.51$. This reduced the amount of numerical damping greatly when compared to the fully implicit method, but still provided enough stability and didn't require a too small time step. The set of 5 equations for every pendulum remains the same as for the string of pendulums, but is now discretised using the method described in this section. The complete integration scheme for each pendulum can be found in appendix C.

The set of equations that are constructed for the last pendulum differ from the set of equations for the other pendulums. The set of equations for the last pendulum becomes as described by equations (5.5) to (5.9).

$$f_{1_N} = \frac{\theta_{n,i+1} - \theta_{n,i}}{dt} - \gamma\, \dot{\theta}_{n,i+1} - (1 - \gamma)\, \dot{\theta}_{n,i} = 0 \tag{5.5}$$

$$f_{2_N} = \frac{\phi_{n,i+1} - \phi_{n,i}}{dt} - \gamma\, \dot{\phi}_{n,i+1} - (1 - \gamma)\dot{\phi}_{n,i} = 0 \tag{5.6}$$

$$f_{3_N} = \sum L_n\, cos(\theta_{n,i+1})\, cos(\phi_{n,i+1}) = 0 \tag{5.7}$$

$$f_{4_N} = \sum L_n\, cos(\theta_{n,i+1})\, sin(\phi_{n,i+1}) = 0 \tag{5.8}$$

$$f_{5_N} = \sum -L_n\, sin(\theta_{n,i+1}) = 0 \tag{5.9}$$

5.2.2. Nonlinear Solver

There are again 5 unknowns per node, θ_{i+1}, $\dot{\theta}_{i+1}$, ϕ_{i+1}, $\dot{\phi}_{i+1}$, T_{i+1}. The nonlinear solver as constructed in chapter 4 is used to solve the set of nonlinear equations. The function vector is constructed by the functions defined in appendix C and by the equations for the last pendulum (5.5) to (5.9).

A problem that arose using the nonlinear solver, was that for certain initial conditions the solver did not converge to a solution. Altering the time step or changing the initial conditions could remove this problem.
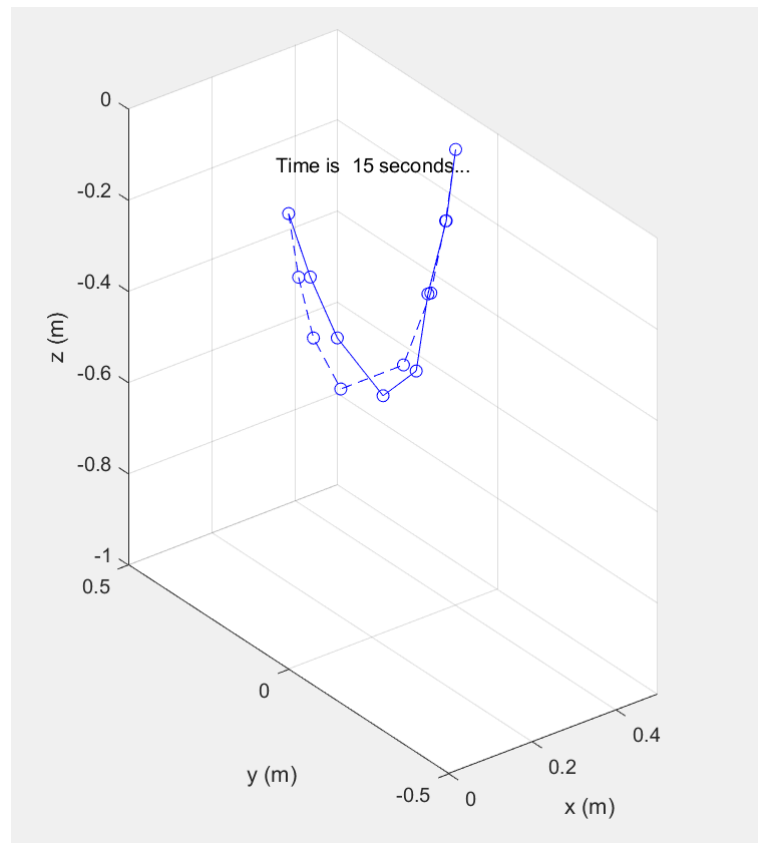
Figure 5.3: A snapshot of a simulation of the 3D model mussel without physical damping. The first pendulum is fixed at the origin of the coordinate system, the last pendulum is fixed at $(0.4, 0, 0)$. The second pendulum, so the third node, was given a force in the positive y direction which moved the dropper from its rest position. The force was removed after 15 seconds which triggered the motion of the dropper.

5.2.3. Time Convergence Analysis

To determine the right time step that should be applied to the model, a time convergence analysis is conducted. The root mean squared error of the results from one time step with the results from a previous time step are determined. When the error reaches zero, the time step for which the model provides accurate results is obtained. An analysis has been done for the 2D and 3D model. For the 2D model a time step of $dt = 0.01$ is small enough for reliable results, as can be seen from figure 5.4. The time convergence analysis for the 3D model can be found at appendix C.5, for the 3D model also a time step of $dt = 0.01$ is a small enough time step for reliable results.
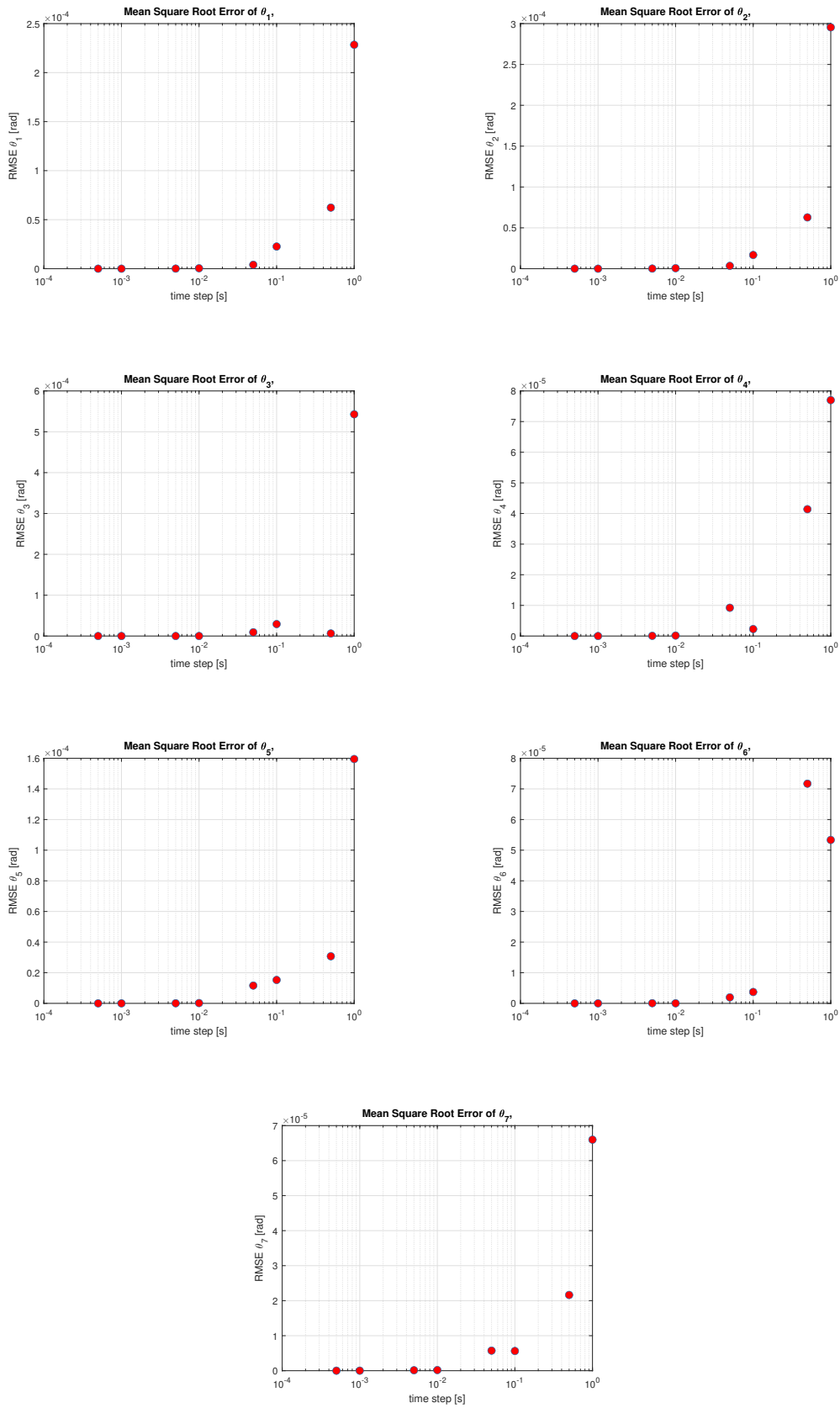
Figure 5.4: A time convergence analysis of the model for the 2D mussel dropper. The square mean root error per pendulum is plotted against different time steps on a logarithmic scale. A time step of $dt = 10^{-2}$ is a sufficiently small time step.

<div style="text-align: right; font-size: 3em;">6</div>

Mussel Dropper in Waves

In order to achieve the main objective of this thesis, a wave force must be applied to the 3D model of the dropper. First, some background information on the behaviour of a pendulum in waves is provided. Next, the wave velocity and acceleration are determined by applying the potential flow theory. Thereafter, an expression for the wave force is provided by incorporating Morison's equation. At last is explained how the wave force is applied to the numerical model and how a fast Fourier transform can provide the data in frequency domain.

6.1. General Information

Bos and Wellens [3] researched the behaviour of a pendulum excited by waves of different wavelengths. When a pendulum is submerged in water, the pendulum is subjected to the effect of added mass. Bos and Wellens [3] expects that when the pendulum is wet, the natural period of the system will become longer due to the added mass. Another effect described by Bos and Wellens [3] is that a shift in the mean position of the pendulum will occur when the pendulum is subjected to nearly sinusoidal waves with no mean and a period that is significantly shorter than the natural period of the pendulum. This shift in the mean is a demonstration of the nonlinear character of the response of the pendulum. They also noticed that in the surface elevation, there is a pronounced maxima and irregularities of the maxima and that those are transferred to the motion of the pendulum.

Bos and Wellens [3] further observes that resonance occurs when the period of the pendulum is close to the wave's period. Determining this resonance period of the pendulum involves monitoring the shift from in phase to out of phase between the wave height and the pendulum response.

Another effect that they expect is that due to the quadratic drag, when the wave amplitude is enlarged by 10%, the velocity will be 10% higher, and thus the response should expect an increase of around 21%. However, the increase in response was not observed for most wave types, therefore Bos and Wellens [3] concluded that the sensitivity of the response amplitude of the pendulum to changes in the wave amplitude is largely influenced by the wetness. The wetness is defined as the level of submergence of the pendulum. The wave that showed the least sensitivity to the change in amplitude, was the wave that excited the pendulum near its natural frequency [3].

A final note that is given is the suggestion that the primary drivers of nonlinear behaviour are the wetting and drying and the drag.

6.2. Ocean Surface Waves

To determine the kinematics of the wave the potential flow theory is applied. The potential flow theory is a linear theory that is based on the assumption that the external flow around the system is inviscid and irrotational. To apply the potential flow theory to surface waves, it is assumed that the wave steepness is neglectable. Then, the wave profile of a propagating harmonic wave in the x-y plane can be described by equation (6.1).

$$\eta(x, y, t) = \eta_a \, cos(k \, cos(\mu) \, x + k \, sin(\mu) \, y - \omega \, t + \epsilon_w) \tag{6.1}$$

Since linear behaviour of the waves is assumed, the total wave elevation in a certain sea state can be defined by the sum of all the wave components present in that sea state, as described in equation (6.2). In this equation c_w is the total number of wave components and c indicates the wave component. The amplitude of the wave is described by η_a, the frequency of the wave by ω and the wave number by k. In these equations x, y and z represent the location where the wave is observed. The angle μ describes the incoming angle of the wave and the phase of the wave ϵ_w accounts for the phase difference between the wave components.

$$\eta(x, y, t) = \sum_{c=1}^{c_w} \eta_{a,c} \, cos(k_c \, cos(\mu) \, x + k_c \, sin(\mu) \, y - \omega_c \, t + \epsilon_{w,c}) \tag{6.2}$$

According to the potential flow principle, the potential of a wave that is dependent on the water depth can be described by equation (6.3). When the potential is dependent on the water depth, the water is assumed to be shallow and long waves are present. In the case of deep water, short waves are present and the potential becomes independent of the water depth. The water is considered to be deep when $\frac{h}{\lambda} > \frac{1}{2}$. In this case, shallow water is assumed.

$$\Phi_w = \frac{\eta_a \, g}{\omega} \, \frac{cosh(k \, (h + z))}{cosh(kh)} \, sin(k \, cos(\mu) \, x + k \, sin(\mu) \, y - \omega \, t + \epsilon_w) \tag{6.3}$$

The wave potential is used to determine the water particle kinematics. The velocity of the wave in 3D are obtained by taking the partial derivative of the potential with respect to the x, y and z coordinate. The sum of the velocities and accelerations for each wave component are taken to obtain the total velocity and acceleration in the different directions, as was explained by Zanten [34]. The dispersion relationship $kg = \frac{\omega^2}{tanh(kh)}$ is used to rewrite the equations in their final form, as presented by the equations (6.4),(6.5), and (6.6). The dispersion relationship is an expression that relates the wave frequency to the wave number.

$$u_{w_x} = \frac{\partial \Phi_w}{\partial x} = \sum_{c=1}^{c_w} \eta_{a,c} \, \omega_c \, cos(\mu) \, \frac{cosh(k_c \, (h + z))}{sinh(k_c \, h)} \, cos(k_c \, x \, cos(\mu) + k_c \, y \, sin(\mu) - \omega_c \, t + \epsilon_{w,c}) \tag{6.4}$$

$$u_{w_y} = \frac{\partial \Phi_w}{\partial y} = \sum_{c=1}^{c_w} \eta_{a,c} \, \omega_c \, sin(\mu) \, \frac{cosh(k_c \, (h + z))}{sinh(k_c \, h)} \, cos(k_c \, x \, cos(\mu) + k_c \, y \, sin(\mu) - \omega_c \, t + \epsilon_{w,c}) \tag{6.5}$$

$$u_{w_z} = \frac{\partial \Phi_w}{\partial z} = \sum_{c=1}^{c_w} \eta_{a,c} \, \omega_c \, \frac{sinh(k_c \, (h + z))}{sinh(k_c \, h)} \, sin(k_c \, x \, cos(\mu) + k_c \, y \, sin(\mu) - \omega_c \, t + \epsilon_{w,c}) \tag{6.6}$$

The velocity vector of one wave particle becomes $n = [u_{x_n} \; u_{y_n} \; u_{z_n}]^T$

The wave acceleration is determined by taking the time derivative of the wave velocity. This results in equations (6.7), (6.8), and (6.9).

$$\dot{u}_{w_x} = \frac{du_{w_x}}{dt} = \sum_{c=1}^{c_w} \eta_{a,c} \, \omega_c^2 \, cos(\mu) \, \frac{cosh(k_c \, (h + z))}{sinh(k_c \, h)} \, sin(k_c \, x \, cos(\mu) + k_c \, y \, sin(\mu) - \omega_c \, t + \epsilon_{w,c}) \tag{6.7}$$

$$\dot{u}_{w_y} = \frac{dv_{w_z}}{dt} = \sum_{c=1}^{c_w} \eta_{a,c} \, \omega_c^2 \, sin(\mu) \, \frac{cosh(k_c \, (h + z))}{sinh(k_c \, h)} \, sin(k_c \, x \, cos(\mu) + k_c \, y \, sin(\mu) - \omega_c \, t + \epsilon_{w,c}) \tag{6.8}$$

$$\dot{u}_{w_z} = \frac{dv_{w_z}}{dt} = \sum_{c=1}^{c_w} -\eta_{a,c} \, \omega_c^2 \, \frac{sinh(k_c \, (h + z))}{sinh(k_c \, h)} \, cos(k_c \, x \, cos(\mu) + k_c \, y \, sin(\mu) - \omega_c \, t + \epsilon_{w,c}) \tag{6.9}$$

The acceleration vector of one wave particle becomes $\dot{u}_n = [\dot{u}_{x_n} \; \dot{u}_{y_n} \; \dot{u}_{z_n}]^T$

6.3. Morison's Equation

A cylinder experiences hydrodynamic forces as a result of the combined effect of increased flow velocity around the cylinder and flow separation from the cylinder's surface, which results in drag and inertia forces [1]. The drag force is a dissipative force that opposes the motion of a solid body moving through a fluid and depends on the speed, size, and shape of this body, according to Dourmashkin [9]. The inertial force, on the other hand, is the force that keeps the fluid moving against the viscous forces.

The force on a small structure due to these hydrodynamic forces can be computed by using Morison's equation (6.10). The first part of Morison's equation represents the contribution of the wave force due to drag. The second part of the equation represents the contribution of the wave force due to inertia. In this equation C_D is the drag coefficient. C_M is the inertia coefficient and is equal to $C_M = 1 + C_A$, where C_A represents the added mass coefficient. D_{cyl} is the diameter of the cylinder.

$$F(t) = \frac{\pi}{4} \rho D_{cyl}^2 C_M \dot{u}(t) + \frac{1}{2} \rho D_{cyl} C_D u(t)|u(t)| \tag{6.10}$$

Morison's equation is an empirical formula that is constructed in order to include the inertia and drag forces on a small cylinder. These forces are dependent on the drag and inertia coefficients, which are determined experimentally in either a laboratory or from field measurements [5]. Morison's equation is only valid when the extension of a body along the wave direction is significantly smaller than the wavelength, so only for slender bodies (6.11).

$$\frac{D_{cyl}}{\lambda} < 0.05 \tag{6.11}$$

Zhao et al. [35] describes the Morison equation as a semi-empirical equation for hydrodynamic forces on an object along the direction of incoming waves. He explains that Morison's equation is a combination of three force components. The first component is the Froude-Krylov force due to the pressure field generated by undisturbed waves. The second component is the contributing force due to the inertia of the surrounding fluid that needs to be accelerated, also called the added mass. The last component is the contribution due to viscous drag.

Techet [33] notes that if a vertical cylinder is subject to a current with a horizontal velocity changing both in time and over the depth, so vertically in the z-direction, Morison's formula needs to be evaluated for a small section of the cylinder at each depth and integrated to get the total force acting on the body.

In the case that a vertical cylinder is moving with a certain velocity within a fluid that is also moving with a certain velocity, Morison's equation must be rewritten, which yields equation (6.12). In this equation the velocity and acceleration of the pendulum bob is denoted by u_p and $\dot{u}_p$.

$$F_w = \frac{\pi}{4} \rho_f D_{cyl}^2 C_M (\dot{u}_w - \dot{u}_p) + \frac{1}{2} \rho_f D_{cyl} C_D (u_w - u_p)|(u_w - u_p)| \tag{6.12}$$

6.4. Application in Model

To apply Morison's equation to the mussel dropper, every pendulum bob is seen as a small cylinder. The external force contributions in the equations of motion are substituted with Morison's equation, as shown in (6.13). The wave force is discretised using the Crank-Nicolson method as described in section 5.2.

$$\begin{bmatrix} E_{x_n} \\ E_{y_n} \\ E_{z_n} \end{bmatrix} = \begin{bmatrix} \frac{\pi}{4} \rho_f D^2 C_M (\dot{u}_{w_x} - \ddot{x}_n) + \frac{1}{2} \rho_f D C_D (u_{w_x} - \dot{x}_n)|(u_{w_x} - \dot{x}_n)| \\ \frac{\pi}{4} \rho_f D^2 C_M (\dot{u}_{w_y} - \ddot{y}_n) + \frac{1}{2} \rho_f D C_D (u_{w_y} - \dot{y}_n)|(u_{w_y} - \dot{y}_n)| \\ \frac{\pi}{4} \rho_f D^2 C_M (\dot{u}_{w_z} - \ddot{z}_n) + \frac{1}{2} \rho_f D C_D (u_{w_z} - \dot{z}_n)|(u_{w_z} - \dot{z}_n)| \end{bmatrix} \tag{6.13}$$

7

Experiment

An experiment is conducted to validate the outcomes of a numerical model that simulates the dynamic behaviour of a series of connected pendulums suspended like a mussel dropper. This experiment will also contribute to determining the for now still unknown damping coefficient of the numerical model. The mussel dropper will be released from a certain height and a camera will capture the motion. The video of the motion will be processed by a script written in Matlab that can determine the positions of the nodes of the experimental model.

In this chapter the experimental and model setup are discussed. Then the calibration of the camera is presented and the post-processing of the results is elaborated on.

7.1. Experimental Setup

In this section, the experimental setup is presented. First, will be elaborated on the construction of the model dropper. Next, the setup of the framework and the additional necessities are discussed. Lastly, the camera settings and calibration of the camera are taken into account.

7.1.1. Model Dropper

The mussel dropper is modelled as a series of 7 connected compound pendulums. The compound pendulum is a pendulum that has an extended mass instead of a massless string with a point mass attached to the end. For the construction of the model dropper, two pendulums were designed, as shown in figure 7.1 and figure 7.2.
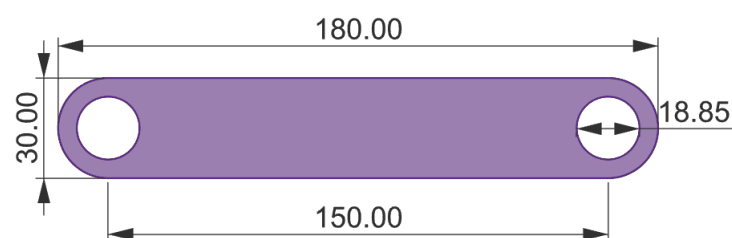
Figure 7.1: A drawing in Rhino of pendulum type A. This is the pendulum in which the bearings are placed. The model dropper will have four pendulums of type A.
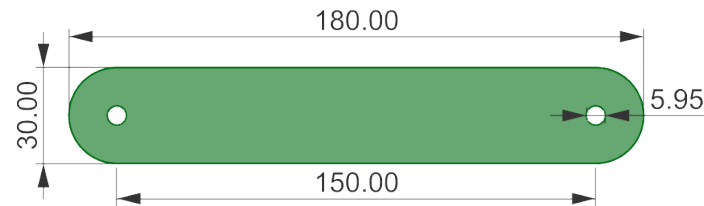
Figure 7.2: A drawing in Rhino of pendulum type B. This is the pendulum is placed between two pendulums of type A. A screw is used to connect both pendulums. The model dropper will have three pendulums of type A.

The complete dropper will consist of 4 pendulums of type A and 3 pendulums of type B, which will be attached alternately. The first and last pendulums are of type A. Smooth bearings will be placed in pendulum A, ensuring that the pendulums can rotate around their axis without too many losses due to friction. The pendulums are connected by screws. Each screw represents a node in the dropper model, so in total there are 8 nodes. The tops of the screws are made black by applying a black sticker on it. These black stickers have a reflecting circle in the middle which makes them better detectable for the camera.

Figure 7.3: The model dropper in the experimental setup. The two outer pendulums are placed 0.4 metres apart. Each node on the mussel dropper has a circle attached to it which is used to determine the positions later on.

7.1.2. Frame setup

The model dropper will be attached to a frame, keeping the two outer ends of the dropper fixed and making sure that the dropper can move without obstruction. The material of the frame will be item beams, which is a modular construction system. The base of the frame will be a T-shaped profile which is convenient because then only two beams have to be leveled and that decreases the chance of incorrect measurements. In order to obtain reliable measurements everything in the setup should be leveled and not displaced afterwards. The main frame is a square of item beams and there are two beams connecting the T profile to the main frame for stability and strength. Vibrations in and deflections of the framework must be reduced as much as possible so that they do not influence the motion of the loop. The model dropper is attached to the framework by two screws. Since the outer ends of the

dropper have smooth bearings, the pendulum can rotate freely around the outer nodes. A drawing of the frame is shown in figure 7.4a and 7.4b.

   During the experiment, multiple scenarios are tested. The nodes of the dropper should be able to be released from different heights. To ensure this, a small screw is attached to the top beam. This screw is used to tie a fishing line to. The other end of the fishing line can be attached to one of the pendulums, bringing it in the desired position, as can be seen in figure 7.12. Finally, a background plate will be placed in the main frame of the frame. The goal of the background plate is to increase the contrast between the model dropper and its surrounding environment. By increasing the contrast, the nodes are more easy detected during the processing of the test runs.
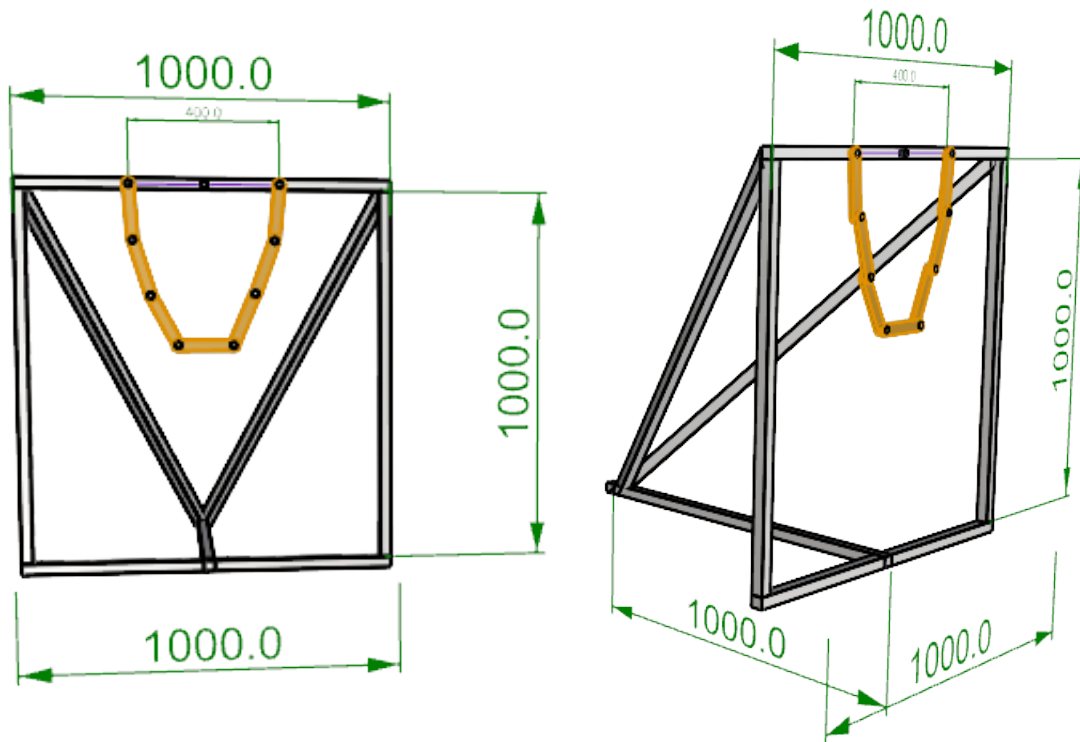
(a) Front view of the experimental setup with the dimensions provided in millimeters and drawn in Rhino.

(b) Side view of the experimental setup with the dimensions provided in millimeters and drawn in Rhino.

7.2. Camera

A camera is used to capture the motion of the loop. The recordings of the camera are used to process the data in Matlab. The settings of the camera must be such that the recordings can be divided into clear frames. The camera will be placed on a tripod that assures that the camera is leveled and does not move throughout the recording. Two LED panel lights are placed behind the camera to enhance the contrast between the model dropper and the background and between the dropper and the circles. The LED lights were placed 125 centimeters from the model dropper, the camera was positioned at 80 centimeters from the model dropper. The legs of the tripod were positioned 130 centimeters apart. A software, Camera Control Pro 2, developed by Nikon was used to operate the camera remotely from a laptop.

Initial conditions double 3D model	
Camera type	Nikon
Lens type	NIKKOR Z 14-30mm f/4 S
focal distance	30 [mm]
Shutter speed	$\frac{1}{640}$ [s]
Diaphragma	$F9$
ISO	$A51200$
Lens	30
LED type	BRESSER SH-1200 Slimline LED Lamp

Table 7.1: An overview of the camera settings and information on the camera and lens type. At last, the type of LED lights are defined.

The complete setup is presented in figures 7.5a and 7.5b.

(a) An image of the front of experimental setup. A camera and two LED lights are placed in front of the framework. The camera detects the motion of the model dropper and the checkerboard connected to the framework is used for calibrating the camera.

(b) An image of the back of the experimental setup. A framework of item profiles is constructed in order to attach the model dropper to. The framework has a T-profile as basis in order to decrease the number of parts that need to be leveled.

7.2.1. Calibration

Before starting the experiment the camera must be calibrated. A camera lens distorts the picture and this distortion can be removed by calibrating the camera. The distortion can be radial or tangential. Radial distortions causes straight lines to appear curved. Tangential distortions occurs when the lens of the camera is not perfectly aligned with the image sensor. To remove these distortion coefficients, the camera parameters must be estimated. Matlab has a built-in camera calibrator app that will be employed for the calibration. In order to conduct the calibration, a calibration pattern must be placed in view of the camera. A checkerboard is used in this case. The checkerboard is placed as far to the side as possible, since that is where the distortion is the largest. A camera has intrinsic and extrinsic parameters and to estimate these parameters, Matlab needs multiple images of the experimental set-up with the checkerboard also in the picture. By making multiple 2D images of a 3D setting from somewhat differing angles, Matlab can remove the distortion. The camera calibrator app provides the new intrinsic and extrinsic camera parameters and the lens distortion parameters. Now, the distortion can be removed from the image and therefore the image returns a reliable representation of the motion of the loop. The camera must not be brought out of its position after the calibration. A different camera

position requires a new calibration. Because the camera was controlled remotely, touching the camera, and thus potentially moving it, was avoided.
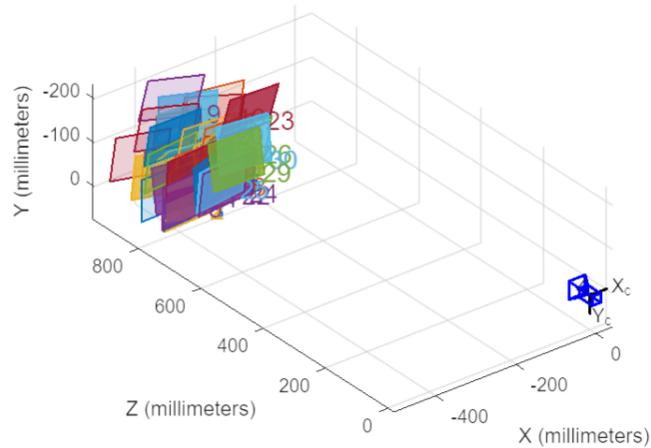
Figure 7.6: How the Calibrator app in Matlab uses multiple 2D images to help determine the 3D view and remove the distortion.

Another reason why calibration of the camera is needed is to get the position of the pendulums in real-life units. By retrieving the position of the pendulums from a picture, the positions are provided in pixels, but the positions are needed in centimeters. Again, the checkerboard is used for this. The dimensions of the squares on the checkerboard are precisely known. By placing the checkerboard in the same frame as the loop, the camera calibrator app can determine the positions of the pendulums in centimeters.
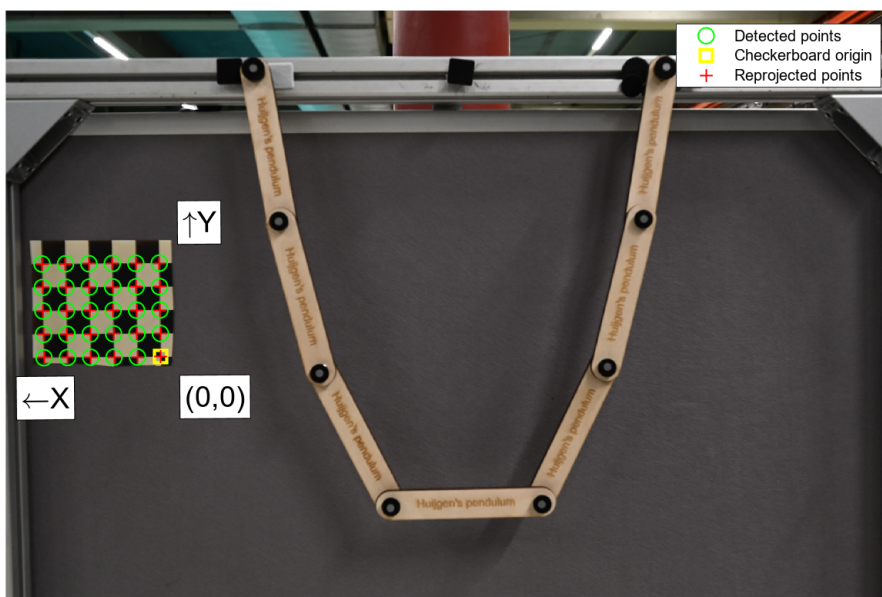
Figure 7.7: The calibrated camera detects the checkerboard's pattern. The size of the squares on the pattern are known. Using the calibrator app in Matlab the coordinates of the dropper in the image can be transformed from pixels to real world coordinates.

Matlab determined the following calibration parameters as presented in table 7.2.

Parameter	Range	Unit
Image size	$[2016, 3024]$	[px]
Radial distortion	$[-0.0494, 0.0301]$	[-]
tangential distortion	$[0, 0]$	[-]
Focal length	$[2.5430\,10^3, 2.5477\,10^3]$	[px]
Principal point	$[1.5720\,10^3, 1.0134\,10^3]$	[px]

Table 7.2: After calibration Matlab determined the calibration parameters of the camera.

The overall mean reprojection error is equal to 0.15 pixels, as shown in figure (7.8). The x-axis in this figure represents the image and the y-axis the mean reprojection error for that image. The reprojection error is the distance between a pattern keypoint detected in a calibration image, and a corresponding world point projected into the same image.
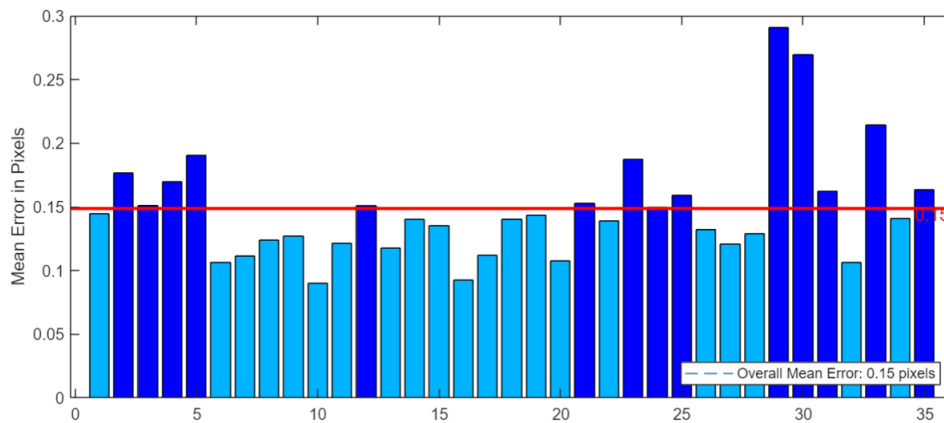
Figure 7.8: A plot of the reprojection error per image used for calibration. The overall mean reprojection error is equal to 0.15 pixels. The images having a larger error than the overall mean error are colored dark blue.

7.3. Post-Processing

During the experiment, five scenarios were tested. The first three scenarios are presented in this chapter, the other two can be found in appendix E.

Scenario A: *Model dropper excited at pendulum 1.*
The mussel dropper will be subject to wave forces, wave forces have the most influence on the motion of the loop near the surface. Therefore, it is important to know how the loop behaves when it is excited at pendulum 1. So, pendulum 1 is removed from its equilibrium position.

Scenario B: *Model dropper excited at pendulum 2.*
When the loop is excited at pendulum 2, a different motion will be seen than in scenario A. The second pendulum is brought at a height where when the pendulum is released, the motion becomes not too large. If the motion becomes too large the pendulums of the model dropper will collide and that will influence the behaviour of the dropper. The release height is adjusted so that the motion is only determined by this release.

Scenario C:*Model dropper excited at pendulum 3.*
The loop is excited at the third pendulum to obtain and review another motion of the mussel dropper.

The fourth, fifth, sixth, and seventh pendulums are not considered due to symmetry of the model dropper.

Figure 7.9: The initial position of the model dropper for scenario A.

Figure 7.10: The initial position of the model dropper for scenario B.

Figure 7.11: The initial position of the model dropper for scenario C.

Circle Detection

In order to process the data obtained from the experiment a Matlab script is constructed. This script reads the video of the experiment and subdivides it into separate frames. The function *imfindcircles* is used to determine the positions of the nodes of the model dropper. This function detects circles and determines their radius and the x and y position of their centers in pixels. As input for the script a guess for the minimum and maximum radius of the circles must be given. The minimal radius is set at 8 pixels and the maximum radius is set at 15 pixels. That range was found to capture the circles that must be detected.

The function *imfindcircles* returns a vector containing 8 centers of the 8 circles, but is not consistent in returning the same center of the same circle. For example, in frame 1 node 3 is defined as the first index of the centers vector, but in frame 2 the center of node 5 is at the first index. Therefore, the script is adjusted to return the center of the circle that was closest to the center of the circle in the previous frame, to the same index.
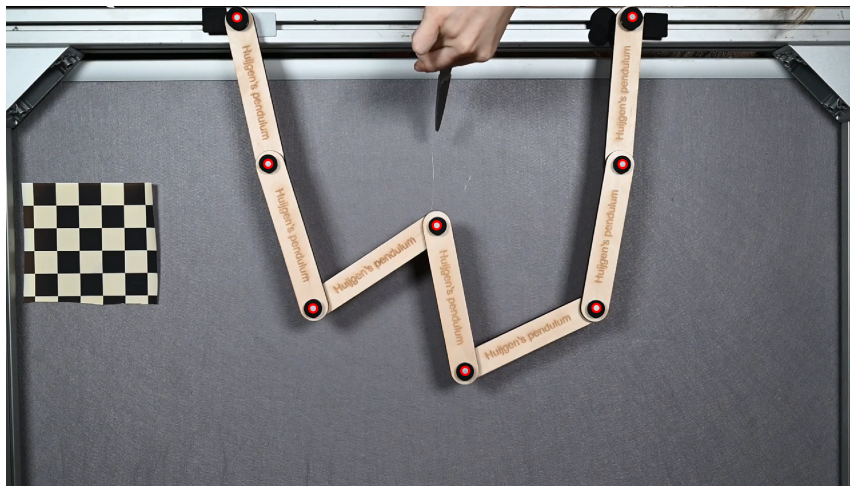
Figure 7.12: One frame from a video of scenario C. The third pendulum is attached to a point with a fishing line, bringing it in the desired initial position. The fishing line is cut which will induce the motion of the model dropper.

The resulting data is a set of 8 vectors containing the x and y position of each node at each frame. The calibration parameters of the camera are used to scale the positions from pixels to real-world coordinates. The next step is to calculate the angle each pendulum makes at each frame. To calculate the angles, the origin of the axis was replaced to the right lower corner so that all x and y positions were positive. The following equations , (7.1) to (7.4), were used to determine the angle for each pendulum at each frame. This is referable to the experiment of Punch et al. [23], who calculated the collision

angle of two colliding pendulums.

if $x_k > x_{k+1}$ & $y_k > y_{k+1}$:

$$\theta_k = -\arctan\left(\frac{y_k - y_{k+1}}{x_k - x_{k+1}}\right) \tag{7.1}$$

elseif $x_k < x_{k+1}$ & $y_k > y_{k+1}$:

$$\theta_k = -\left(\pi - \arctan\left(\frac{y_k - y_{k+1}}{x_{k+1} - x_k}\right)\right) \tag{7.2}$$

elseif $x_k < x_{k+1}$ & $y_k < y_{k+1}$:

$$\theta_k = \pi - \arctan\left(\frac{y_{k+1} - y_k}{x_{k+1} - x_k}\right) \tag{7.3}$$

elseif $x_k > x_{k+1}$ & $y_k < y_{k+1}$:

$$\theta_k = \arctan\left(\frac{y_{k+1} - y_k}{x_k - x_{k+1}}\right) \tag{7.4}$$
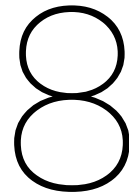
Results

The results obtained from the experiment and numerical model will be discussed in this chapter. First the experimental results are used to determine the linear and quadratic damping coefficient of the numerical model. This is done by reconstructing the experiment using the 2D model of the mussel dropper for various damping coefficients, which will be compared. Phase space plots of the simulation are presented in order to show the complex and nonlinear behaviour of the mussel dropper. Next, a simulation for a 3D mussel dropper in waves is conducted, for which the input and response will be analysed.

8.1. Experimental results

Each scenario was tested three times, with all three runs plotted on the same graph. This approach was taken to assess the success of the experiment and to determine the system's sensitivity to small variations in the initial position. Given the challenge of precisely replicating the initial position for each run, this method allowed for evaluation. All runs however seemed to be quite similar, as can be seen in the figures in appendix E. For Scenario C the third run had gone wrong and therefore only the results of two runs are presented.

To determine the right damping coefficient, the second pendulum of scenario A run 2 will be observed and compared with the results from the simulation of scenario A using the numerical 2D model. The 2D model is the same as the constructed 3D model, but the value of ϕ_n is always equal to zero. Ideally all scenarios would be observed and compared with numerical results but due to limited time only one scenario is considered. In this chapter, the results obtained from the experiment are referred to as the experimental results and the results obtained from the numerical model are referred to as the simulated results.

8.2. Determining the Damping Coefficients

In this section the linear and quadratic damping coefficients will be determined by reviewing the experimental result with the simulated results.

Initial Conditions for the Simulation
For the simulation of scenario performed by the numerical model, the right input must be determined. Since the experiment was done with physical pendulums and the model incorporates simple pendulums a translation from the physical pendulums to the simple pendulums must be made. The equivalent length and mass of each physical pendulum is calculated, see appendix D, and substituted in the model. The horizontal distance D_x was equal to 0.4 metres during the experiment. But, since as input the equivalent length is used, also the equivalent horizontal distance is calculated so that the angles the pendulums make are scaled correctly. The scalingfactor β (8.1) is calculated by dividing the total equivalent length of the mussel dropper by the actual length. Where L is the notation of the total length

and is equal to $L = 3\,L_A + 4\,L_B$. The length of one pendulum L_p was as determined in chapter 7.

$$\beta = \frac{3\,L_A + 4\,L_B}{7\,L_p} = 0.7 \tag{8.1}$$

An complete overview of the input for the numerical model in order to reconstruct scenario A is presented in table 8.1. In this table the parameters D_x, D_y, and D_z represent the distance between the first and last node of the dropper. The equivalent length and mass of pendulum A and B are described by m_A, m_B, L_A and L_B respectively. The total mass and length of the dropper are denoted by M and L. The maximum force that was exerted on the first pendulum of the simulated dropper is described by E_{max}. The number of pendulums is defined by the parameter N and is equal to the amount of pendulums used in the experiment. The parameter t_{end} denotes the duration of the simulation and dt is the time step applied during the simulation.

Initial conditions 3D Mussel Dropper		
D_x	0.28	$[m]$
D_y	0	$[m]$
D_z	0	$[m]$
m_A	0.0334	$[kg]$
m_B	0.0.0324	$[kg]$
M	0.2621	$[kg]$
L	0.7346	$[m]$
L_A	0.1061	$[m]$
L_B	0.1040	$[m]$
E_{max}	2.5624	$[N]$
N	7	$[-]$
t_{end}	65	$[s]$
dt	0.0065	$[s]$

Table 8.1: Input used for the 2D simulation to reconstruct the experiment of scenario A run 2.

In scenario A, the first pendulum of the dropper was lifted during the experiment and released from this initial position. To simulate scenario A the first pendulum of the simulated dropper must be lifted to the same height. This is done by adjusting the external force applied to the first pendulum until the initial angles of the simulation were comparable to the initial angles of the experiment, see table 8.2.

Initial angles for scenario A			
Angle	Experiment	Simulation	Unit
θ_1	-0.5128	-0.1501	$[rad]$
θ_2	-0.14518	-1.4440	$[rad]$
θ_3	-1.3616	-1.3513	$[rad]$
θ_4	-0.8410	-0.8642	$[rad]$
θ_5	1.1545	1.1560	$[rad]$
θ_6	1.3818	1.3943	$[rad]$
θ_7	1.4646	0.4607	$[rad]$

Table 8.2: A comparison of the initial angles of each pendulum for experiment scenario A run 2 and the 2D simulation.

The graph of the polar angle of the second pendulum over a period of time during the experiment for scenario A, the second run, is shown in figure 8.1. The plot is divided into three parts, presenting the behaviour of the model dropper at different time intervals. In the first part, the pendulum is released from an initial height and the motion is more complex and irregular. In the middle part, the motion transitions from irregular to a more periodic motion. Finally, in the last part, the motion is oscillatory and eventually dies out. The first part is considered the head of the graph and runs from 0 to 12 seconds. The middle part runs from 12 to 25 seconds and the last part, the tail, runs from 25 seconds to the end.

The simulation for scenario A is executed for when only linear damping is present and for when only quadratic damping is present. Various values for the coefficients are simulated. Each part of the graph is reviewed for the case with only linear damping and the case with only quadratic damping. By comparing the different values of the coefficients the best fit for linear damping is chosen for that part of the graph and the best fit for quadratic damping is chosen for that part of the graph. At the end, the potential damping factors are taken and a list of combinations will be constructed, see appendix E. The simulation will be run for these different combinations and the results will be compared with each other to find the best fitting combination of damping coefficients.
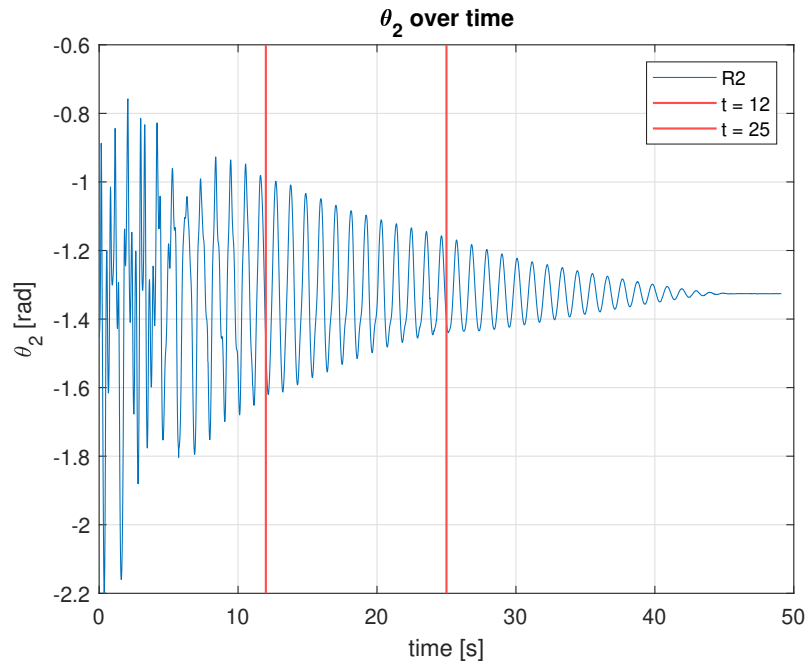
Figure 8.1: The angle of the second pendulum of the experiment of scenario A run 2 plotted over time. The graph is divided into 3 parts. The head part ranges from 0 to 12 seconds, the middle part from 12 to 25 seconds, and the tail part from 25 to 50 seconds.

8.2.1. Head of the Graph

The head of the graph shows the moment the pendulum is released from its initial state. This event causes large and more complicated motions in the dropper. The head of the graph is reviewed for various linear damping coefficients and various quadratic damping coefficients. The plot of the amplitude of the second pendulum over time and the response spectrum are provided and reviewed.

Linear Damping

In figure 8.2 the experimental result compared to the simulation for three different linear damping coefficients is presented. Small values for the damping coefficient were chosen since the no damping case already resulted in a too small amplitude. Reviewing the first three seconds the peaks and through of the experimental and simulated results are occurring at the same moments. However, all three simulations do not present the right height of the peaks and troughs. After about 5 seconds the amplitude of the experimental and simulated results are more comparable.
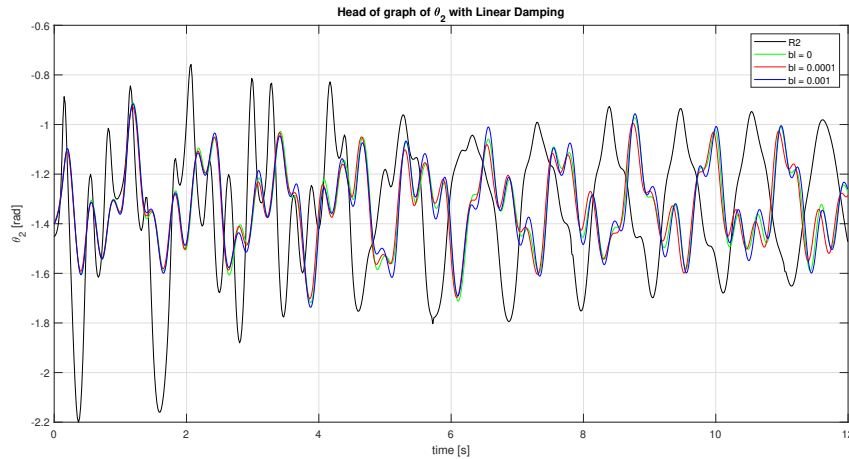
Figure 8.2: Graph considering the head of the plot with varying linear damping compared to the experimental result.

A fast Fourier transform is performed to obtain the amplitude response spectrum of the experimental and simulated results of the head of the graph, see figure 8.3. The level of energy within the experimental dropper and the simulated dropper should be similar, meaning that the peaks in the spectrum should have comparable sizes. Reviewing the spectrum, three peaks are noted. The first peak is underestimated by all three simulations. The second peak is comparable to the experimental result for all three simulations. The third peak in the spectrum is best estimated by the simulation with a damping coefficient of $b_{linear} = 0.0001$ kg/s. However, the simulated peaks are smaller than the peaks of the experimental results.

Figure 8.3: Spectrum considering the head of the plot with varying linear damping compared to the experimental result.

Comparing the results from the graph and the spectrum , the best fit for the linear damping coefficient is determined to be $b_{linear} = 0.0001$ kg/s, since the results for the three simulations in the graph are almost identical and because this value is the best estimation when reviewing the response spectrum.

Quadratic Damping
Now, the head of the graph is reviewed for three different quadratic damping terms. The quadratic damping terms have the same values as the earlier reviewed linear damping terms. Again, for the first three seconds the simulation has peaks occurring at the same moment as the experimental result, but the simulation underestimates the amplitude of the motion. Later on, the damping coefficient of 0 kg seems to maintain a larger amplitude than the results for the other damping coefficients.
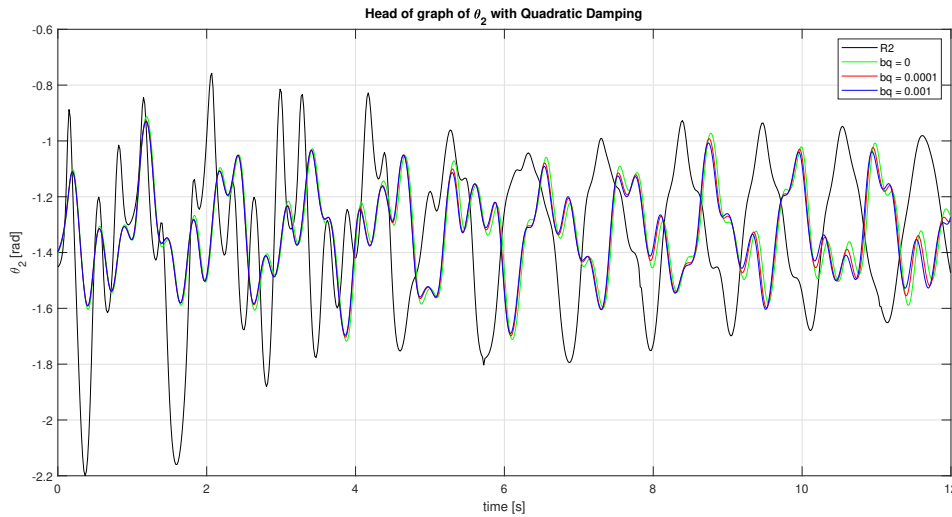
Figure 8.4: Graph considering the head of the plot with varying quadratic damping compared to the experimental result.

In the response spectrum, the results from the simulation are almost identical. Only at the last peak is a coefficient of $b_{quadratic} = 0.001$ kg a better fit than the other two coefficients, but the difference is small. Again, all peaks in the spectrum of the simulation are smaller than the peaks from the experimental result. Showing that the simulation underestimated the level of energy in the mussel dropper, which is related to the earlier identified underestimation of the amplitude by the simulated results.

Figure 8.5: Spectrum considering the head of the plot with varying quadratic damping compared to the experimental result.

Comparing the results from the graph and the spectrum , the best fit for the quadratic damping coefficient is determined to be $b_{quadratic} = 0$ kg, since the results for the three simulations in the simulation are almost identical and because this value is the best estimation when reviewing the graph.

8.2.2. Middle of the Graph

The middle of the graph shows the transition from a more chaotic motion to a periodic one. The plot from the experimental result transforms from one containing irregularities to a smooth curve. The middle of the graph is reviewed for different values of the linear and quadratic damping coefficients.

Linear Damping

Reviewing figure 8.6, the following observations are made. For a higher value of the damping coefficient, the irregularities in the curve decrease faster. However, the experimental result shows a smooth curve from the beginning of the graph while all three simulated results do not. The amplitude of the curve is overestimated by the smallest damping coefficient after 20 seconds and underestimated by the largest damping coefficient from the beginning of the graph.

Figure 8.6: Graph considering the middle part of the plot with varying linear damping compared to the experimental result.

The response spectrum of the experimental result shows two peaks, the spectrum of the simulated results show three peaks, see figure 8.7. This indicates that the level of damping is too low in the simulation, a higher damping would remove the third peak. However, the simulated results for the highest value of the damping coefficients dampens the first two peaks too much. The damping coefficient with a value of $b_{linear} = 0.002$ kg/s underestimates the first peak, but not as much as the results for $b_{linear} = 0.005$ kg/s. And, the results from $b_{linear} = 0.002$ kg/s overestimates the third peak, but not as much as $b_{linear} = 0.001$ kg/s.
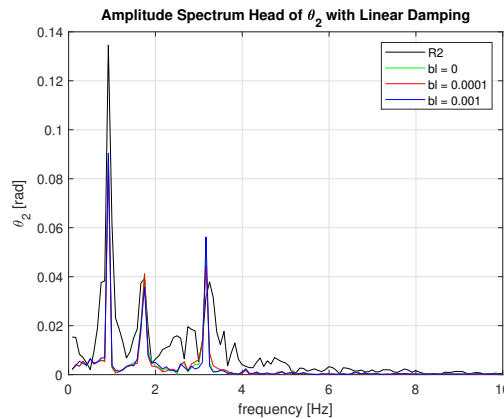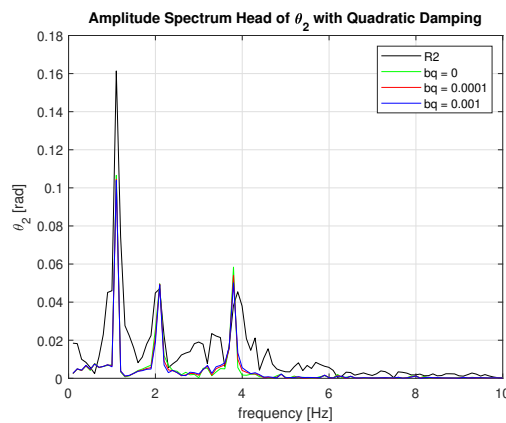

Figure 8.7: Spectrum considering the middle part of the plot with varying linear damping compared to the experimental result.

Comparing the results from the graph and the spectrum , the best fit for the linear damping coefficient is determined to be $b_{linear} = 0.002$ kg/s, since this is the best fit when reviewing the graph and is the best fit when reviewing all three peaks in the spectrum.

Quadratic Damping

Similar observations are made for the graph presenting the experimental result with the simulated results for three different values of the quadratic damping coefficients, see figure 8.8, as for the graph containing the linear damping coefficients 8.6. A higher value for the coefficient leads to less frequencies present in the motion and therefore comes closer to the experimental result. However, the highest coefficient underestimates the amplitude of the motion. The lowest coefficient is a good fit at the beginning of the graph but overestimates the motion after 17 seconds. The coefficient with a value of $b_{quadratic} = 0.01$ kg underestimates the amplitude at the beginning, is a better fit in the middle of the graph, but over amplifies the amplitude a bit at the end of the graph.
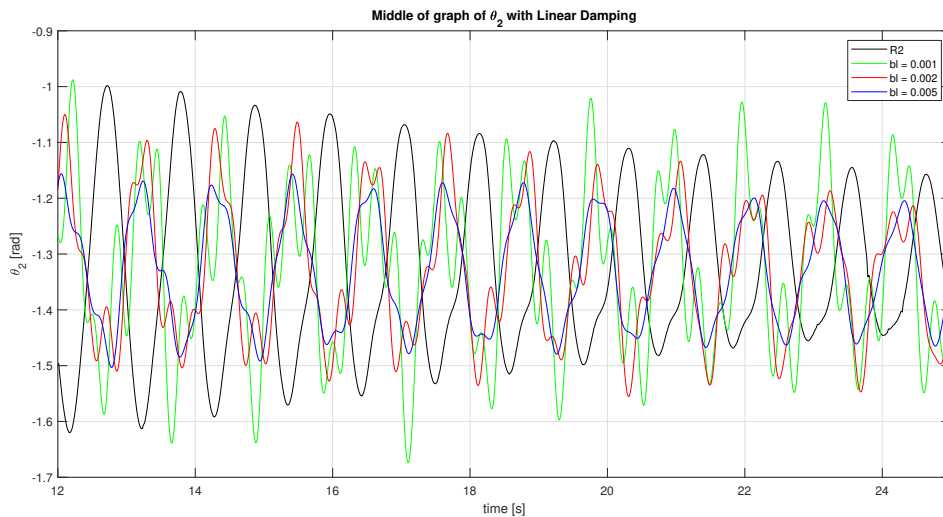

Figure 8.8: Graph considering the middle part of the plot with varying quadratic damping compared to the experimental result.

The spectrum of the graph containing the various quadratic damping coefficients compared to the experimental results 8.9 also allows for making similar observations as for the linear damping case. The spectrum of the simulations experience three peaks while the experimental spectrum provides only two. However, the width of the peaks of the simulation are comparable to the size of the peaks of the experimental results, which was not the case at the head of the graph. The lowest coefficient overestimates the last two peaks in the spectrum, the highest coefficient underestimates the first and second peak. The coefficient with a value of $b_{quadratic} = 0.01$ kg can be seen as the average between the lowest and highest coefficient reviewed.

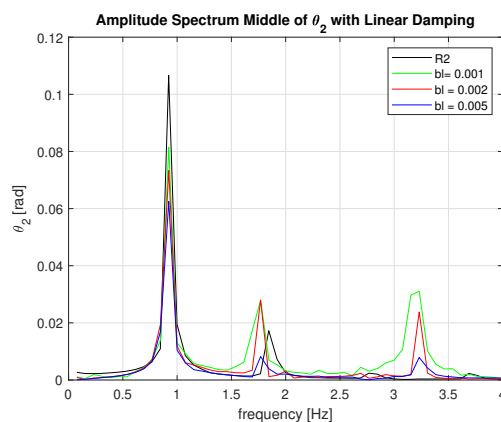**Figure 8.9:** Spectrum considering the middle part of the plot with varying quadratic damping compared to the experimental result.

Comparing the results from the graph and the spectrum , the best fit for the quadratic damping coefficient is determined to be $b_{quadratic} = 0.01$ kg, since this is the best fit when reviewing the graph and is the best fit when reviewing all three peaks in the spectrum.

8.2.3. Tail of the Graph

At the tail of the graph, the amplitude of the motion shows a relatively rapid decay until it has completely died out after about 45 seconds. The simulation with different values of the linear and quadratic damping coefficients are compared with the experimental result at the tail of the graph.

Linear Damping

When reviewing figure 8.10, one aspect of the graph is noteworthy. Namely, all the simulated results underestimate the amplitude too much at the beginning of the graph but don not show the same rapid decay. Therefore, only a large coefficient which already has a very small amplitude at the beginning of the graph, is the only one resulting in an amplitude equal to zero after 45 seconds.
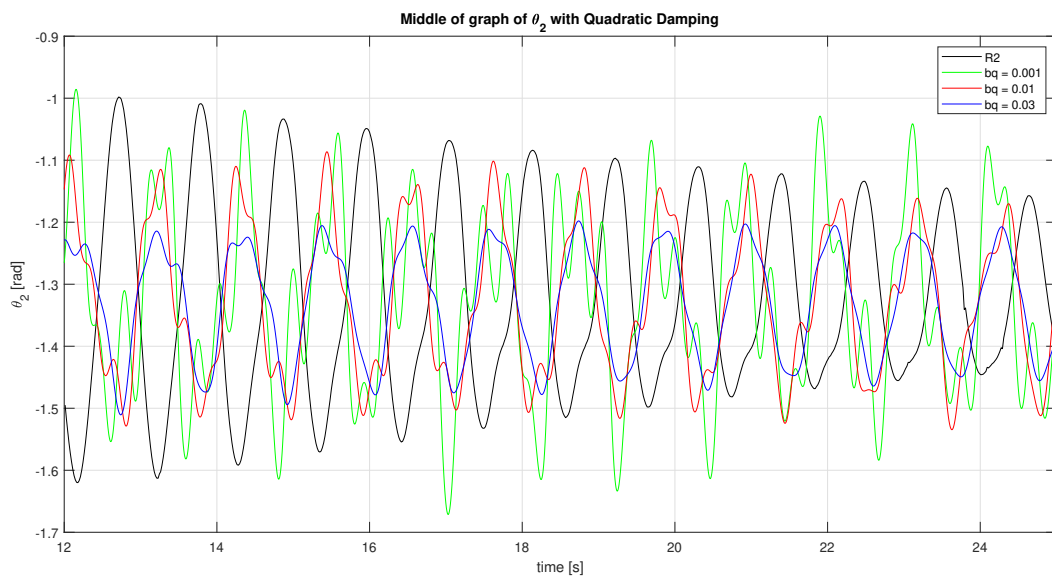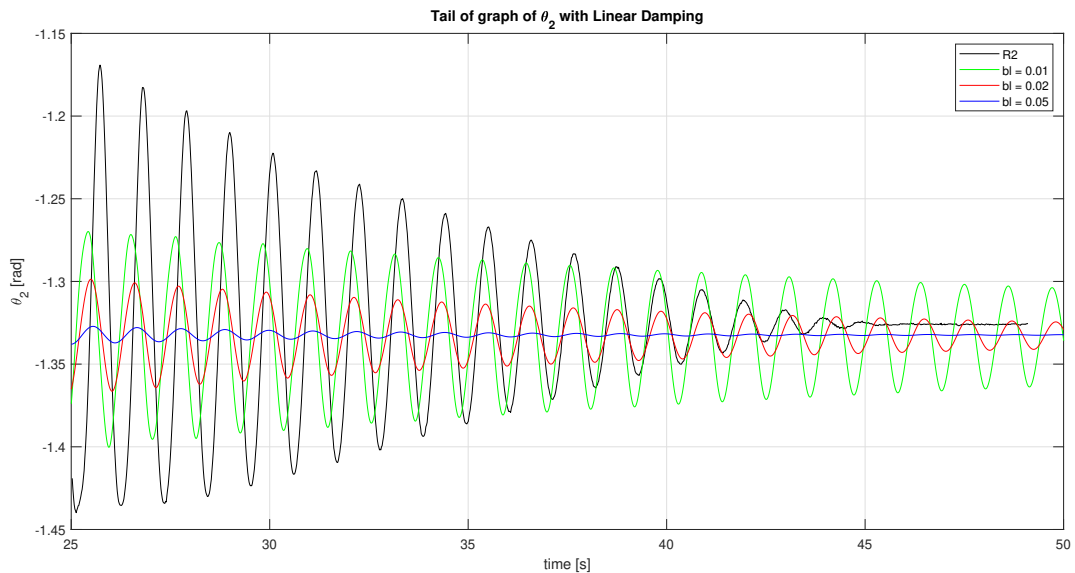

Figure 8.10: Graph considering the latter part of the plot with varying linear damping compared to the experimental result.

The response spectrum shows that the largest damping coefficient highly underestimates the energy in the system. Thus, even if this coefficient did dampen the motion enough to die out at the same time level as the experimental result, it is not a good fit. The lowest damping coefficient however comes closer to the level of energy in the experiment.

Figure 8.11: Spectrum considering the latter part of the plot with varying linear damping compared to the experimental result.

Comparing the results from the graph and the spectrum , the best fit for the linear damping coefficient is determined to be $b_{linear} = 0.01$ kg/s, since this is the best fit when reviewing the spectrum of the tail.

Quadratic Damping

From figure 8.12 it is observed that the results form the simulation do not show a significant decay, whereas the results shown in figure 8.10 did show a small decay. This indicates that quadratic damping is more at play when the velocity of the system is high and less for lower velocities. None of the simulated results are comparable to the experimental results when reviewing the amplitude of the motion. The all underestimate the motion at the beginning and do not decay fast enough to obtain an amplitude of zero after 45 seconds.

Figure 8.12: Graph considering the latter part of the plot with varying quadratic damping compared to the experimental result.

When reviewing the spectrum, see figure 8.13, the damping coefficient of $b_{quadratic} = 0.1$ kg is almost identical to the experimental result. This value rightly estimates the energy in the system, but considering the graph it can be seen that this is due to the fact that the simulated result is equal to the average amplitude of the experimental result.
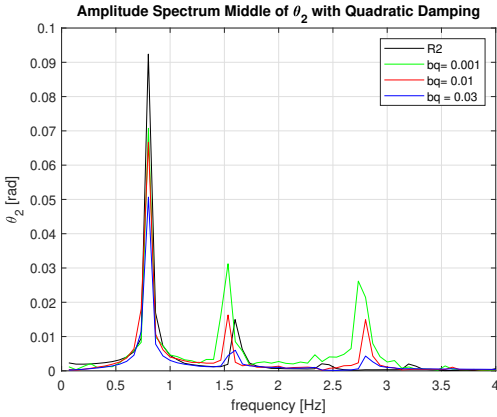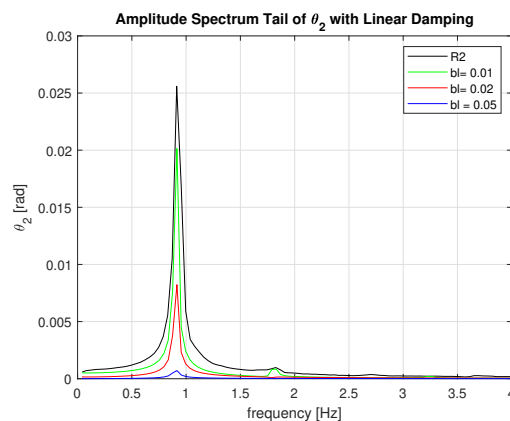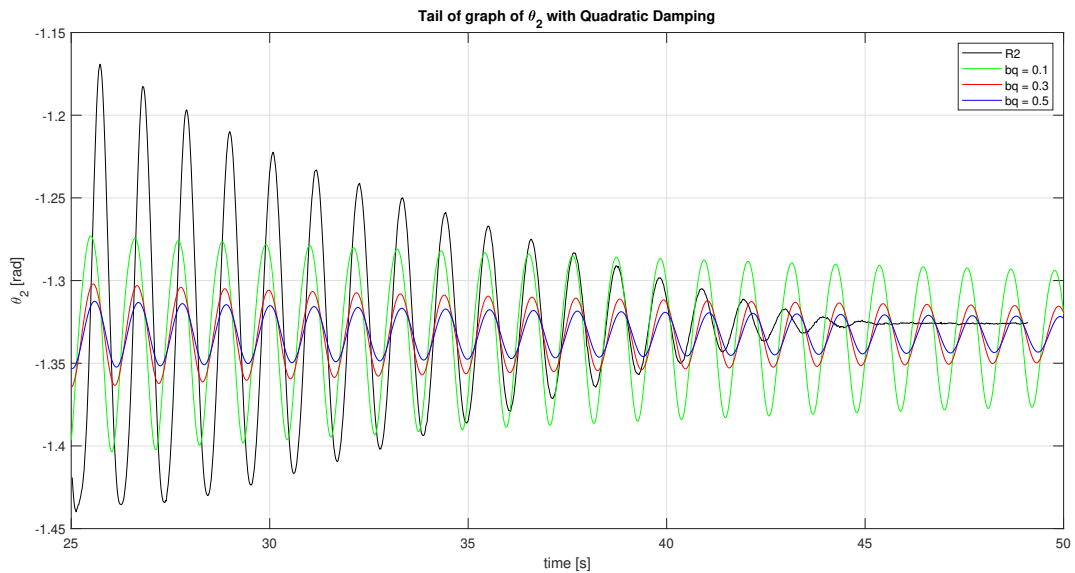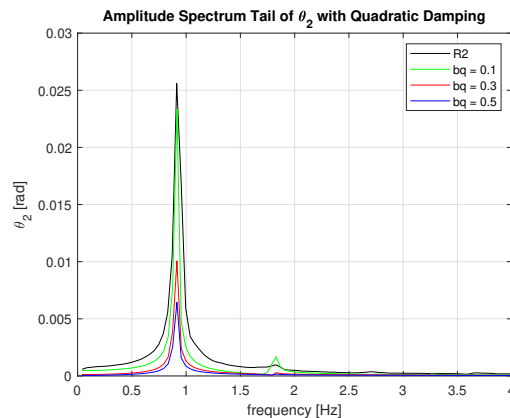

Figure 8.13: Spectrum considering the latter part of the plot with varying quadratic damping compared to the experimental result.

Comparing the results from the graph and the spectrum , the best fit for the quadratic damping coefficient is determined to be $b_{quadratic} = 0.1$ kg, since if the spectrum is considered, this value provides the best fit.

8.3. Combined Linear and Quadratic Damping

After reviewing the results from the run with only linear damping and the results from the run with only quadratic damping, multiple combinations are defined. The list of combinations that were tested can be found in appendix E. Two situations are considered, one where the damping coefficients are chosen when considering the best fits to finish the motion at almost the same time as the experimental result. This scenario is defined as the overdamped scenario. The other scenario considered is the underdamped scenario. Here the damping coefficients are chosen to best fit the head and middle part of the graph.

Considering the fact that quadratic damping is more relevant when the velocity is high and linear damping when the velocity is low, the expectation is that the quadratic damping coefficient for the head and middle of the graph and the linear coefficient for the tail of the graph are the best guesses for their respective dampings. The velocity of the mussel dropper shows oscillatory behaviour, due to the swinging motion of the dropper. This means that the velocity within the system changes constantly form high to low. However, still the velocity is expected to be higher right after the dropper is released from its initial position than when the motion has become periodic and almost close to zero.

8.3.1. Overdamped Scenario

To obtain a set of combinations that result in a decay of the amplitude of the motion comparable to the experimental result, a multiple combinations were simulated. The combinations were constructed using the results from the head, middle and tail of the graph as described in the sections before. Three combinations were found to best fit the experimental result with as goal to let the motion die out at a similar rate as for the experimental result. The three best combinations were:

Combination 1	$b_{linear} = 0.010$	$[kg/s]$	$b_{quadratic} = 0.000$	$[kg]$
Combination 2	$b_{linear} = 0.010$	$[kg/s]$	$b_{quadratic} = 0.001$	$[kg]$
Combination 3	$b_{linear} = 0.010$	$[kg/s]$	$b_{quadratic} = 0.030$	$[kg]$

Table 8.3: An overview of the combinations of linear and quadratic damping terms that proved to come closest to the experimental result by comparing the three parts of the graph for various coefficients.

The final combination of damping coefficients is again determined by reviewing the three parts of the plot of the experiment and finding the best fit.

Head of the graph

For the head of the plot in figure 8.14, it can be seen that all combinations result in an overdamped motion throughout the graph. The amplitude of the motion of all three simulated results are similar. The largest difference between the simulated combinations is that combination 3 results in a more smooth curve after a period of time, which is similar to the behaviour of the curve of the experimental result. Thus, a higher quadratic damping seems to result in a less irregular curve. Considering the spectrum as shown in figure 8.15, no large differences are observed between the three simulations. The second combination comes closest to the experimental result, but not sufficiently. Since the three combinations generated similar results, the third combination is considered to be the best fit since this combination shows a smoothed curve after a period of time.

Figure 8.14: Graph considering the first part of the plot for the 3 combinations compared to the experimental result.
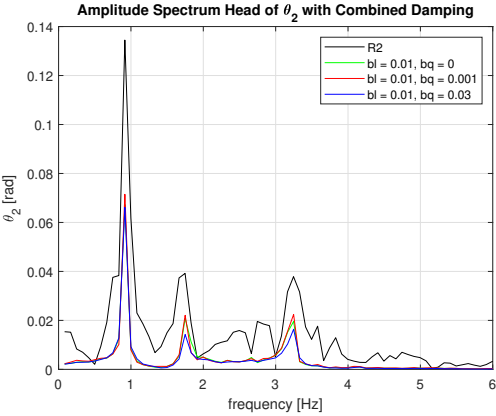
Figure 8.15: Spectrum considering the first part of the plot for the 3 combinations compared to the experimental result.

Middle of the graph

Reviewing the middle of the graph, see figure 8.16, it is noticed that again no large differences between the simulated results are present. All three combinations underestimate the amplitude of the motion and now all three show a smooth curve. The second combination shows a slight decay when looking at the beginning and the end of the graph, the other combinations experience less of a decay. This decay is similar to the behaviour of experimental model, as can be seen in the graph. The response spectrum, as shown in figure 8.17, again shows no large deviations between the simulated results. The second combination comes closest to the experimental result. Therefore, considering the graph and spectrum, the second combination is determined to be the best fit for the middle of the graph.
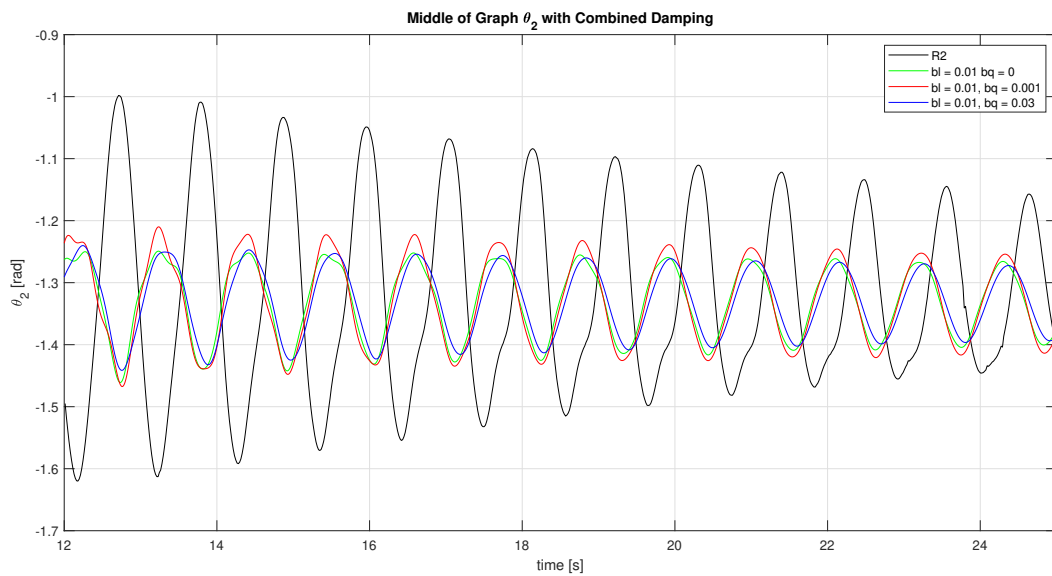
Figure 8.16: Graph considering the middle part of the plot for the 3 combinations compared to the experimental result.
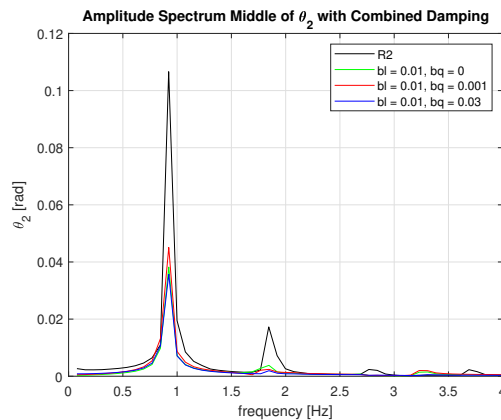
Figure 8.17: spectrum considering the middle part of the plot for the 3 combinations compared to the experimental result.

Tail of the graph

Considering the tail of the graph, which can be found in figure 8.18, it can be seen that the amplitude of the motion of the simulated combinations are similar. Again, the second combination experiences the most decay, however the decay is slight. The second combination is the best fit considering the response spectrum, see figure 8.19. A higher quadratic damping coefficient has as effect more overall damping. Reviewing both the graph and the spectrum the second combination is again determined to be the best fit. This because the graphs of all three combinations are similar, but the second combination is a closer fit when looking at the spectrum and shows more similar behaviour to the experimental result than the other combinations.
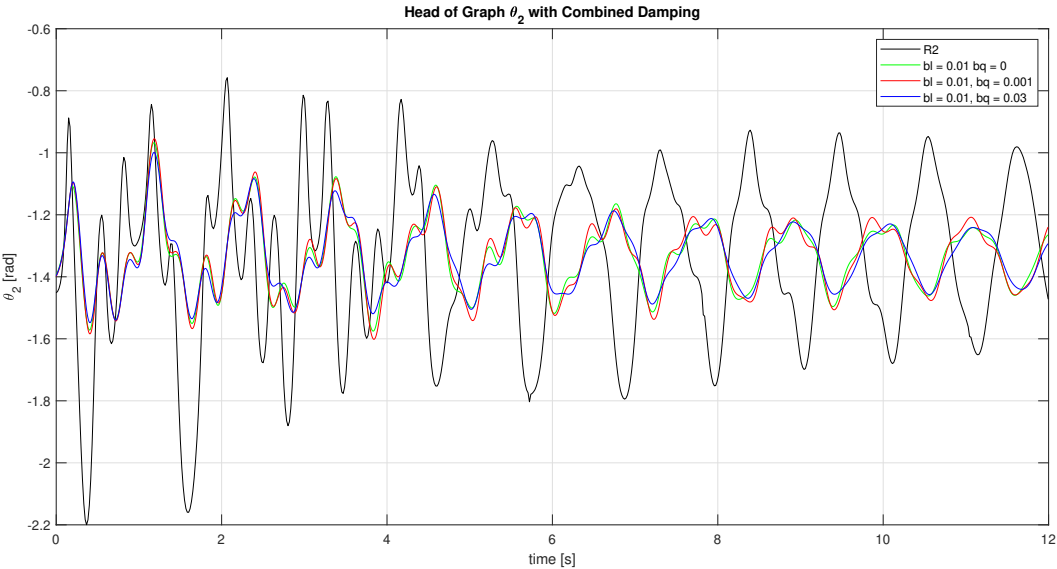

Figure 8.18: Graph considering the last part of the plot for the 3 combinations compared to the experimental result.
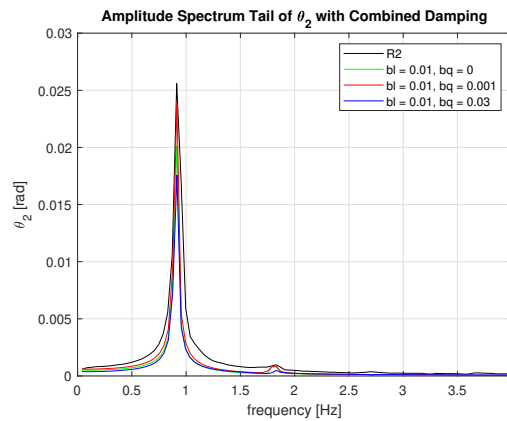
Figure 8.19: Spectrum considering the last part of the plot for the 3 combinations compared to the experimental result.

In all scenarios the system ends underdamped, see figure 8.18. There was no scenario found where the decay of the amplitude started later in the simulation. Therefore, for determining the right coefficient the spectrum is considered, see figure 8.19. In this figure it can be seen that scenario 2 again best represents the experimental results.

Best fit overdamped scenario
Combination 2 is considered to be the best fit with the experimental results.

$$b_{linear} = 0.010 \ [kg/s] \tag{8.2}$$

$$b_{quadratic} = 0.001 \ [kg] \tag{8.3}$$

In figure 8.20 the results of the simulation with combination 2 are plotted against the experimental result for each pendulum in the dropper. The overall shape of the curves are comparable to each other. However, the amplitude of the motion obtained from the simulation is smaller than the experimental results. The irregularities in the curves are removed at about the same time. A noticeable difference is that the motion for the simulated dropper does not dampen completely after 45 seconds.

Even though this combination of coefficients provided the best overall fit, from an engineering perspective it is not a suitable fit. The amplitude of the simulation is overdamped at each second. When a mussel farm is engineered to be located at an offshore location, or any other location, the mussel droppers must be engineered to withstand extreme conditions. Therefore, it is more desired to have a model that underestimates the damping, and thereby introducing an extra safety factor to the design.
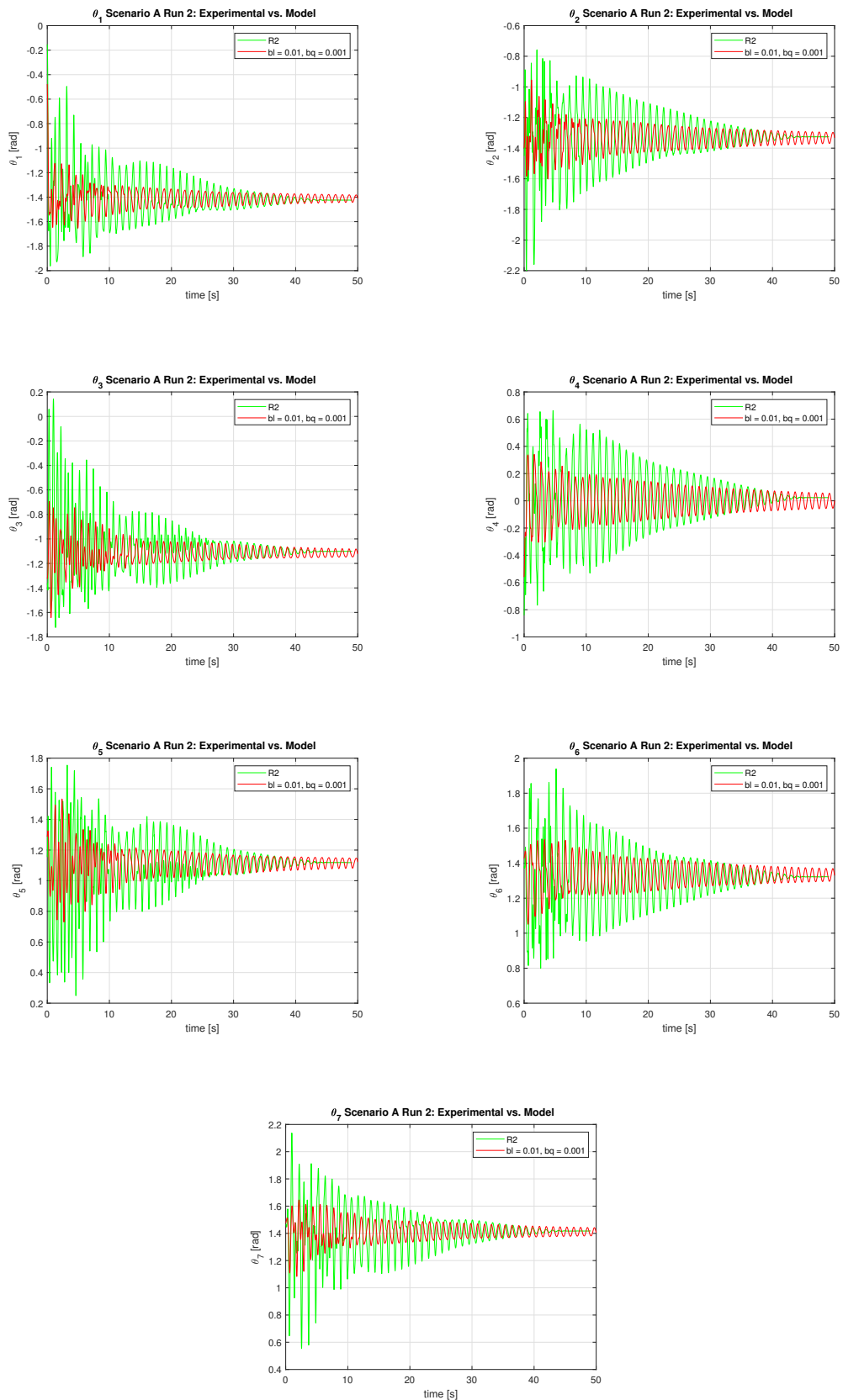
Figure 8.20: A plot for each angle of the mussel dropper over time for the experimental result of scenario A, run 2, and the 2D simulation with damping coefficients $b_l = 0.01$ and $b_q = 0.001$.

8.3.2. Underdamped Scenario

The scenario where the best fit was aimed to be found for the head and middle of the graph is reviewed in this section. The same method as for the overdamped scenario is applied. Multiple combinations were reviewed an the best combinations found are shown in table 8.4.

Combination 1	$b_{linear} = 0.001$	$[kg/s]$	$b_{quadratic} = 0.001$	$[kg]$
Combination 2	$b_{linear} = 0.002$	$[kg/s]$	$b_{quadratic} = 0.001$	$[kg]$
Combination 3	$b_{linear} = 0.001$	$[kg/s]$	$b_{quadratic} = 0.002$	$[kg]$

Table 8.4: An overview of the combinations of linear and quadratic damping terms that are close to the experimental result at the beginning and middle of the graph by comparing the three parts of the graph for various coefficients. Further referred to as the underdamped combinations since these combinations do not dampen the motion enough at the end.

Head of the graph

The three simulated results do not show large differences when considering the amplitude of the motion, see figure 8.21. After six seconds it is noticed that the first combination maintains a higher amplitude than the other combinations. Reviewing the spectrum 8.22 again no large differences between the simulations are spotted, as all three overestimate the energy within the system. Therefore, the best fit is chosen to be the first combination, since the amplitude of this result remains closest to the experimental one.
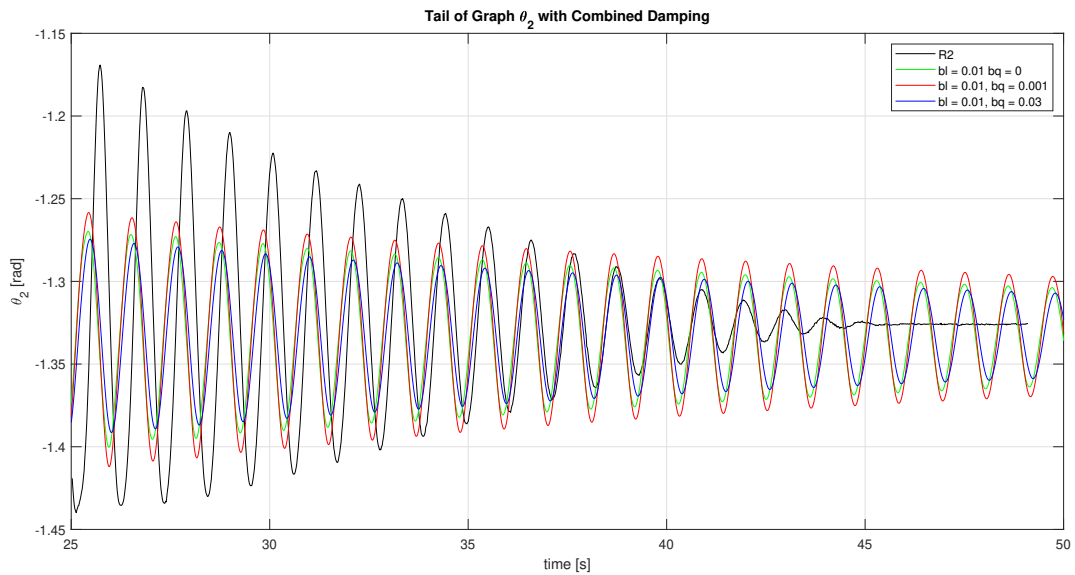

Figure 8.21: Graph considering the head of the plot for the 3 underdamped combinations compared to the experimental result.

Figure 8.22: Spectrum considering the head of the plot for the 3 underdamped combinations compared to the experimental result.

Middle of the graph

In the middle of the graph, the first combination overestimates the amplitude of the motion, the second combination also overestimates the amplitude of the motion after 20 seconds, but less than the first combination, as can be seen in figure 8.23. The third combination underestimates the amplitude from the beginning till 23 seconds and thereafter becomes a close fit to the experimental result. So, the combination with two smaller values for the coefficients provides not enough damping for the middle part. The combination with a larger linear damping is the best fit when looking at the overall curve. The combination with a larger quadratic damping provides a bit too much damping. The spectrum 8.24 shows almost identical results for the three combinations. The second combination is considered to be the best fit as this combination underestimates the amplitude of the motion less in the middle of the graph than the third combination, but also does not largely overestimate it, as does the first combination.
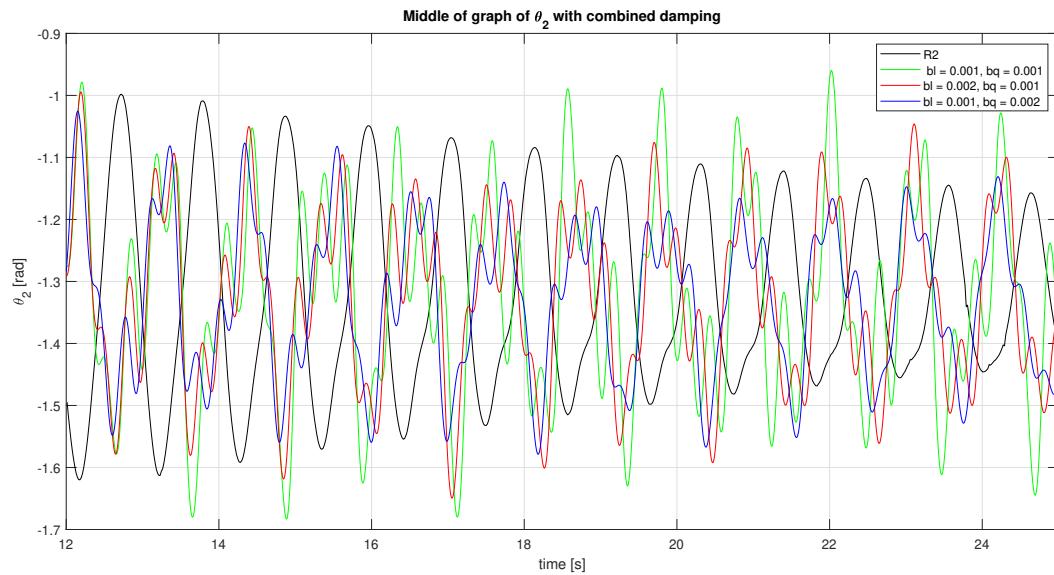
Figure 8.23: Graph considering the middle part of the plot for the 3 underdamped combinations compared to the experimental result.
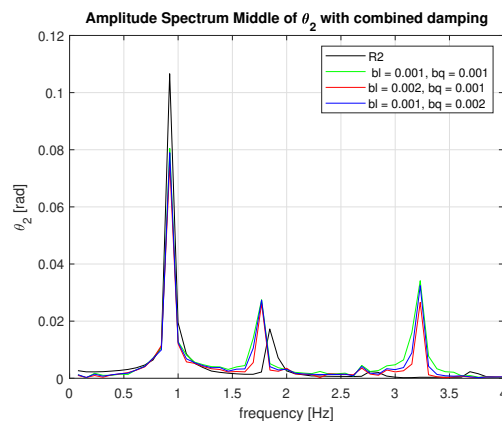
Figure 8.24: Spectrum considering the middle part of the plot for the 3 underdamped combinations compared to the experimental result.

Tail of the graph

Since for all three combinations the applied linear damping coefficient is small, the motion does not decay fast enough to come close to the experimental result, as is shown in figure 8.25. After a close review of the graph, it is noticed that the simulation with the second combination of damping coefficients results in the smallest amplitude. Also for the spectrum, see figure 8.26 is combination 2 determined to be the best fit. All three combinations overestimate the level of energy in the system, but combination 2 does this the least.
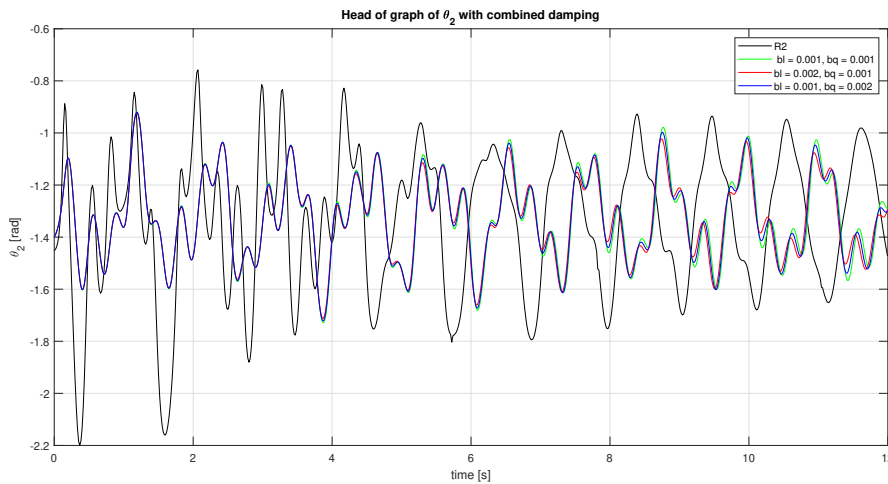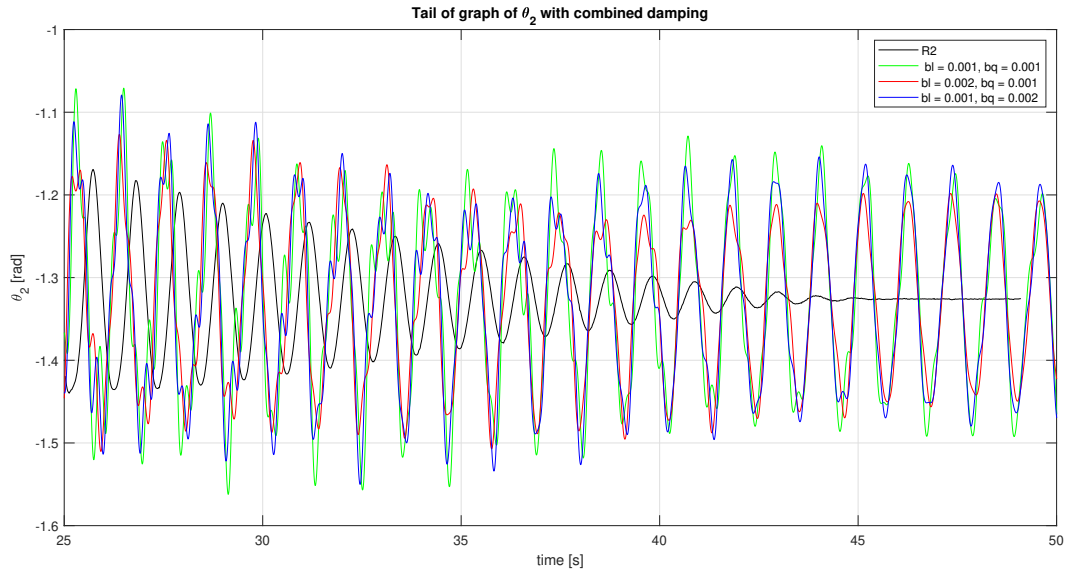

Figure 8.25: Graph considering the tail of the plot for the 3 underdamped combinations compared to the experimental result.

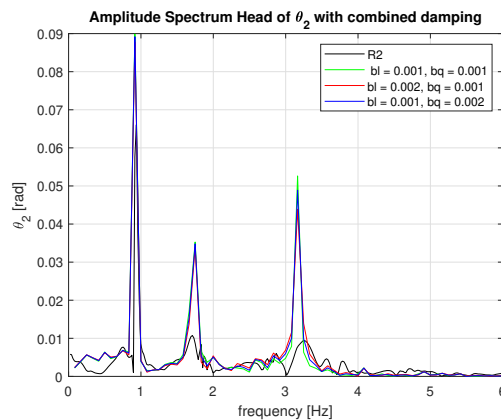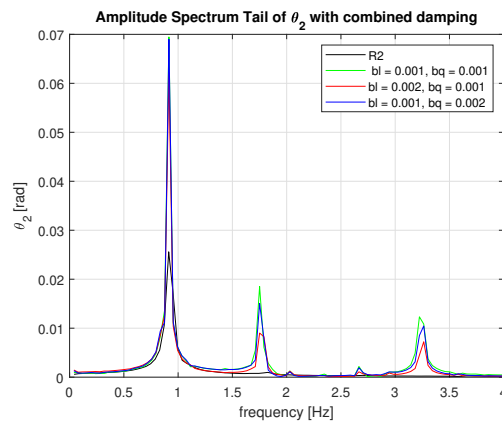**Figure 8.26:** Spectrum considering the tail of the plot for the 3 underdamped combinations compared to the experimental result.

Best fit underdamped scenario

The second combination is determined to be the overall best fit since this combination provided the best fit for the middle and the tail of the graph.

$$b_{linear} = 0.002 \ [kg/s] \tag{8.4}$$

$$b_{quadratic} = 0.001 \ [kg] \tag{8.5}$$

These new values for the damping coefficients are applied to the numerical model scenario A is again simulated. The results for each pendulum of the simulation compared to the experimental results are presented in figure 8.27. At the beginning the simulated motion still experiences too much damping, but it now comes closer to the experimental result that for the coefficients determined in the previous section. Also, for the middle part of the graph the simulation now seems to come close to the experimental result. The largest deviation is at the end of the graph where the motion is not dampened enough. However, it is more important that the large amplitudes of the mussel dropper are simulated than small motions. This enables the possibility to simulate reliable results for example a high wave force that is applied to the model. Therefore, the damping coefficients as determined for the underdamped scenario are determined to be the final damping coefficients which will be applied to the numerical model.
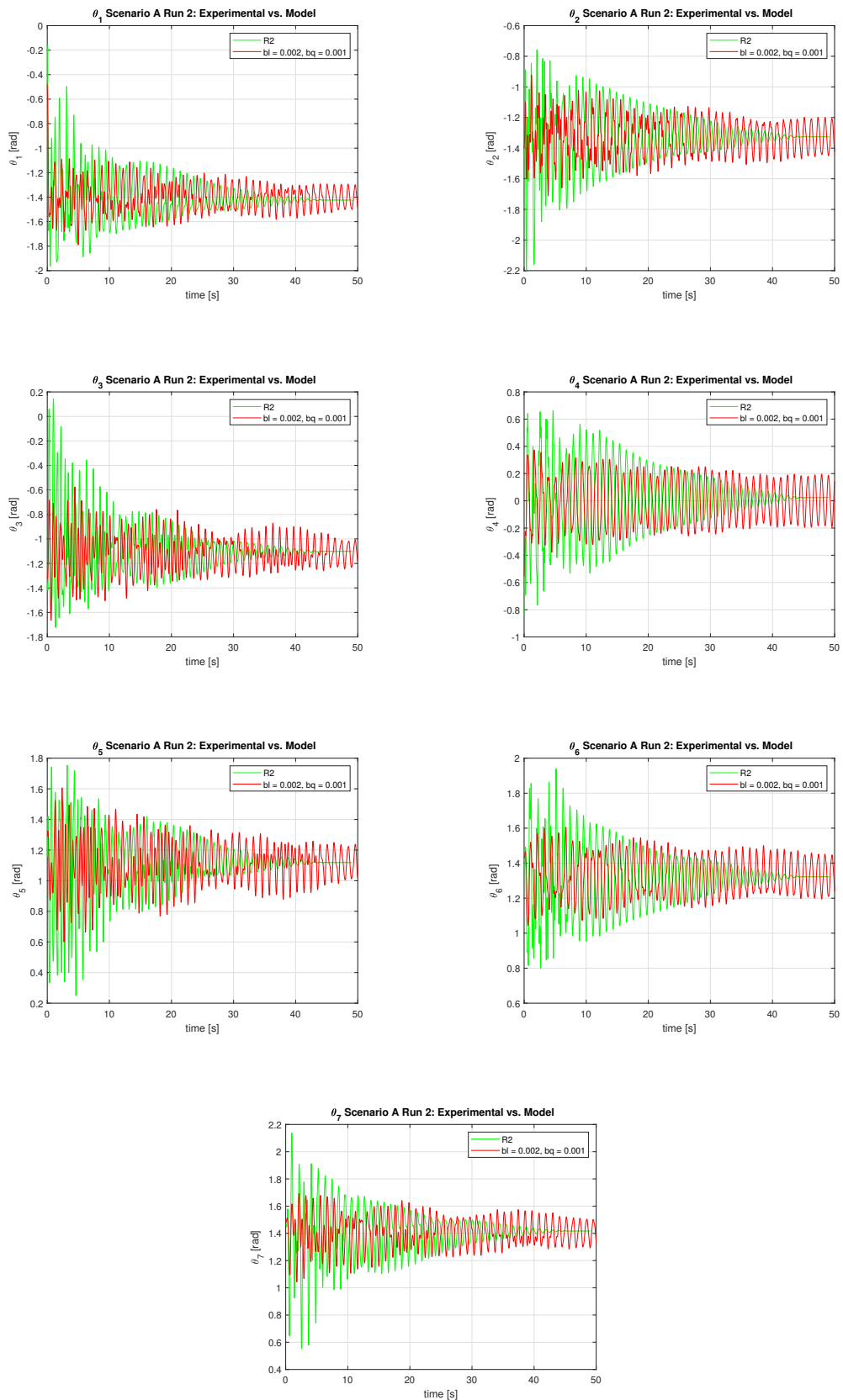
Figure 8.27: A plot for each angle of the mussel dropper over time for the experimental result of scenario A, run 2, and the 2D simulation with damping coefficients $b_l = 0.002$ kg/s and $b_q = 0.001$ kg.

8.4. Phase Space for Scenario A

The simulation of scenario A, the 2D simulation, is used to make phase space plots of the pendulums. A complete overview of the plots can be found appendix E. In appendix F the phase space plots of a 3D simulation can also be found, which showed similar behaviour to the 2D case.

Since up till now the second pendulum is reviewed, the phase space plots of the second pendulum are presented. In figure 8.28 the phase space of the second pendulum is shown for the case of no damping. In figure 8.29 the phase space of the second pendulum with the determined linear and quadratic damping coefficients is shown. Reviewing both plots, complex and irregular trajectories can be seen. This indicates nonlinear behaviour of the system. When comparing the phase space plots to the phase spaces of the double pendulum 3.5 and 3.6, it is noticed that the phase space of the dropper is somewhere between the fully periodic motion and the fully chaotic motion of the double pendulum. Irregular and complex trajectories are observed in the plots for the simulated scenario, but also a pattern is detected, especially for the case of no damping. In the scenario with damping, the trajectory in the phase space plot decreases, which means that energy is leaving the system. This is expected behaviour of the pendulum, as described in chapter 3.
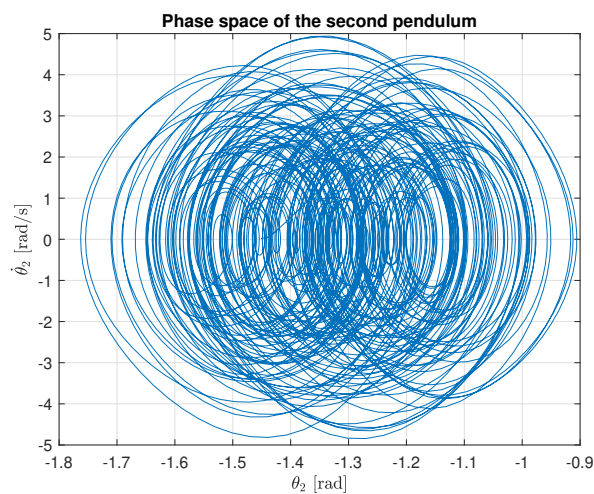
Figure 8.28: A phase space plot of the second pendulum in the 2D simulation of scenario A without damping. Showing the nonlinear and complex behaviour of the pendulum.
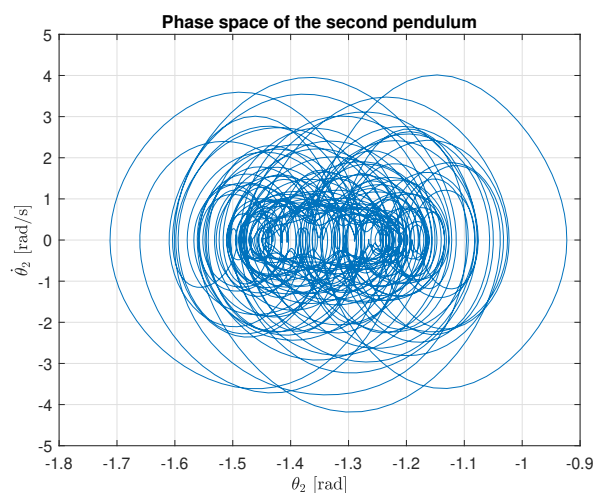
Figure 8.29: A phase space plot of the second pendulum in the 2D simulation of scenario A with $b_l = 0.002$ kg/s and $b_q = 0.001$ kg. Showing the nonlinear and complex behaviour of the pendulum while energy is leaving the system.

8.5. Numerical 3D results

The 3D model was constructed with in mind to simulate a mussel dropper in waves. As described in chapter 1, the Cees Leenaars will be placed in the North Sea, therefore a sea state from the North Sea is taken and applied to the mussel dropper. The sea state applied has a significant wave height of $H_s = 8.20$ m and a peak wave period of $T_p = 11.7$ s. This sea state occurs statistically once in every 25 years. It is desired that the mussel droppers of the Cees Leenaars will survive these conditions. The total wave elevation is calculated by using equation (6.2). In total, 190 wave components are considered. The characteristics of the wave components can be found in appendix G.
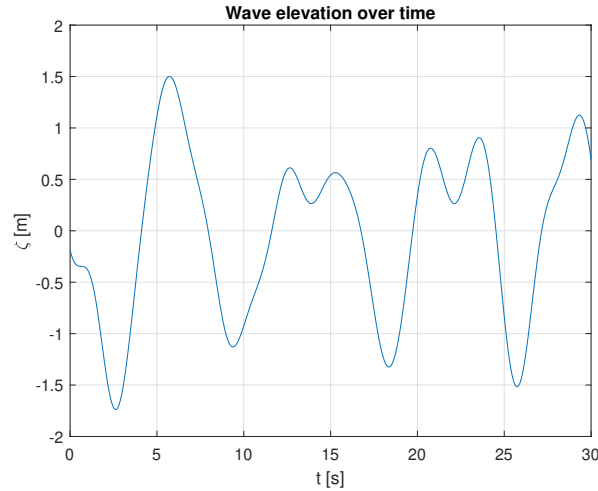
Figure 8.30: The wave elevation $\zeta(t)$, consisting of multiple wave components, plotted over time. This sea state occurs every 25 years and must be survived by the mussel dropper.

To model the mussel dropper in the given sea sate, dimensions and model specifics as shown in table 8.5 are used. The total mass of the dropper is equal to 14 kg/m. The water depth is set at 30 m, which is a typical water depth for the North Sea. The wave is propagating in positive y-direction and the position at which the wave is reviewed is at the origin of the system $(0, 0, 0)$.

Initial model parameters			Initial wave parameters		
L	17	$[m]$	h	30	$[m]$
M	238	$[kg]$	ρ_f	1000	$[kg/m^3]$
D_x	2.5	$[m]$	D_{cyl}	0.05	$[m]$
D_y	0	$[m]$	μ	$\pi/2$	$[rad]$
D_z	0	$[m]$	C_d	2	$[-]$
t_{end}	30	$[s]$	C_m	1	$[-]$
dt	0.03	$[s]$	x_w	0	$[m]$
N	18	$[-]$	y_w	0	$[m]$
b_{linear}	0.002	$[kg/s]$	z_w	0	$[m]$

Table 8.5: Initial conditions of the reference model for a single spherical pendulum.

8.5.1. Response of the Mussel Dropper

In figure 8.31, a snapshot of the simulation of the mussel dropper is found after 4 seconds into the simulation. From figure 8.30 it can be seen that the wave amplitude starts to increase at that moment, which complies with the large displacement that can be seen in figure 8.31.
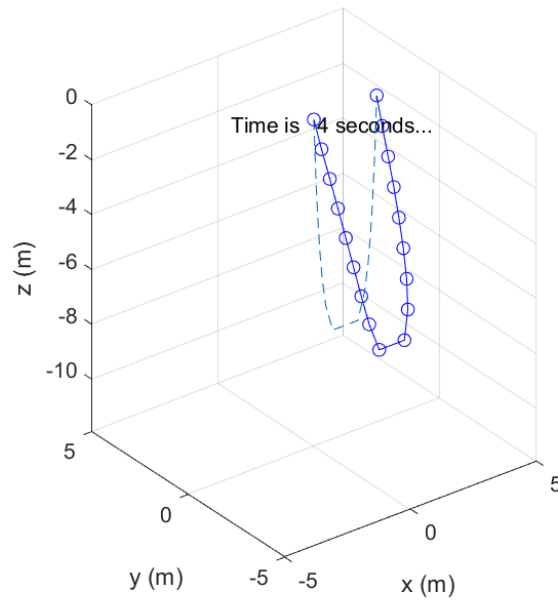
Figure 8.31: A snapshot for the simulation of the 3D mussel dropper in waves with the input as provided in table 8.5. The snapshot is made after 4 seconds. The wave is propagating in the positive y-direction.

To review the response of the mussel dropper, the tenth pendulum is discussed. The results for each pendulum of the simulated dropper can be found in appendix G. In figure 8.32 the polar and azimuth angle of the tenth pendulum are plotted over the simulated time. Comparing figure 8.30 and 8.32 show that when the amplitude of the wave is most positive, the tenth pendulum was removed furthest from it's resting position. The troughs in the plot for the polar angle are almost at the same location as the peaks for the azimuth angle of the pendulum. Furthermore, it can be seen that the plot of the wave elevation deviates from the plot of the tenth pendulum. So, the input is not the same as the output. This is due to the nonlinear characteristic of the mussel dropper.
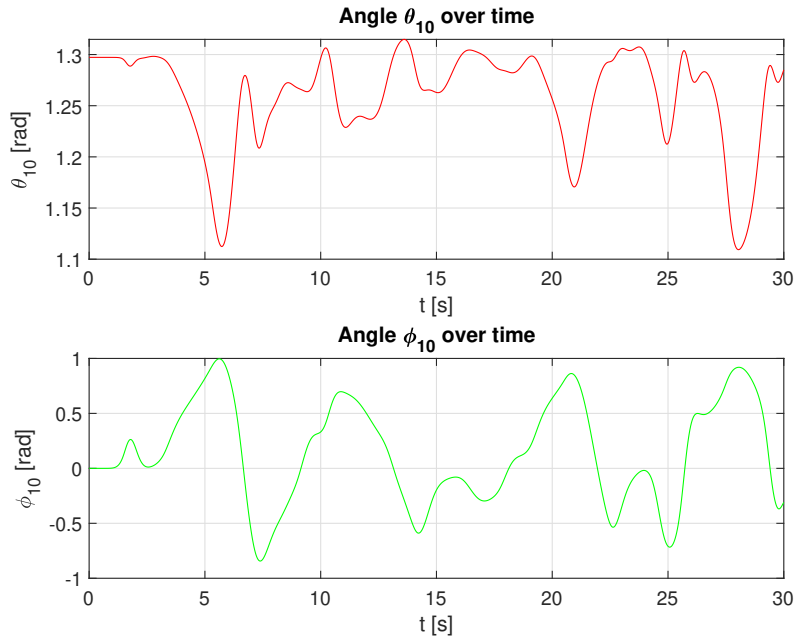
Figure 8.32: A plot of the polar angle (top figure) and the azimuth angle (bottom figure) of the first pendulum in the 3D mussel dropper over the simulated period of time.

To provide an extra representation of the nonlinear behaviour of the system, the response spectrum for the tenth pendulum is provided in figure 8.33. In the right figure 8.33b, the initial peak in the spectrum is removed so to better show the rest of the spectrum. Both spectra show irregular peaks and thus indicate the nonlinear behaviour of the system.
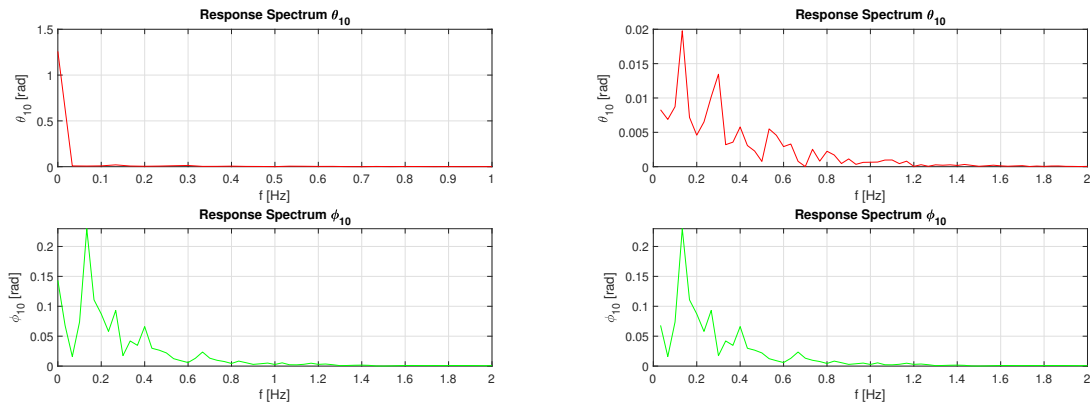
(a) The response spectrum of the polar and azimuth angle of the tenth pendulum.

(b) The response spectrum of the polar and azimuth angle of the tenth pendulum, with the initial peak excluded from the spectrum.

Figure 8.33

To make a representation of the chaos present in the system, a phase space plot for the polar and azimuth angle of the tenth pendulum are made in figure 8.34. The complex and chaotic behaviour as described in chapter 3 can also be found in the mussel dropper. The phase space plots show an irregular pattern with trajectories that loop or spiral. This indicates nonlinear and chaotic behaviour. The mussel dropper experiences internal damping but also damping due to the viscosity of the water surrounding the dropper, damping causes the amplitude of the motion to decrease. On the other hand, the wave force excites the system, causing the amplitude of the motion to increase. The increasing

and decreasing amplitudes of the trajectory in the phase space plots are a representation of this energy being added or leaving the system.

Figure 8.34: A phase space plot of the polar angle (top figure) and the azimuth angle (bottom figure) of the first pendulum in the 3D mussel dropper over the simulated period of time.

9

Conclusion

Offshore mussel cultivation results in high loads on the mussel farm. High loads on the farm can lead to failures such as mussel fall-off and line entangl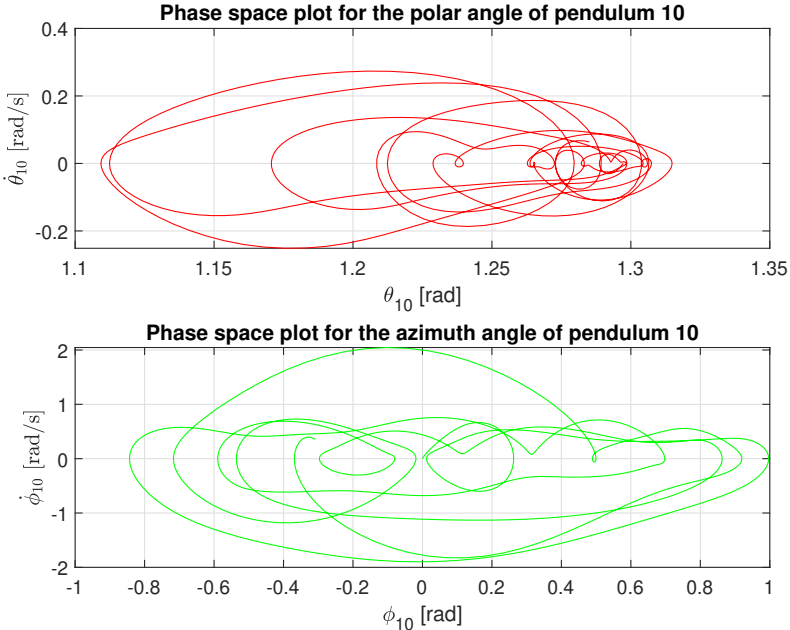ement. An accurate model to estimate the effects of these loads on a mussel farm does not yet exist without the simplification of a mussel dropper as cylinder. If the dynamic behaviour of a mussel farm is known, events such as mussel fall-of and line entanglement can be predicted. The motion of the mussel droppers also influences the flow in and around the farm. The flow within a mussel farm determines the amount of nutrition's reaching the mussels and therefore mussel growth. The dynamic behaviour of a single mussel dropper in the farm therefore has a significant influence on the performance of the mussel farm. This led to the following objective for this thesis:

"The construction of a 3D numerical model of the dynamic response of a single looped mussel dropper in waves."

For the construction of the numerical 3D model of a mussel dropper in waves, first a simple pendulum was considered. The model for the simple pendulum was expanded to a model for a double pendulum, which was again expanded to model a string of pendulums. Finally, constraints were added to the model of a string of pendulum to convert the model into a model for a mussel dropper.

Analytical
During the construction of the models, various analytical and numerical methods were applied. For a simple 3D pendulum, the Euler-Lagrange equation was applied to derive the equations of motion. This method was applied because it was deemed to be the easiest one applicable. By applying the Lagrangian method, the number of equations of motion was reduced from three equations in x,y and z direction, to two equations of motion. One for each generalised coordinate, which where the polar and azimuth angle. Another advantage of the Lagrangian method is that the method is based on the energy within the system, and vectors do not have to be delt with. This meant that defining the positive and negative direction of the motion were less important and there are less chances to have an error in the signs in the equations of motion. Furthermore, by using the Lagrangian method, it was not necessary to determine the tension within the pendulum. The Lagrangian method could also be applied by using x,y, and z as generalised coordinates. However, by applying the angles as generalised coordinates, the constraints were already taken into account and no need for Lagrange multipliers was needed.

For the double pendulum, again the Lagrangian method was applied because of the same advantages as discussed before. Four equations of motion were needed to describe the behaviour of a double pendulum, one for the polar angle of each pendulum and one for the azimuth angel of each pendulum. The expression for the Lagrangian became larger because not only the energy of the first and second pendulum were taken into account, but also the effect of the coupling of the pendulums. Deriving the equations of motion therefore became a harder task and trigonometric identities were used to simplify the equations.

To model the string of pendulums, first the Lagrangian method was used, by rewriting the equa-

tions for the double pendulum in matrix form. Each pendulum that was connected to the system enlarged the matrix equation. Since the coupling effects between two pendulums were known by deriving the equations for the double pendulum, these coupling effects were copied for each pendulum attached to the system. However, later on it proved to be easier to use the Newtonian method than the Lagrangian method when the model for the dropper had to be constructed. Since for modelling the dropper, constraints had to be set to the position of the last pendulum. Setting constraints to the x,y, and z position for the last pendulum was easier done when the equations of motion where expressed in Cartesian coordinates. First, the Lagrangian method was applied but now instead of using the angles as generalised coordinates, the x,y and z coordinates were used. However, this meant that Lagrange multiplier had to be used to apply constraints to the system. Each pendulum had to have its own constraint for the length and three constraints for the position where needed. Since this would lead to an expression with many Lagrange multipliers Newton's method was used instead, where only one constraint for the equation of motion in each direction of the last pendulum was needed.

Furthermore, the Lagrangian method can better be applied to conservative instead of non-conservative systems. Non-conservative forces such as dissipative forces and externally applied forces can be substituted in the Euler-Lagrange equation by using the Dissipation function and generalised forces. However, the Lagrangian method is based on the principle of least action and non-conservative forces can't come from this principle. Therefore, d'Alembert's principle was used for adding dissipative and external forces. Using the Newtonian method, forces are applied easily. Therefore, the Newtonian method was better suited for the model of the mussel dropper, since the mussel dropper would experience dissipative and other external forces.

Finally using Newton's second law to derive the equations of motion led to three equations of motion per pendulum. The acceleration, velocity and position of each pendulum was expressed in spherical coordinates. The signs now became important, if a sign was determined wrong in the equation the model would not work.

Numerical

For the simple and double 3D pendulum, after reviewing explicit, implicit and semi-implicit Euler, a semi-implicit integration scheme was found to be best applicable. Applying semi-implicit Euler proved to be less work than implicit Euler, and more stable than explicit Euler. Explicit Euler seemed to amplify the amplitude of the motion, whereas implicit Euler damped the amplitude of the motion. The semi-implicit method combines explicit and implicit Euler and therefore this method cancels out the over and under damping effects of these methods. When dissipative and external forces were applied to the system, the model became less stable and a smaller time step was necessary to maintain stability.

The semi-implicit integration scheme required the calculation of an expression for the second derivative of the angles. This was done by rewriting the matrix equation and isolate the vector containing the second derivatives of the generalised coordinates. However, the model had troubles with the determinant of the mass matrix M, which is non-diagonal and non-symmetric. The determinant sometimes came close to zero or to infinity, causing the matrix to become singular. Also, the equation of motion for the azimuth angle contained a term with a division by $sin(\theta)$. This meant that when theta was zero, the value for the second derivative of the azimuth angle would become infinite, also causing the matrix to become singular.

The semi-implicit model for the double pendulum worked, but experienced issues when damping and a driving force were introduced. Altering the initial conditions and time step could sometimes avoid these issues, but the model was not unconditionally stable. Therefore, implicit Euler was used to further construct the numerical model for the string of pendulums. The implicit model was unconditional stable but required more analytical and computational effort. The implicit integration scheme results in a set of nonlinear equations that must be solved at each time step. A nonlinear solver was needed to solve the set of equations, the Newton-Raphson method was applied. Instead of using the build-in Matlab function "fsolve" the nonlinear solver was constructed from scratch. Therefore, the Jacobian that must be constructed for the Newton-Raphson method is determined analytically whilst fsolve determines the Jacobian matrix discretely. Determining the Jacobian analytically proved to be more robust. It was also found that determining the Jacobian for the equations derived using the Newtonian method was easier than for the Lagrangian method. The expressions on the matrix elements became smaller, and therefore the computational time was reduced.

For constructing the model of the dropper the equations for the boundary conditions were incorporated into the nonlinear solver. There was still one complication and that was that the implicit method

introduced a lot of numerical damping. The amount of numerical damping resulted in a non-realistic response of the mussel dropper. To reduce the amount of numerical damping the Crank-Nicolson method was applied. A γ of 0.5 would be the best value to not over or under damp the motion. However, this value for γ proved to be too unstable, therefore a value of 0.51 was chosen, which provided the model with enough stability.

Damping
The results from the experiment were compared with results from simulations made by the numerical model for various values of the linear and quadratic damping coefficient. The first set of damping coefficients found to be the best fit underestimated the amplitude of the motion when compared to the experimental result. This could be due to a translation error from a physical or compound pendulum to a simple pendulum. Another reason could be that the internal damping in the system is too simplified. Coupling terms of the damping were not taken into account, but these could play an important part for this highly nonlinear system.

Since from an engineering perspective it is safer in the designing phase to overestimate the motion of the mussel dropper than to underestimate the motion. Therefore, the process of finding the right damping coefficients was repeated. Now the focus was to obtain similar results for the experimental and simulated dropper at the moment right after the dropper was released from its initial state. The damping coefficients for the numerical model wre deterimend to be $b_{linear} = 0.002 \; \frac{kg}{s}$ and $b_{quadratic} = 0.001 \; kg$.

As to conclude, the main objective of this thesis is reached. A numerical model for a 3D mussel dropper in waves is constructed and an indication of the internal damping of the model is provided.

10

Recommendations

A numerical model for a 3D mussel dropper is constructed, however there is still much that can be researched or improved. Recommendations for further potential research are discussed in this chapter.

Experiment

My recommendations concerning validating the 2D model is to conduct a more accurate experiment. The experiment that was conducted can be improved. Due to the limited time on this research, the experiment was kept as simple as possible, but therefore possibly lacked in accuracy. The stickers with circles that were detected by Matlab were not completely fixed and could've changed position during the tests. Also, the surface on which the stickers were applied was spherical, a flat surface would provide a better surface to put the circles on. Another improvement of the experiment is that the cutting of the fishing line could be improved. At times during the experiment, the fishing line got stuck between two pendulums after it was cut and therefore could have had an impact on their motion. In the future, a more complex experiment could be conducted using for example accelero- and/or potentiometers to accurately measure the angular position and acceleration of the pendulums. This could lead to more accurate results and therefore help in a better determination of the damping.

Furthermore, it is recommended to do experiments with a simple pendulum instead of a physical pendulum. Even though the equivalent length, equivalent mass and the mass moment of inertia of the physical pendulums were determined, it would be better to conduct experiments with masses attached to massless strings.This would avoid possible errors in the input required for the reconstruction of the experiment with the numerical model.

Lastly, a 3D model is constructed but not yet validated. A recommendation would be to validate the 3D model also by conducting an experiment, preferably in waves. An experiment in waves also provides information on the drag and inertia coefficients and takes into account effects like added mass.

Model

There are improvements that can be made to the numerical mode. There is still some numerical damping present in the model. The model can be improved by reducing this numerical damping while maintaining stability.

In the 3D model, the coordinates at which the wave was observed were set to zero. However, a more accurate response can be obtained if the coordinates at which the wave were observed would be equal to the coordinates of each pendulum. Because this would yield into a complicated expression for the general Jacobian, the wave coordinates were fixed. In further research the model could be improved by taking into account variable wave coordinates. Another improvement could be to consider loads due to current in the model, giving a better representation of reality.

Furthermore, there were two main problems that were sometimes encountered in the numerical model. The first one is that the nonlinear solver at times did not converge to a solution. The second problem was that the Jacobian became singular during some simulations. Both problems were avoided by changing the time step or initial conditions, but it would be better to not encounter them at all. For further research it would be recommended to find ways to reduce numerical instabilities and make the model more robust.

References

[1] Yong Bai, R. Bhattacharyya, and M.E. McCormick. "Pipelines and Risers". In: *Elsevier Ocean Engineering Series* 3 (2001), pp. 85–95.

[2] Josh Bevivino. *The Path From the Simple Pendulum to Chaos*. 2009.

[3] R W Bos and P R Wellens. "Fluid-structure interaction between a pendulum and monochromatic waves". In: *Journal of Fluids and Structures* 100 (2021), p. 103191. DOI: `10.4121/13187594`. URL: `www.elsevier.com/locate/jfs`.

[4] Llucia Mascorda Cabre et al. "Offshore longline mussel farms: a review of oceanographic and ecological interactions to inform future research needs, policy and management". In: *Reviews in Aquaculture* 13.4 (2021), pp. 1864–1887. DOI: `10.1111/raq.12549`.

[5] "Loads and Responses". In: *Handbook of Offshore Engineering*. Ed. by Subrata K Chakrabarti. Offshore Structure Analysis Inc., Plainfield, IL, USA, 2005. Chap. 4, pp. 133–195. ISBN: 978-0-08-044381-2.

[6] A.K. Chopra. "Dynamics of structures: Theory and application to earthquake engineering". In: (1995).

[7] Rod Cross. "Rotational modes of a double conical pendulum". In: *European Journal of Physics* 44 (2 Mar. 2023). ISSN: 13616404. DOI: `10.1088/1361-6404/acacd6`.

[8] Duc Long Dao et al. *Physics Education Experimental evaluation of damping models for a nonlinear pendulum system You may also like Towards more accurate numerical modeling of impedance based high frequency harmonic vibration Residual gas damping noise in constrained volume in space-borne gravitational wave detection Parameter identification of general damping model based on structural dynamic response Experimental evaluation of damping models for a nonlinear pendulum system*. 2023.

[9] Peter Dourmashkin. "8.6: Drag Froces in Fluids". In: *MIT OpenCourseWave*. Massachusetts Institute of Technology, 2022.

[10] *Euler's numerical method*. https://www.uah.edu/images/people/faculty/howellkb/DEText-Ch9.pdf.

[11] Marc Gagnon and Pierre Bergeron. "Observations of the loading and motion of a submerged mussel longline at an open ocean site". In: *Aquaculture Engineering* 78 (2017), pp. 114–129. DOI: `10.1016/j.aquaeng.2017.05.004`.

[12] Yuji Harata and Takashi Ikeda. "Modal analysis for localization of harmonic oscillations in nonlinear pendulum arrays subjected to horizontal excitation". In: *International Journal of Non-Linear Mechanics* 157 (Dec. 2023). ISSN: 00207462. DOI: `10.1016/j.ijnonlinmec.2023.104555`.

[13] OOS International. https://www.oosinternational.com/ssmf-oos-cees-leenaars/. 2023.

[14] Sven Erik Jørgensen and Brian D. Fath. *Encyclopedia of Ecology*. Elsevier B.V., 2008. ISBN: 978-0-08-045405-4.

[15] Pauline Kamermans. "Case study: Mussels in the North Sea". In: *CERES* (2020).

[16] Kun Woo Kim, Jae Wook Lee, and Wan Suk Yoo. "The motion and deformation rate of a flexible hose connected to a mother ship". In: *Journal of Mechanical Science and Technology* 26 (3 Mar. 2012), pp. 703–710. ISSN: 1738494X. DOI: `10.1007/s12206-011-1202-5`.

[17] Alexander Knysh et al. "Numerical modeling of submerged mussel longlines with protective sleeves". In: *Aquacultural Engineering* 88 (Feb. 2020). ISSN: 01448609. DOI: `10.1016/j.aquaeng.2019.102027`.

[18] Jannis Landmann et al. "Drag and inertia coefficients of live and surrogate shellfish dropper lines under steady and oscillatory flow". In: *Ocean Engineering* 235 (Sept. 2021). ISSN: 00298018. DOI: `10.1016/j.oceaneng.2021.109377`.

[19] "Finite Difference Method". In: *Multiphysics in Porous Materials*. Ed. by Zhen (Leo) Liu. Springer International Publishing AG, 2018. Chap. 28, pp. 369–382. ISBN: 978-3-319-93027-5. URL: `https://doi.org/10.1007/978-3-319-93028-2`.

[20] David Morin. *The Lagrangian Method*. Harvard, 2007.

[21] Fearghal O'Donncha, Scott C James, and Emanuele Ragnoli. "Modelling study of the effects of suspended aquaculture installations on tidal stream generation in Cobscook Bay". In: *Renewable Energy* 102 (2016), pp. 65–76. DOI: `10.1016/j.renene.2016.10.024`.

[22] David Russell Plew. *The Hydrodynamic Effects of Long-line Mussel Farms*. 2005.

[23] Oscar Punch et al. "A comparison of pendulum experiments and discrete-element simulations of oblique collisions of wet spheres". In: *AIChE Journal* 69 (3 Mar. 2023). ISSN: 15475905. DOI: `10.1002/aic.17989`.

[24] W. Raman-Nair and B. Colbourne. "Dynamics of a mussel longline system". In: *Aquacultural Engineering* 27 (3 2003), pp. 191–212. ISSN: 01448609. DOI: `10.1016/S0144-8609(02)00083-3`.

[25] W. Raman-Nair et al. "Numerical model of a mussel longline system: Coupled dynamics". In: *Ocean Engineering* 35 (13 Sept. 2008), pp. 1372–1380. ISSN: 00298018. DOI: `10.1016/j.oceaneng.2008.05.008`.

[26] Wageningen University & Research. *Carrying Capacity for Shellfish*. Year of Access. URL: `https://www.wur.nl/en/research-results/research-institutes/marine-research/themes/carrying-capacity-for-shellfish.htm`.

[27] Dan Russel. *Oscillation of a Simple Pendulum*. Accessed on 14-07-2023. 2018. URL: `https://www.acs.psu.edu/drussell/Demos/Pendulum/Pendulum.html`.

[28] Rebeka Sarkar, Krishna Kumar, and Sugata Pratik Khastgir. *Motion of a parametrically driven damped coplanar double pendulum*. 2023.

[29] Ravichandran Sowmya, Manoharan Premkumar, and Pradeep Jangir. "Newton-Raphson-based optimizer: A new population-based metaheuristic algorithm for continuous optimization problems". In: *Engineering Applications of Artificial Intelligence* 128 (Feb. 2024). ISSN: 09521976. DOI: `10.1016/j.engappai.2023.107532`.

[30] C L Stevens et al. "Hydrodynamic Forcing of Long-Line Mussel Farms: Observations". In: *Journal of Waterway* 133 (3 2007), pp. 192–199. DOI: `10.1061/ASCE0733-950X2007133:3192`.

[31] Craig Stevens et al. "The physics of open-water shellfish aquaculture". In: *Aquacultural Engineering* 38 (3 June 2008), pp. 145–160. ISSN: 01448609. DOI: `10.1016/j.aquaeng.2008.01.006`.

[32] T. Strohmeier et al. "Temporal and spatial variation in food availability and meat ratio in a longline mussel farm (Mytilus edulis)". In: *Aquaculture* 276 (1-4 Apr. 2008), pp. 83–90. ISSN: 00448486. DOI: `10.1016/j.aquaculture.2008.01.043`.

[33] A.H. Techet. "Morrison's Equation". In: (2004).

[34] R.R. van Zanten. "Analysis of elastoplastic response of maritime structures in breaking waves using a double pendulum with a friction hinge". In: *TU Delft Repository* (2020).

[35] Dan Zhao et al. "Offshore wind turbine aerodynamics modelling and measurements". In: *Wind Turbines and Aerodynamics Energy Harvesters*. Elsevier, 2019, pp. 373–400. DOI: `10.1016/b978-0-12-817135-6.00005-3`.
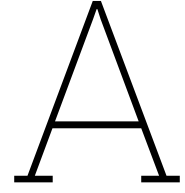
Double Pendulum

In this appendix the calculations conducted to construct the numerical model of the double pendulum are presented. Furthermore, the numerical scheme used for the model is shown.

A.1. The Lagrangian Method for a Double Pendulum

A.1.1. Coordinates

The position of the two pendulum bobs are described by these expressions.

$$x_1 = L_1 \, sin(\theta_1) \, cos(\phi_1) \tag{A.1}$$

$$y_1 = L_1 \, sin(\theta_1) \, sin(\phi_1) \tag{A.2}$$

$$z_1 = -L_1 \, cos(\theta_1) \tag{A.3}$$

$$x_2 = L_1 \, sin(\theta_1) \, cos(\phi_1) + L_2 \, sin(\theta_2) \, cos(\phi_2) \tag{A.4}$$

$$y_2 = L_1 \, sin(\theta_1) \, sin(\phi_1) + L_2 \, sin(\theta_2) \, sin(\phi_2) \tag{A.5}$$

$$z_2 = -L_1 \, cos(\theta_1) - L_2 \, cos(\theta_2) \tag{A.6}$$

A.1.2. Kinetic Energy

The position coordinates of the pendulum bobs are used to determine the velocity of the bobs and therefore their kinetic energy.

$$T_1 = \frac{1}{2} \, m_1 \, v_1^2 = \frac{1}{2} \, m_1 \, (\dot{x}_1^2 + \dot{y}_1^2 + \dot{z}_1^2) \tag{A.7}$$

$$\dot{x}_1 = L_1 \dot{\theta}_1 \, cos(\theta_1)cos(\phi_1) - L_1 \dot{\phi}_1 \, sin(\theta_1)sin(\phi_1) \tag{A.8}$$

$$\dot{y}_1 = L_1 \dot{\theta}_1 \, cos(\theta_1)sin(\phi_1) + L_1 \dot{\phi}_1 \, sin(\theta_1)cos(\phi_1) \tag{A.9}$$

$$\dot{z}_1 = L_1 \dot{\theta}_1 \, sin(\theta_1) \tag{A.10}$$

Substituting the equations (A.8), (A.9), and (A.10) into the equation for the kinetic energy(A.7) and thereafter simplifying the final kinetic energy is found (A.11)

$$T_1 = \frac{1}{2} \, m_1 \, (L_1^2 \, \dot{\theta}_1^2 + L_1^2 \, \dot{\phi}_1^2 \, sin^2(\theta_1)) \tag{A.11}$$

For the second pendulum the kinetic energy can be calculated by using equations(A.12), (A.13), (A.14), and (A.15).

$$T_2 = \frac{1}{2} \, m_2 \, v_2^2 = \frac{1}{2} \, m_2 \, (\dot{x}_2^2 + \dot{y}_2^2 + \dot{z}_2^2) \tag{A.12}$$

$$\dot{x}_2 = L_1\dot{\theta}_1 \, cos(\theta_1)cos(\phi_1) - L_1\dot{\phi}_1 \, sin(\theta_1)sin(\phi_1) + L_2\dot{\theta}_2 \, cos(\theta_2)cos(\phi_2) - L_2\dot{\phi}_2 \, sin(\theta_2)sin(\phi_2) \quad \text{(A.13)}$$

$$\dot{y}_2 = L_1\dot{\theta}_1 \, cos(\theta_1)sin(\phi_1) + L_1\dot{\phi}_1 \, sin(\theta_1)cos(\phi_1) + L_2\dot{\theta}_2 \, cos(\theta_2)sin(\phi_2) + L_2\dot{\phi}_2 \, sin(\theta_2)cos(\phi_2) \quad \text{(A.14)}$$

$$\dot{z}_2 = L_1\dot{\theta}_1 \, sin(\theta_1) + L_2\dot{\theta}_2 \, sin(\theta_2) \quad \text{(A.15)}$$

Substituting these equations and simplifying for the equations of the kinetic energy, results in an expression for the kinetic energy of the second pendulum (A.16).

$$
\begin{aligned}
T_2 = \frac{1}{2} \, m_2 \, (&L_1^2 \dot{\theta}_1^2 + L_1^2 \dot{\phi}_1^2 \, sin^2(\theta_1) + L_2^2 \dot{\theta}_2^2 + L_2^2 \dot{\phi}_2^2 \, sin^2(\theta_2) \\
&+ 2L_1L_2\dot{\theta}_1\dot{\theta}_2(cos(\theta_1)cos(\theta_2)cos(\phi_1 - \phi_2) + sin(\theta_1)sin(\theta_2)) \\
&+ 2L_1L_2\dot{\theta}_1\dot{\phi}_2cos(\theta_1)sin(\theta_2)sin(\phi_1 - \phi_2) \\
&+ 2L_1L_2\dot{\phi}_1\dot{\theta}_2sin(\theta_1)cos(\theta_2)sin(\phi_2 - \phi_1) \\
&+ 2L_1L_2\dot{\phi}_1\dot{\phi}_2sin(\theta_1)sin(\theta_2)cos(\phi_1 - \phi_2))
\end{aligned}
\quad \text{(A.16)}
$$

A.1.3. Potential Energy
For the potential energy, only the z-coordinate of the pendulum bobs is needed. The equations for the potential energy are given in (A.17) and (A.18).

$$V_1 = m_1 \, g \, z_1 = -m_1 \, g \, L_1 \, cos(\theta_1) \quad \text{(A.17)}$$

$$V_2 = m_2 \, g \, z_2 = -m_2 \, g \, L_1 \, cos(\theta_1) - m_2 \, g \, L_2 \, cos(\theta_2) \quad \text{(A.18)}$$

A.1.4. The Euler-Lagrange per generalised coordinate
The total Lagrange is then equal to equation (A.19).

$$
\begin{aligned}
L =& (T_1 + T_2) - (V_1 + V_2) \\
=& \frac{1}{2} \, (m_1 + m_2) \, L_1^2 \dot{\theta}_1^2 + \frac{1}{2} \, (m_1 + m_2) \, L_1^2 \dot{\phi}_1^2 \, sin^2(\theta_1) + \frac{1}{2} \, m_2 \, L_2^2 \dot{\theta}_2^2 + \frac{1}{2} \, m_2 \, L_2^2 \dot{\phi}_2^2 \, sin^2(\theta_2) \\
&+ m_2L_1L_2\dot{\theta}_1\dot{\theta}_2(cos(\theta_1)cos(\theta_2)cos(\phi_1 - \phi_2) + sin(\theta_1)sin(\theta_2)) + m_2L_1L_2\dot{\theta}_1\dot{\phi}_2cos(\theta_1)sin(\theta_2)sin(\phi_1 - \phi_2) \\
&+ m_2L_1L_2\dot{\phi}_1\dot{\theta}_2sin(\theta_1)cos(\theta_2)sin(\phi_2 - \phi_1) + m_2L_1L_2\dot{\phi}_1\dot{\phi}_2sin(\theta_1)sin(\theta_2)cos(\phi_1 - \phi_2) \\
&+ (m_1 + m_2) \, g \, L_1 \, cos(\theta_1) + m_2 \, g \, L_2 \, cos(\theta_2)
\end{aligned}
$$

$$\text{(A.19)}$$

After the Lagrangian is defined, the basic Euler-Lagrange equations for every generalised coordinate can be constructed, as shown in (A.20), (A.21), (A.22), (A.23).

$$
\begin{aligned}
\frac{d}{dt}(\frac{\partial L}{\partial \dot{\theta}_1}) - \frac{\partial L}{\partial \theta_1} =& (m1 + m2)L_1^2 \ddot{\theta}_1 - (m1 + m2)L_1^2cos(\theta_1)sin(\theta_1)\dot{\phi}_1^2 \\
&+ m_2L_1L_2(sin(\theta_1)sin(\theta_2) + cos(\theta_1)cos(\theta_2)cos(\phi_1 - \phi_2))\ddot{\theta}_2 + m_2L_1L_2cos(\theta_1)sin(\theta_2)sin(\phi_1 - \phi_2)\ddot{\phi}_2 \\
&+ m_2L_1L_2(sin(\theta_1)cos(\theta_2) - cos(\theta_1)sin(\theta_2)cos(\phi_1 - \phi_2))\dot{\theta}_2^2 - m_2L_1L_2cos(\theta_1)sin(\theta_2)cos(\phi_1 - \phi_2)\dot{\phi}_2^2 \\
&+ 2m_2L_1L_2cos(\theta_1)cos(\theta_2)sin(\phi_1 - \phi_2)\dot{\theta}_2\dot{\phi}_2 + (m_1 + m_2)gL_1sin(\theta_1) = 0
\end{aligned}
$$

$$\text{(A.20)}$$

$$
\begin{aligned}
\frac{d}{dt}(\frac{\partial L}{\partial \dot{\phi}_1}) - \frac{\partial L}{\partial \phi_1} =& (m1 + m2)L_1^2sin^2(\theta_1)\ddot{\phi}_1 + 2(m_1 + m_2)L_1^2cos(\theta_1)sin(\theta_1)\dot{\theta}_1\dot{\phi}_1 \\
&+ m_2L_1L_2sin(\theta_1)sin(\theta_2)cos(\phi_1 - \phi_2)\ddot{\phi}_2 - m_2L_1L_2sin(\theta_1)cos(\theta_2)sin(\phi_1 - \phi_2)\ddot{\theta}_2 \\
&+ m_2L_1L_2sin(\theta_1)sin(\theta_2)sin(\phi_1 - \phi_2)\dot{\theta}_2^2 + m_2L_1L_2sin(\theta_1)sin(\theta_2)sin(\phi_1 - \phi_2)\dot{\phi}_2^2 \\
&+ 2m_2L_1L_2sin(\theta_1)cos(\theta_2)cos(\phi_1 - \phi_2)\dot{\theta}_2\dot{\phi}_1 = 0
\end{aligned}
\quad \text{(A.21)}
$$

$$\frac{d}{dt}\left(\frac{\partial L}{\partial \dot{\theta}_2}\right) - \frac{\partial L}{\partial \theta_2} = m_2 L_2^2 \ddot{\theta}_2 - m_2 L_2^2 cos(\theta_2)sin(\theta_2)\dot{\phi}_2^2$$
$$+ m_2 L_1 L_2 (sin(\theta_1)sin(\theta_2) + cos(\theta_1)cos(\theta_2)cos(\phi_1 - \phi_2))\ddot{\theta}_1 - m_2 L_1 L_2 sin(\theta_1)cos(\theta_2)sin(\phi_1 - \phi_2)\ddot{\phi}_1$$
$$+ m_2 L_1 L_2 (cos(\theta_1)sin(\theta_2) - sin(\theta_1)cos(\theta_2)cos(\phi_1 - \phi_2))\dot{\theta}_1^2 - m_2 L_1 L_2 sin(\theta_1)cos(\theta_2)cos(\phi_1 - \phi_2)\dot{\phi}_1^2$$
$$- 2m_2 L_1 L_2 cos(\theta_1)cos(\theta_2)sin(\phi_1 - \phi_2)\dot{\theta}_1\dot{\phi}_1 + m_2 g L_2 sin(\theta_2) = 0$$

(A.22)

$$\frac{d}{dt}\left(\frac{\partial L}{\partial \dot{\phi}_2}\right) - \frac{\partial L}{\partial \phi_2} = m_2 L_2^2 sin^2(\theta_2)\ddot{\phi}_2 + 2m_2 L_2^2 cos(\theta_2)sin(\theta_2)\dot{\theta}_2\dot{\phi}_2$$
$$+ m_2 L_1 L_2 sin(\theta_1)sin(\theta_2)cos(\phi_1 - \phi_2)\ddot{\phi}_1 + m_2 L_1 L_2 cos(\theta_1)sin(\theta_2)sin(\phi_1 - \phi_2)\ddot{\theta}_1$$
$$- m_2 L_1 L_2 sin(\theta_1)sin(\theta_2)sin(\phi_1 - \phi_2)\dot{\theta}_1^2 - m_2 L_1 L_2 sin(\theta_1)sin(\theta_2)sin(\phi_1 - \phi_2)\dot{\phi}_1^2$$
$$+ 2m_2 L_1 L_2 cos(\theta_1)sin(\theta_2)cos(\phi_1 - \phi_2)\dot{\theta}_1\dot{\phi}_1 = 0$$

(A.23)

A.2. Equation of Motion

After the basic E-L equations for the set of generalised coordinates are determined, the complete set of equations of motion can be constructed by including damping and forces to the E-L equations.

A.2.1. Dissipation Function

The Rayleigh dissipation function is determined by $D = \frac{1}{2}b(v_1^2 + v_2^2)$. This results in the total dissipation function as described in equation (A.24)

$$D = \frac{1}{2}b(2L_1^2\dot{\theta}_1 + 2L_1^2\dot{\phi}_1^2 sin^2(\theta_1) + L_2^2\dot{\theta}_2 + L_2^2\dot{\phi}_2^2 sin^2(\theta_2)$$
$$+ 2L_1 L_2\dot{\theta}_1\dot{\theta}_2(cos(\theta_1)cos(\theta_2)cos(\phi_1 - \phi_2) + sin(\theta_1)sin(\theta_2))$$
$$+ 2L_1 L_2\dot{\theta}_1\dot{\phi}_2 cos(\theta_1)sin(\theta_2)sin(\phi_1 - \phi_2)$$
$$+ 2L_1 L_2\dot{\phi}_1\dot{\theta}_2 sin(\theta_1)cos(\theta_2)sin(\phi_2 - \phi_1)$$
$$+ 2L_1 L_2\dot{\phi}_1\dot{\phi}_2 sin(\theta_1)sin(\theta_2)cos(\phi_1 - \phi_2))$$

(A.24)

By taking the partial derivative of the dissipation function with respect to the differential of the generalised coordinate, the dissipative terms that must be included in the equations of motion are determined.

$$\frac{\partial D}{\partial \dot{\theta}_1} = 2b\,L_1^2\,\dot{\theta}_1 + bL_1 L_2(cos(\theta_1)cos(\theta_2)cos(\phi_1 - \phi_2)$$
$$+ sin(\theta_1)sin(\theta_2))\dot{\theta}_2 + bL_1 L_2 cos(\theta_1)sin(\theta_2)sin(\phi_1 - \phi_2)\dot{\phi}_2$$

(A.25)

$$\frac{\partial D}{\partial \dot{\phi}_1} = 2bL_1^2\dot{\phi}_1 sin^2(\theta_1) - bL_1 L_2 sin(\theta_1)cos(\theta_2)sin(\phi_1 - \phi_2)\dot{\theta}_2$$
$$+ bL_1 L_2 sin(\theta_1)sin(\theta_2)cos(\phi_1 - \phi_2)\dot{\phi}_2$$

(A.26)

$$\frac{\partial D}{\partial \dot{\theta}_2} = b\,L_2^2\,\dot{\theta}_2 + bL_1 L_2(cos(\theta_1)cos(\theta_2)cos(\phi_1 - \phi_2)$$
$$+ sin(\theta_1)sin(\theta_2))\dot{\theta}_1 - bL_1 L_2 sin(\theta_1)cos(\theta_2)sin(\phi_1 - \phi_2)\dot{\phi}_1$$

(A.27)

$$\frac{\partial D}{\partial \dot{\phi}_2} = bL_2^2\dot{\phi}_2 sin^2(\theta_2) + bL_1 L_2 cos(\theta_1)sin(\theta_2)sin(\phi_1 - \phi_2)\dot{\theta}_1 + bL_1 L_2 sin(\theta_1)sin(\theta_2)cos(\phi_1 - \phi_2)\dot{\phi}_1 \quad \text{(A.28)}$$

A.2.2. generalised Forces

The equation for the generalised force is given in equation (A.29).

$$Q_j = \mathbf{F}_1 \frac{\partial \mathbf{r}_1}{\partial q_j} + \mathbf{F}_2 \frac{\partial \mathbf{r}_2}{\partial q_j} \tag{A.29}$$

A horizontal force will be applied to the system, meaning in the xy-plane. The forces $\mathbf{F}_1$ and $\mathbf{F}_2$ can represent oscillating or normal excitation forces.

$$\mathbf{F}_1 = (F_{x_1}, F_{y_1}, 0)^T \tag{A.30}$$

$$\mathbf{F}_2 = (F_{x_2}, F_{y_2}, 0)^T \tag{A.31}$$

The position vectors (A.32) and (A.33) are needed to determine the generalised force.

$$\mathbf{r}_1 = (L_1 sin\theta_1 cos\phi_1, L_1 sin\theta_1 sin\phi_1, -L_1 cos\theta_1)^T \tag{A.32}$$

$$\mathbf{r}_2 = (L_1 sin\theta_1 cos\phi_1 + L_2 sin\theta_2 cos\phi_2, L_1 sin\theta_1 sin\phi_1 + L_2 sin\theta_2 sin\phi_2, -L_1 cos\theta_1 - L_2 cos\theta_2)^T \tag{A.33}$$

Next, the expressions for the generalised force per generalised can be constructed.

$$
\begin{aligned}
Q_{\theta_1} &= \mathbf{F}_1 \frac{\partial \mathbf{r}_1}{\partial \theta_1} + \mathbf{F}_2 \frac{\partial \mathbf{r}_2}{\partial \theta_1} = \begin{bmatrix} F_{x_1} \\ F_{y_1} \\ 0 \end{bmatrix} \begin{bmatrix} L_1 cos\theta_1 cos\phi_1 \\ L_1 cos\theta_1 sin\phi_1 \\ L_1 sin\theta_1 \end{bmatrix} + \begin{bmatrix} F_{x_2} \\ F_{y_2} \\ 0 \end{bmatrix} \begin{bmatrix} L_1 cos\theta_1 cos\phi_1 \\ L_1 cos\theta_1 sin\phi_1 \\ L_1 sin\theta_1 \end{bmatrix} \\
&= (F_{x_1} + F_{x_2}) L_1 cos\theta_1 cos\phi_1 + (F_{y_1} + F_{y_2}) L_1 cos\theta_1 sin\phi_1
\end{aligned}
\tag{A.34}
$$

$$
\begin{aligned}
Q_{\phi_1} &= \mathbf{F}_1 \frac{\partial \mathbf{r}_1}{\partial \phi_1} + \mathbf{F}_2 \frac{\partial \mathbf{r}_2}{\partial \phi_1} = \begin{bmatrix} F_{x_1} \\ F_{y_1} \\ 0 \end{bmatrix} \begin{bmatrix} -L_1 sin\theta_1 sin\phi_1 \\ L_1 sin\theta_1 cos\phi_1 \\ 0 \end{bmatrix} + \begin{bmatrix} F_{x_2} \\ F_{y_2} \\ 0 \end{bmatrix} \begin{bmatrix} -L_1 sin\theta_1 sin\phi_1 \\ L_1 sin\theta_1 cos\phi_1 \\ 0 \end{bmatrix} \\
&= -(F_{x_1} + F_{x_2}) L_1 sin\theta_1 sin\phi_1 + (F_{y_1} + F_{y_2}) L_1 sin\theta_1 cos\phi_1
\end{aligned}
\tag{A.35}
$$

$$
\begin{aligned}
Q_{\theta_2} &= \mathbf{F}_1 \frac{\partial \mathbf{r}_1}{\partial \theta_2} + \mathbf{F}_2 \frac{\partial \mathbf{r}_2}{\partial \theta_2} = \begin{bmatrix} F_{x_1} \\ F_{y_1} \\ 0 \end{bmatrix} \begin{bmatrix} 0 \\ 0 \\ 0 \end{bmatrix} + \begin{bmatrix} F_{x_2} \\ F_{y_2} \\ 0 \end{bmatrix} \begin{bmatrix} L_2 cos\theta_2 cos\phi_2 \\ L_2 cos\theta_2 sin\phi_2 \\ L_2 sin\theta_2 \end{bmatrix} \\
&= F_{x_2} L_2 cos\theta_2 cos\phi_2 + F_{y_2} L_2 cos\theta_2 sin\phi_2
\end{aligned}
\tag{A.36}
$$

$$
\begin{aligned}
Q_{\phi_2} &= \mathbf{F}_1 \frac{\partial \mathbf{r}_1}{\partial \phi_2} + \mathbf{F}_2 \frac{\partial \mathbf{r}_2}{\partial \phi_2} = \begin{bmatrix} F_{x_1} \\ F_{y_1} \\ 0 \end{bmatrix} \begin{bmatrix} 0 \\ 0 \\ 0 \end{bmatrix} + \begin{bmatrix} F_{x_2} \\ F_{y_2} \\ 0 \end{bmatrix} \begin{bmatrix} -L_2 sin\theta_2 sin\phi_2 \\ L_2 sin\theta_2 cos\phi_2 \\ 0 \end{bmatrix} \\
&= -F_{x_2} L_2 sin\theta_2 sin\phi_2 + F_{y_2} L_2 sin\theta_2 cos\phi_2
\end{aligned}
\tag{A.37}
$$

A.2.3. Total Equation of Motion

Now all the terms needed to construct the complete equation of motion for every generalised coordinate are known.

The equation of motion for θ_1

$$\frac{d}{dt}\left(\frac{\partial L}{\partial \dot{\theta}_1}\right) - \frac{\partial L}{\partial \theta_1} + \frac{\partial D}{\partial \dot{\theta}_1} = Q_{\theta_1} \tag{A.38}$$

$$
\begin{aligned}
&(m1+m2)L_1^2\ddot{\theta}_1 - (m1+m2)L_1^2 cos(\theta_1)sin(\theta_1)\dot{\phi}_1^2 + m_2L_1L_2(sin(\theta_1)sin(\theta_2) + cos(\theta_1)cos(\theta_2)cos(\phi_1-\phi_2))\ddot{\theta}_2 \\
&+ m_2L_1L_2cos(\theta_1)sin(\theta_2)sin(\phi_1-\phi_2)\ddot{\phi}_2 + m_2L_1L_2(sin(\theta_1)cos(\theta_2) - cos(\theta_1)sin(\theta_2)cos(\phi_1-\phi_2))\dot{\theta}_2^2 \\
&- m_2L_1L_2cos(\theta_1)sin(\theta_2)cos(\phi_1-\phi_2)\dot{\phi}_2^2 + 2m_2L_1L_2cos(\theta_1)cos(\theta_2)sin(\phi_1-\phi_2)\dot{\theta}_2\dot{\phi}_2 \\
&+ (m_1+m_2)gL_1sin(\theta_1) + 2bL_1^2\dot{\theta}_1 + bL_1L_2(cos(\theta_1)cos(\theta_2)cos(\phi_1-\phi_2) + sin(\theta_1)sin(\theta_2))\dot{\theta}_2 \\
&+ bL_1L_2cos(\theta_1)sin(\theta_2)sin(\phi_1-\phi_2)\dot{\phi}_2 \\
&= (F_{x_1} + F_{x_2})\,L_1\,cos\theta_1\,cos\phi_1 + (F_{y_1} + F_{y_2})\,L_1cos\theta_1\,sin\phi_1
\end{aligned}
$$
$$\tag{A.39}$$

The equation of motion for ϕ_1

$$\frac{d}{dt}\left(\frac{\partial L}{\partial \dot{\phi}_1}\right) - \frac{\partial L}{\partial \phi_1} + \frac{\partial D}{\partial \dot{\phi}_1} = Q_{\phi_1} \tag{A.40}$$

$$
\begin{aligned}
&(m1+m2)L_1^2 sin^2(\theta_1)\ddot{\phi}_1 + 2(m_1+m_2)L_1^2 cos(\theta_1)sin(\theta_1)\dot{\theta}_1\dot{\phi}_1 \\
&+ m_2L_1L_2sin(\theta_1)sin(\theta_2)cos(\phi_1-\phi_2)\ddot{\phi}_2 - m_2L_1L_2sin(\theta_1)cos(\theta_2)sin(\phi_1-\phi_2)\ddot{\theta}_2 \\
&+ m_2L_1L_2sin(\theta_1)sin(\theta_2)sin(\phi_1-\phi_2)\dot{\theta}_2^2 + m_2L_1L_2sin(\theta_1)sin(\theta_2)sin(\phi_1-\phi_2)\dot{\phi}_2^2 \\
&+ 2m_2L_1L_2sin(\theta_1)cos(\theta_2)cos(\phi_1-\phi_2)\dot{\theta}_2\dot{\phi}_1 + 2bL_1^2\dot{\phi}_1sin^2(\theta_1) - bL_1L_2sin(\theta_1)cos(\theta_2)sin(\phi_1-\phi_2)\dot{\theta}_2 \\
&+ bL_1L_2sin(\theta_1)sin(\theta_2)cos(\phi_1-\phi_2)\dot{\phi}_2 \\
&= -(F_{x_1} + F_{x_2})\,L_1\,sin\theta_1\,sin\phi_1 + (F_{y_1} + F_{y_2})\,L_1sin\theta_1\,cos\phi_1
\end{aligned}
$$
$$\tag{A.41}$$

The equation of motion for θ_2

$$\frac{d}{dt}\left(\frac{\partial L}{\partial \dot{\theta}_2}\right) - \frac{\partial L}{\partial \theta_2} + \frac{\partial D}{\partial \dot{\theta}_2} = Q_{\theta_2} \tag{A.42}$$

$$
\begin{aligned}
&m_2L_2^2\ddot{\theta}_2 - m_2L_2^2cos(\theta_2)sin(\theta_2)\dot{\phi}_2^2 + m_2L_1L_2(sin(\theta_1)sin(\theta_2) + cos(\theta_1)cos(\theta_2)cos(\phi_1-\phi_2))\ddot{\theta}_1 \\
&- m_2L_1L_2sin(\theta_1)cos(\theta_2)sin(\phi_1-\phi_2)\ddot{\phi}_1 + m_2L_1L_2(cos(\theta_1)sin(\theta_2) - sin(\theta_1)cos(\theta_2)cos(\phi_1-\phi_2))\dot{\theta}_1^2 \\
&- m_2L_1L_2sin(\theta_1)cos(\theta_2)cos(\phi_1-\phi_2)\dot{\phi}_1^2 - 2m_2L_1L_2cos(\theta_1)cos(\theta_2)sin(\phi_1-\phi_2)\dot{\theta}_1\dot{\phi}_1 \\
&+ m_2gL_2sin(\theta_2) + bL_2^2\dot{\theta}_2 + bL_1L_2(cos(\theta_1)cos(\theta_2)cos(\phi_1-\phi_2) \\
&+ sin(\theta_1)sin(\theta_2))\dot{\theta}_1 - bL_1L_2sin(\theta_1)cos(\theta_2)sin(\phi_1-\phi_2)\dot{\phi}_1 \\
&= F_{x_2}\,L_2\,cos\theta_2\,cos\phi_2 + F_{y_2}\,L_2cos\theta_2\,sin\phi_2
\end{aligned}
$$
$$\tag{A.43}$$

The equation of motion for ϕ_2

$$\frac{d}{dt}\left(\frac{\partial L}{\partial \dot{\phi}_2}\right) - \frac{\partial L}{\partial \phi_2} + \frac{\partial D}{\partial \dot{\phi}_2} = Q_{\phi_2} \tag{A.44}$$

$$
\begin{aligned}
&m_2L_2^2 sin^2(\theta_2)\ddot{\phi}_2 + 2m_2L_2^2cos(\theta_2)sin(\theta_2)\dot{\theta}_2\dot{\phi}_2 + m_2L_1L_2sin(\theta_1)sin(\theta_2)cos(\phi_1-\phi_2)\ddot{\phi}_1 \\
&+ m_2L_1L_2cos(\theta_1)sin(\theta_2)sin(\phi_1-\phi_2)\ddot{\theta}_1 - m_2L_1L_2sin(\theta_1)sin(\theta_2)sin(\phi_1-\phi_2)\dot{\theta}_1^2 \\
&- m_2L_1L_2sin(\theta_1)sin(\theta_2)sin(\phi_1-\phi_2)\dot{\phi}_1^2 + 2m_2L_1L_2cos(\theta_1)sin(\theta_2)cos(\phi_1-\phi_2)\dot{\theta}_1\dot{\phi}_1 \\
&+ bL_2^2\dot{\phi}_2 sin^2(\theta_2) + bL_1L_2cos(\theta_1)sin(\theta_2)sin(\phi_1-\phi_2)\dot{\theta}_1 + bL_1L_2sin(\theta_1)sin(\theta_2)cos(\phi_1-\phi_2)\dot{\phi}_1 \\
&= -F_{x_2}\,L_2\,sin\theta_2\,sin\phi_2 + F_{y_2}\,L_2sin\theta_2\,cos\phi_2
\end{aligned}
$$
$$\tag{A.45}$$

Equation of Motion in Matrix Form

The equations of motion are coupled. Therefore, it is more convenient to describe them in matrix form.

$$\begin{bmatrix} M_{11} & M_{12} & M_{13} & M_{14} \\ M_{21} & M_{22} & M_{23} & M_{24} \\ M_{31} & M_{32} & M_{33} & M_{34} \\ M_{41} & M_{42} & M_{43} & M_{44} \end{bmatrix} \begin{bmatrix} \ddot{\theta}_1 \\ \ddot{\phi}_1 \\ \ddot{\theta}_2 \\ \ddot{\phi}_2 \end{bmatrix} + \begin{bmatrix} C_{11} & C_{12} & C_{13} & C_{14} \\ C_{21} & C_{22} & C_{23} & C_{24} \\ C_{31} & C_{32} & C_{33} & C_{34} \\ C_{41} & C_{42} & C_{43} & C_{44} \end{bmatrix} \begin{bmatrix} \dot{\theta}_1 \\ \dot{\phi}_1 \\ \dot{\theta}_2 \\ \dot{\phi}_2 \end{bmatrix} + \begin{bmatrix} G_1 \\ G_2 \\ G_3 \\ G_4 \end{bmatrix} = \begin{bmatrix} Q_1 \\ Q_2 \\ Q_3 \\ Q_4 \end{bmatrix} \tag{A.46}$$

The mass matrix M is symmetrical. The terms within the matrix are shown below.

$$M_{11} = (m_1 + m_2)L_1^2 \tag{A.47}$$

$$M_{12} = 0 \tag{A.48}$$

$$M_{13} = m_2 L_1 L_2(sin(\theta_1)sin(\theta_2) + cos(\theta_1)cos(\theta_2)cos(\phi_1 - \phi_2)) \tag{A.49}$$

$$M_{14} = m_2 L_1 L_2 cos(\theta_1)sin(\theta_2)sin(\phi_1 - \phi_2) \tag{A.50}$$

$$M_{22} = (m_1 + m_2)L_1^2 sin(\theta_1)^2 \tag{A.51}$$

$$M_{23} = -m_2 L_1 L_2 sin(\theta_1)cos(\theta_2)sin(\phi_1 - \phi_2) \tag{A.52}$$

$$M_{24} = m_2 L_1 L_2 sin(\theta_1)sin(\theta_2)cos(\phi_1 - \phi_2) \tag{A.53}$$

$$M_{33} = m_2 L_2^2 \tag{A.54}$$

$$M_{34} = 0 \tag{A.55}$$

$$M_{44} = m_2 L_2^2 sin(\theta_2)^2 \tag{A.56}$$

$$M_{21} = M_{12} \quad M_{31} = M_{13} \quad M_{41} = M_{14} \tag{A.57}$$

$$M_{32} = M_{23} \quad M_{42} = M_{24} \quad M_{43} = M_{34} \tag{A.58}$$

The C matrix consists of the original C matrix and the terms due to damping. The original C matrix following from the basic E-L equations is described by C_u and the terms due to damping are described in the matrix C_d. The total C matrix then equal to $C = C_u + C_d$.

The original C matrix C_u.

$$C_{u_{11}} = C_{u_{22}} = C_{u_{33}} = C_{u_{44}} = 0 \tag{A.59}$$

$$C_{u_{12}} = -(m_1 + m_2)L_1^2 cos(\theta_1)sin(\theta_1)\dot{\phi}_1 \tag{A.60}$$

$$C_{u_{13}} = m_2 L_1 L_2(sin(\theta_1)cos(\theta_2) - cos(\theta_1)sin(\theta_2)cos(\phi_1 - \phi_2))\dot{\theta}_2 \tag{A.61}$$

$$C_{u_{14}} = -m_2 L_1 L_2 cos(\theta_1)sin(\theta_2)cos(\phi_1 - \phi_2)\dot{\phi}_2 + 2m_2 L_1 L_2 cos(\theta_1)cos(\theta_2)sin(\phi_1 - \phi_2)\dot{\theta}_2 \tag{A.62}$$

$$C_{u_{21}} = 2(m_1 + m_2)L_1^2 sin(\theta_1)cos(\theta_1)\dot{\phi}_1 \tag{A.63}$$

$$C_{u_{23}} = m_2 L_1 L_2 sin(\theta_1)sin(\theta_2)sin(\phi_1 - \phi_2)\dot{\theta}_2 + 2m_2 L_1 L_2 sin(\theta_1)cos(\theta_2)cos(\phi_1 - \phi_2)\dot{\phi}_2 \tag{A.64}$$

$$C_{u_{24}} = m_2 L_1 L_2 sin(\theta_1)sin(\theta_2)sin(\phi_1 - \phi_2)\dot{\phi}_2 \tag{A.65}$$

$$C_{u_{31}} = m_2 L_1 L_2(cos(\theta_1)sin(\theta_2) - sin(\theta_1)cos(\theta_2)cos(\phi_1 - \phi_2))\dot{\theta}_1 \tag{A.66}$$

$$C_{u_{32}} = -m_2 L_1 L_2 sin(\theta_1)cos(\theta_2)cos(\phi_1 - \phi_2)\dot{\phi}_1 - 2m_2 L_1 L_2 cos(\theta_1)cos(\theta_2)sin(\phi_1 - \phi_2)\dot{\theta}_1 \tag{A.67}$$

$$C_{u_{34}} = -m_2 L_2^2 cos(\theta_2)sin(\theta_2)\dot{\phi}_2 \tag{A.68}$$

$$C_{u_{41}} = -m_2 L_1 L_2 sin(\theta_1)sin(\theta_2)sin(\phi_1 - \phi_2)\dot{\theta}_1 + 2m_2 L_1 L_2 cos(\theta_1)sin(\theta_2)cos(\phi_1 - \phi_2)\dot{\phi}_1 \tag{A.69}$$

$$C_{u_{42}} = -m_2 L_1 L_2 sin(\theta_1)sin(\theta_2)sin(\phi_1 - \phi_2)\dot{\phi}_1 \tag{A.70}$$

$$C_{u_{43}} = 2m_2 L_2^2 sin(\theta_2)cos(\theta_2)\dot{\phi}_2 \tag{A.71}$$

The terms due to damping C_u.

$$C_{11d} = C_{11} + 2bL_1^2 \tag{A.72}$$

$$C_{13d} = C_{13} + bL_1L_2(cos(\theta_1)cos(\theta_2)cos(\phi_1 - \phi_2) + sin(\theta_1)sin(\theta_2)) \tag{A.73}$$

$$C_{14d} = C_{14} + bL_1L_2cos(\theta_1)sin(\theta_2)sin(\phi_1 - \phi_2) \tag{A.74}$$

$$C_{22d} = C_{22} + 2bL_1^2sin^2(\theta_1) \tag{A.75}$$

$$C_{23d} = C_{23} - bL_1L_2sin(\theta_1)cos(\theta_2)sin(\phi_1 - \phi_2) \tag{A.76}$$

$$C_{24d} = C_{24} + bL_1L_2sin(\theta_1)sin(\theta_2)cos(\phi_1 - \phi_2) \tag{A.77}$$

$$C_{31d} = C_{31} + bL_1L_2(cos(\theta_1)cos(\theta_2)cos(\phi_1 - \phi_2) + sin(\theta_1)sin(\theta_2)) \tag{A.78}$$

$$C_{32d} = C_{32} - bL_1L_2sin(\theta_1)cos(\theta_2)sin(\phi_1 - \phi_2) \tag{A.79}$$

$$C_{33d} = C_{33} + b\,L_2^2 \tag{A.80}$$

$$C_{41d} = C_{41} + bL_1L_2cos(\theta_1)sin(\theta_2)sin(\phi_1 - \phi_2) \tag{A.81}$$

$$C_{42d} = C_{42} + bL_1L_2sin(\theta_1)sin(\theta_2)cos(\phi_1 - \phi_2) \tag{A.82}$$

$$C_{44d} = C_{44} + bL_2^2sin^2(\theta_2) \tag{A.83}$$

The vector G contains the terms due to the potential energy.

$$G_1 = (m_1 + m_2)gL_1sin(\theta_1) \tag{A.84}$$

$$G_3 = m_2gL_2sin(\theta_2) \tag{A.85}$$

$$G_2 = G_4 = 0 \tag{A.86}$$

The vector containing the generalised forces is equal to $[Q_1, Q_2, Q_3, Q_4]^T = [Q_{\theta_1}, Q_{\phi_1}, Q_{\theta_2}, Q_{\phi_2}]^T$

A.3. Semi-Implicit Integration Scheme

The semi-implicit integration sheme used to model the double pendulum is presented in equation (A.87).

$$
\begin{aligned}
\theta_{1,i+1} &= \theta_{1,i} + \dot{\theta}_{1,i+1}\,dt \\
\dot{\theta}_{1,i+1} &= \dot{\theta}_{1,i} + \ddot{\theta}_{1,i}\,dt \\
\phi_{1,i+1} &= \phi_{1,i} + \dot{\phi}_{1,i}\,dt \\
\dot{\phi}_{1,i+1} &= \dot{\phi}_{1,i} + \ddot{\phi}_{1,i}\,dt \\
\theta_{2,i+1} &= \theta_{2,i} + \dot{\theta}_{2,i+1}\,dt \\
\dot{\theta}_{2,i+1} &= \dot{\theta}_{2,i} + \ddot{\theta}_{2,i}\,dt \\
\phi_{2,i+1} &= \phi_{2,i} + \dot{\phi}_{2,i+1}\,dt \\
\dot{\phi}_{2,i+1} &= \dot{\phi}_{2,i} + \ddot{\phi}_{2,i}\,dt
\end{aligned}
\tag{A.87}
$$

The expressions for the second derivatives of the angles that are needed in the integration scheme are calculated using equation (A.88).

$$
\begin{bmatrix} \ddot{\theta}_{1,i} \\ \ddot{\phi}_{1,i} \\ \ddot{\theta}_{1,i} \\ \ddot{\phi}_{1,i} \end{bmatrix} = \begin{bmatrix} M_{11} & M_{12} & M_{13} & M_{14} \\ M_{21} & M_{22} & M_{23} & M_{24} \\ M_{31} & M_{32} & M_{33} & M_{34} \\ M_{41} & M_{42} & M_{43} & M_{44} \end{bmatrix}^{-1} \left(\begin{bmatrix} Q_1 \\ Q_2 \\ Q_3 \\ Q_4 \end{bmatrix} - \begin{bmatrix} C_{11} & C_{12} & C_{13} & C_{14} \\ C_{21} & C_{22} & C_{23} & C_{24} \\ C_{31} & C_{32} & C_{33} & C_{34} \\ C_{41} & C_{42} & C_{43} & C_{44} \end{bmatrix} \begin{bmatrix} \dot{\theta}_{1,i} \\ \dot{\phi}_{1,i} \\ \dot{\theta}_{1,i} \\ \dot{\phi}_{1,i} \end{bmatrix} - \begin{bmatrix} G_1 \\ G_2 \\ G_3 \\ G_4 \end{bmatrix} \right) \tag{A.88}
$$

In the integration the matrix M, vector G and Q are functions of the angles at the current time step. The matrix C is a function of the angles and their derivatives at the current time step.

$$
\begin{aligned}
&M(\theta_{1,i}, \phi_{1,i}, \theta_{2,i}, \phi_{2,i}) \\
&C(\theta_{1,i}, \dot{\theta}_{1,i}, \phi_{1,i}, \dot{\phi}_{1,i}, \theta_{2,i}, \dot{\theta}_{2,i}, \phi_{2,i}, \dot{\phi}_{2,i}) \\
&G(\theta_{1,i}, \phi_{1,i}, \theta_{2,i}, \phi_{2,i}) \\
&Q(\theta_{1,i}, \phi_{1,i}, \theta_{2,i}, \phi_{2,i})
\end{aligned}
\tag{A.89}
$$

String of Pendulums

In this appendix the calculations conducted to construct the numerical model of the string of pendulums are presented. In addition, the numerical scheme used for the model is discussed as well as the equations needed for the Newton-Raphson method.

B.1. Calculations

The equation of motion for each pendulum in x, y and z direction is solved using Newton's second law, see (B.1).

$$m_n\ddot{x}_n = \sum F_{x_n}$$
$$m_n\ddot{y}_n = \sum F_{y_n} \tag{B.1}$$
$$m_n\ddot{z}_n = \sum F_{z_n}$$

The coordinates of each pendulum bob are described by equations (B.2)

$$x_n = x_{n-1} + L_n cos(\theta_n)cos(\phi_n)$$
$$y_n = y_{n-1} + L_n cos(\theta_n)sin(\phi_n) \tag{B.2}$$
$$z_n = z_{n-1} + L_n sin(\theta_n)$$

The velocity of each pendulum bob in x, y and z direction is presented in equation (B.3)

$$\dot{x}_n = \dot{x}_{n-1} - L_n sin(\theta_n)cos(\phi_n)\dot{\theta}_n - L_n cos(\theta_n)sin(\phi_n)\dot{\phi}_n$$
$$\dot{y}_n = \dot{y}_{n-1} - L_n sin(\theta_n)sin(\phi_n)\dot{\theta}_n + L_n cos(\theta_n)cos(\phi_n)\dot{\phi}_n \tag{B.3}$$
$$\dot{z}_n = \dot{z}_{n-1} + L_n cos(\theta_n)\dot{\theta}_n$$

The acceleration of each pendulum bob in x, y and z direction are equal to equations (B.4).

$$\ddot{x}_n = \ddot{x}_{n-1} - L_n sin(\theta_n)cos(\phi_n)\ddot{\theta}_n - L_n cos(\theta_n)sin(\phi_n)\ddot{\phi}_n - L_n cos(\theta_n)cos(\phi_n)\dot{\theta}_n^2$$
$$- L_n cos(\theta_n)cos(\phi_n)\dot{\phi}_n^2 + 2L_n sin(\theta_n)sin(\phi_n)\dot{\theta}_n\dot{\phi}_n$$
$$\ddot{y}_n = \ddot{y}_{n-1} - L_n sin(\theta_n)sin(\phi_n)\ddot{\theta}_n + L_n cos(\theta_n)cos(\phi_n)\ddot{\phi}_n - L_n cos(\theta_n)sin(\phi_n)\dot{\theta}_n^2 \tag{B.4}$$
$$- L_n cos(\theta_n)sin(\phi_n)\dot{\phi}_n^2 + 2L_n sin(\theta_n)cos(\phi_n)\dot{\theta}_n\dot{\phi}_n$$
$$\ddot{z}_n = \ddot{z}_{n-1} + L_n cos(\theta_n)\ddot{\theta}_n - L_n sin(\theta_n)\dot{\theta}_n^2$$

The sum of the forces in x, y and z direction for each node are shown in equation (B.5).

$$\sum F_{x,n} = -T_n cos(\theta_n)cos(\phi_n) + T_{n+1}cos(\theta_{n+1})cos(\phi_{n+1}) - b\,\dot{x}_n + E_{x_n}$$
$$\sum F_{y,n} = -T_n cos(\theta_n)sin(\phi_n) + T_{n+1}cos(\theta_n)sin(\phi_n) - b\,\dot{y}_n + E_{y_n}$$
$$\sum F_{z,n} = T_{n+1}sin(\theta_{n+1}) - T_n sin(\theta_n) - m_n g - b\,\dot{z}_n + E_{z_n}$$

(B.5)

The last pendulum only has one string connecting it to the previous pendulum bob, but there exists no next pendulum. Therefore, the equations for the last pendulum N become as shown in (B.6).

$$\sum F_{x,N} = -T_N cos(\theta_N)cos(\phi_N) - b\,\dot{x}_N + E_{x_N}$$
$$\sum F_{y,N} = -T_N cos(\theta_N)sin(\phi_N) - b\,\dot{y}_N + E_{y_N}$$
$$\sum F_{z,N} = T_N sin(\theta_N) - m_N g - b\,\dot{z}_N + E_{z_N}$$

(B.6)

B.2. Implicit Integration Scheme

The general implicit scheme for a string of pendulum is equal to equations (B.7) to (B.11).

$$\theta_{n,i+1} = \theta_{n,i} + \dot{\theta}_{n,i+1}\,dt$$

(B.7)

$$m_n\,\ddot{x}_{n,i+1} =$$
$$-T_{n,i+1}cos(\theta_{n,i+1})cos(\phi_{n,i+1}) + T_{n+1,i+1}cos(\theta_{n+1,i+1})cos(\phi_{n+1,i+1}) - b\,\dot{x}_{n,i+1} + E_{x_{n,i+1}}$$

(B.8)

$$\phi_{n,i+1} = \phi_{n,i} + \dot{\phi}_{n,i+1}\,dt$$

(B.9)

$$m_n\,\ddot{y}_{n,i+1} =$$
$$-T_{n,i+1}cos(\theta_{n,i+1})sin(\phi_{n,i+1}) + T_{n+1,i+1}cos(\theta_{n+1,i+1})sin(\phi_{n+1,i+1}) - b\,\dot{y}_{n,i+1} + E_{y_{n,i+1}}$$

(B.10)

$$m_n\,\ddot{z}_{n,i+1} =$$
$$T_{n+1,i+1}sin(\theta_{n+1,i+1}) - T_{n,i+1}sin(\theta_{n,i+1}) - m_n g - b\,\dot{z}_{n,i+1} + E_{z_{n,i+1}}$$

(B.11)

In these equations the general velocities are discretised according to equation (B.12).

$$\dot{x}_{n,i+1} = \dot{x}_{n-1,i+1} - L_n sin(\theta_{n,i+1})cos(\phi_{n,i+1})\dot{\theta}_{n,i+1} - L_n cos(\theta_{n,i+1})sin(\phi_{n,i+1})\dot{\phi}_{n,i+1}$$
$$\dot{y}_{n,i+1} = \dot{y}_{n-1,i+1} - L_n sin(\theta_{n,i+1})sin(\phi_{n,i+1})\dot{\theta}_{n,i+1} + L_n cos(\theta_{n,i+1})cos(\phi_{n,i+1})\dot{\phi}_{n,i+1}$$
$$\dot{z}_{n,i+1} = \dot{z}_{n-1,i+1} + L_n cos(\theta_{n,i+1})\dot{\theta}_{n,i+1}$$

(B.12)

The acceleration are discretised according to equation B.13.

$$\ddot{x}_{n,i+1} = \ddot{x}_{n-1,i+1} - L_n sin(\theta_{n,i+1})cos(\phi_{n,i+1})\frac{\dot{\theta}_{n,i+1} - \dot{\theta}_{n,i}}{dt} - L_n cos(\theta_{n,i+1})sin(\phi_{n,i+1}))\frac{\dot{\phi}_{n,i+1} - \dot{\phi}_{n,i}}{dt}$$
$$-L_n cos(\theta_{n,i+1})cos(\phi_{n,i+1})\dot{\theta}_{n,i+1}^2 - L_n cos(\theta_{n,i+1})cos(\phi_{n,i+1})\dot{\phi}_{n,i+1}^2 + 2L_n sin(\theta_{n,i+1})sin(\phi_{n,i+1})\dot{\theta}_{n,i+1}\dot{\phi}_{n,i+1}$$

$$\ddot{y}_{n,i+1} = \ddot{y}_{n-1,i+1} - L_n sin(\theta_{n,i+1})sin(\phi_{n,i+1}))\frac{\dot{\theta}_{n,i+1} - \dot{\theta}_{n,i}}{dt} + L_n cos(\theta_{n,i+1})cos(\phi_{n,i+1})\frac{\dot{\phi}_{n,i+1} - \dot{\phi}_{n,i}}{dt}$$
$$-L_n cos(\theta_{n,i+1})sin(\phi_{n,i+1})\dot{\theta}_{n,i+1}^2 - L_n cos(\theta_{n,i+1})sin(\phi_{n,i+1})\dot{\phi}_{n,i+1}^2 + 2L_n sin(\theta_n)cos(\phi_{n,i+1})\dot{\theta}_{n,i+1}\dot{\phi}_{n,i+1}$$

$$\ddot{z}_{n,i+1} = \ddot{z}_{n-1,i+1} + L_n cos(\theta_{n,i+1}))\frac{\dot{\theta}_{n,i+1} - \dot{\theta}_{n,i}}{dt} - L_n sin(\theta_{n,i+1})\dot{\theta}_{n,i+1}^2$$

(B.13)

The set of equations for the last pendulum is equal to the set of equations presented in equation (B.14) to (B.18).

$$\theta_{N,i+1} = \theta_{N,i} + \dot{\theta}_{N,i+1}\, dt \tag{B.14}$$

$$m_N\, \ddot{x}_{N,i+1} = -T_{N,i+1}cos(\theta_{N,i+1})cos(\phi_{N,i+1}) - b\,\dot{x}_{N,i+1} + E_{x_{N,i+1}} \tag{B.15}$$

$$\phi_{N,i+1} = \phi_{N,i} + \dot{\phi}_{N,i+1}\, dt \tag{B.16}$$

$$m_N\, \ddot{y}_{N,i+1} = -T_{N,i+1}cos(\theta_{n,i+1})sin(\phi_{N,i+1}) + -b\,\dot{x}_{N,i+1} + E_{y_{N,i+1}} \tag{B.17}$$

$$m_N\, \ddot{z}_{N,i+1} = -T_{N,i+1}sin(\theta_{N,i+1}) - m_N g - b\,\dot{z}_{N,i+1} + E_{z_{N,i+1}} \tag{B.18}$$

B.3. Newton-Raphson

$$\boldsymbol{Y}_{k+1} = \boldsymbol{Y}_k - \boldsymbol{J}^{-1}\,\boldsymbol{F}(\boldsymbol{Y}_k) \tag{B.19}$$

The set of unknowns for each pendulum is equal to $\boldsymbol{Y}_n$, given in (B.20).

$$\boldsymbol{Y}_n = [\theta_{n,i+1}, \dot{\theta}_{n,i+1}, \phi_{n,i+1}, \dot{\phi}_{n,i+1}, T_{n,i+1}]^T \tag{B.20}$$

The set of functions for each pendulum is equal to equation (B.21).

$$\boldsymbol{F}(\boldsymbol{Y}_n) = [f_{1_n}, f_{2_n}, f_{3_n}, f_{4_n}, f_{5_n}]^T \tag{B.21}$$

The components of the function vector per pendulum are described in equations (B.22) to (B.26).

$$f_{1_n} = \frac{\theta_{n,i+1} - \theta_{n,i}}{dt} - \dot{\theta}_{n,i+1} = 0 \tag{B.22}$$

$$f_{2_n} = m_n\, \ddot{x}_{n,i+1} + T_{n,i+1}cos(\theta_{n,i+1})cos(\phi_{n,i+1}) - T_{n+1,i+1}cos(\theta_{n+1,i+1})cos(\phi_{n+1,i+1}) \\ + b\,\dot{x}_{n,i+1} - E_{x_{n,i+1}} = 0 \tag{B.23}$$

$$f_{3_n} = \frac{\phi_{n,i+1} - \phi_{n,i}}{dt} - \dot{\phi}_{n,i+1} = 0 \tag{B.24}$$

$$f_{4_n} = m_n\, \ddot{y}_{n,i+1} + T_{n,i+1}cos(\theta_{n,i+1})sin(\phi_{n,i+1}) - T_{n+1,i+1}cos(\theta_{n+1,i+1})sin(\phi_{n+1,i+1}) \\ + b\,\dot{x}_{n,i+1} - E_{y_{n,i+1}} = 0 \tag{B.25}$$

$$f_{5_n} = m_n\, \ddot{z}_{n,i+1} - T_{n+1}sin(\theta_{n+1,i+1}) + T_{n,i+1}sin(\theta_{n,i+1}) + m_n g + b\,\dot{z}_{n,i+1} - E_{z_{n,i+1}} = 0 \tag{B.26}$$

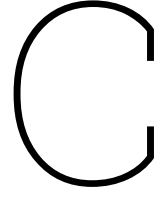The set of equations for the last pendulum become as described in equations (B.27) to (B.31).

$$f_{1_N} = \frac{\theta_{N,i+1} - \theta_{N,i}}{dt} - \dot{\theta}_{N,i+1} = 0 \tag{B.27}$$

$$f_{2_N} = m_N\, \ddot{x}_{N,i+1} + T_{N,i+1}cos(\theta_{N,i+1})cos(\phi_{N,i+1}) + b\,\dot{x}_{N,i+1} - E_{x_{N,i+1}} = 0 \tag{B.28}$$

$$f_{3_N} = \frac{\phi_{N,i+1} - \phi_{N,i}}{dt} - \dot{\phi}_{N,i+1} = 0 \tag{B.29}$$

$$f_{4_N} = m_N\, \ddot{y}_{N,i+1} + T_{N,i+1}cos(\theta_{N,i+1})sin(\phi_{N,i+1}) + b\,\dot{x}_{N,i+1} - E_{y_{N,i+1}} = 0 \tag{B.30}$$

$$f_{5_N} = m_N\, \ddot{z}_{N,i+1} + T_{N,i+1}sin(\theta_{N,i+1}) + m_N g + b\,\dot{z}_{N,i+1} - E_{z_{N,i+1}} = 0 \tag{B.31}$$

C

Mussel Dropper

In this appendix the equations for a catenary curve are presented. Then, the boundary conditions applied in order to transform the string of pendulums into a dropper are shown. Next, the numerical scheme with the Crank-Nicolson method for the model of the dropper and how the wave force is substituted into the scheme are discussed. At last, the time convergence analysis of the 3D model is presented.

C.1. Catenary Curve Equations

The catenary curve equations help to determine a first guess for the numerical model of the mussel dropper. Equation (C.1) determines the position on the curve. The parameter a in this equation has as unit metres and is a constant which determines the shape of the curve. The tension in the curve is determined by equation (C.2), with μ being a parameter for the mass per unit length of the chain. Equation (C.3) is used to determine the angle the curve makes.

$$y = a\,cosh\frac{x}{a} \tag{C.1}$$

$$T = \mu\,g\,y \tag{C.2}$$

$$\phi = 2\,tan^{-1}[tanh(\frac{t}{2a})] \tag{C.3}$$

C.2. Boundary Conditions

For the mussel dropper the equations of motion for the pendulums remain the same as for the string, so equal to (B.1). However, the equations of motion for the last pendulum are replaced with boundary conditions.

$$x_N = \sum L_n\,cos(\theta_n)\,cos(\phi_n) \tag{C.4}$$

$$y_N = \sum L_n\,cos(\theta_n)\,sin(\phi_n) \tag{C.5}$$

$$z_N = \sum -L_n\,sin(\theta_n) \tag{C.6}$$

C.3. Implicit Integration scheme using Crank-Nicolson

The integration scheme for each pendulum becomes as described in equations (C.7) to (C.11).

$$\frac{\theta_{n,i+1} - \theta_{n,i}}{dt} = \gamma\,\dot{\theta}_{n,i+1} + (1 - \gamma)\,\dot{\theta}_{n,i} \tag{C.7}$$

$$ddx_{A_n} = \gamma(ddx_{B_{n,i+1}} - T_{n,i+1}cos(\theta_{n,i+1})cos(\phi_{n,i+1}) + T_{n+1,i+1}cos(\theta_{n+1,i+1})cos(\phi_{n+1,i+1}) - b\dot{x}_{n,i+1} + E_{x_{n,i+1}})$$
$$+ (1-\gamma)(ddx_{B_{n,i}} - T_{n,i}cos(\theta_{n,i})cos(\phi_{n,i}) + T_{n+1,i}cos(\theta_{n+1,i})cos(\phi_{n+1,i}) - b\dot{x}_{n,i} + E_{x_{n,i}})$$

$$(C.8)$$

$$\frac{\phi_{n,i+1} - \phi_{n,i}}{dt} = \gamma\dot{\phi}_{n,i+1} + (1-\gamma)\dot{\phi}_{n,i} \tag{C.9}$$

$$ddy_{A_n} = \gamma(ddy_{B_{n,i+1}} - T_{n,i+1}cos(\theta_{n,i+1})sin(\phi_{n,i+1}) + T_{n+1,i+1}cos(\theta_{n+1,i+1})sin(\phi_{n+1,i+1}) - b\dot{y}_{n,i+1} + E_{y_{n,i+1}})$$
$$+ (1-\gamma)(ddy_{B_{n,i}} - T_{n,i}cos(\theta_{n,i})sin(\phi_{n,i}) + T_{n+1,i}cos(\theta_{n+1,i})sin(\phi_{n+1,i}) - b\dot{y}_{n,i+1} + E_{y_{n,i}})$$

$$(C.10)$$

$$ddz_{A_n} = \gamma(ddz_{B_{n,i+1}} + T_{n+1,i+1}sin(\theta_{n+1,i+1}) - T_{n,i+1}sin(\theta_{n,i+1}) - m_n g - b\dot{z}_{n,i+1} + E_{z_{n,i+1}})$$
$$+ (1-\gamma)(ddz_{B_{n,i}} + T_{n+1,i}sin(\theta_{n+1,i}) - T_{n,i}sin(\theta_{n,i}) - m_n g - b\dot{z}_{n,i} + E_{z_{n,i}})$$

$$(C.11)$$

The terms that split up the second derivatives of the angles are presented in equations (C.12) to (C.20).

$$ddx_{A_n} = ddx_{A_{n-1}} - L_n sin(\theta_{n,i+1})cos(\phi_{n,i+1})\frac{\dot{\theta}_{n,i+1} - \dot{\theta}_{n,i}}{dt} - L_n cos(\theta_{n,i+1})sin(\phi_{n,i+1})\frac{\dot{\phi}_{n,i+1} - \dot{\phi}_{n,i}}{dt}$$

$$(C.12)$$

$$ddx_{B_{n,i+1}} = ddx_{B_{n-1,i+1}} - L_n cos(\theta_{n,i+1})cos(\phi_{n,i+1})\dot{\theta}_{n,i+1}^2 - L_n cos(\theta_{n,i+1})cos(\phi_{n,i+1})\dot{\phi}_{n,i+1}^2$$
$$+ 2L_n sin(\theta_{n,i+1})sin(\phi_{n,i+1})\dot{\theta}_{n,i+1}\dot{\phi}_{n,i+1}$$

$$(C.13)$$

$$ddx_{B_{n,i}} = ddx_{B_{n-1,i}} - L_n cos(\theta_{n,i})cos(\phi_{n,i})\dot{\theta}_{n,i}^2 - L_n cos(\theta_{n,i})cos(\phi_{n,i})\dot{\phi}_{n,i}^2 + 2L_n sin(\theta_{n,i})sin(\phi_{n,i})\dot{\theta}_{n,i}\dot{\phi}_{n,i}$$

$$(C.14)$$

$$ddy_{A_n} = ddy_{A_{n-1}} - L_n sin(\theta_{n,i+1})sin(\phi_{n,i+1}))\frac{\dot{\theta}_{n,i+1} - \dot{\theta}_{n,i}}{dt} + L_n cos(\theta_{n,i+1})cos(\phi_{n,i+1})\frac{\dot{\phi}_{n,i+1} - \dot{\phi}_{n,i}}{dt}$$

$$(C.15)$$

$$ddy_{B_{n,i+1}} = ddy_{B_{n-1,i+1}} - L_n cos(\theta_{n,i+1})sin(\phi_{n,i+1})\dot{\theta}_{n,i+1}^2$$
$$- L_n cos(\theta_{n,i+1})sin(\phi_{n,i+1})\dot{\phi}_{n,i+1}^2 + 2L_n sin(\theta_n)cos(\phi_{n,i+1})\dot{\theta}_{n,i+1}\dot{\phi}_{n,i+1}$$

$$(C.16)$$

$$ddy_{B_{n,i}} = ddy_{B_{n-1,i}} - L_n cos(\theta_{n,i})sin(\phi_{n,i})\dot{\theta}_{n,i}^2 - L_n cos(\theta_{n,i})sin(\phi_{n,i})\dot{\phi}_{n,i}^2 + 2L_n sin(\theta_n)cos(\phi_{n,i})\dot{\theta}_{n,i}\dot{\phi}_{n,i}$$

$$(C.17)$$

$$ddz_{A_n} = ddz_{A_{n-1}} - L_n cos(\theta_{n,i+1}))\frac{\dot{\theta}_{n,i+1} - \dot{\theta}_{n,i}}{dt} \tag{C.18}$$

$$ddz_{B_{n,i+1}} = ddz_{B_{n-1,i+1}} - L_n sin(\theta_{n,i+1})\dot{\theta}_{n,i+1}^2 \tag{C.19}$$

$$ddz_{B_{n,i}} = ddz_{B_{n-1,i}} - L_n sin(\theta_{n,i})\dot{\theta}_{n,i}^2 \tag{C.20}$$

The boundary conditions are discretised as in equation (C.21).

$$x_N = \sum L_n \, cos(\theta_{n,i+1}) \, cos(\phi_{n,i+1})$$
$$y_N = \sum L_n \, cos(\theta_{n,i+1}) \, sin(\phi_{n,i+1}) \tag{C.21}$$
$$z_N = \sum -L_n \, sin(\theta_{n,i+1})$$

C.3.1. Wave Force

To apply a wave force to the system, the terms for the external forces are replaced with equations (C.22), (C.23) and (C.24).

$$E_{x_{n,i+1}} = \frac{\pi}{4} \, \rho_f \, D^2 \, C_M \, \dot{u}_{x_{n,i+1}} + \frac{1}{2} \, \rho_f \, D \, C_D \, u_{x_{n,i+1}} |u_{x_{n,i+1}}| \tag{C.22}$$

$$E_{y_{n,i+1}} = \frac{\pi}{4} \, \rho_f \, D^2 \, C_M \, \dot{u}_{y_{n,i+1}} + \frac{1}{2} \, \rho_f \, D \, C_D \, u_{x_{n,i+1}} |u_{y_{n,i+1}}| \tag{C.23}$$

$$E_{z_{n,i+1}} = \frac{\pi}{4} \, \rho_f \, D^2 \, C_M \, \dot{u}_{z_{n,i+1}} + \frac{1}{2} \, \rho_f \, D \, C_D \, u_{x_{n,i+1}} |u_{z_{n,i+1}}| \tag{C.24}$$

The discretised wave velocities and acceleration are described by equations (C.25) to (C.30).

$$u_{x_{n,i+1}} = \frac{\partial \Phi_w}{\partial x_{n,i+1}} = \eta_a \, \omega \, cos(\mu) \, \frac{cosh(k \, (h + z_{n,i+1}))}{sinh(kh)} \, cos(k \, x_{n,i+1} \, cos(\mu) + k \, y_{n,i+1} \, sin(\mu) - \omega \, t) \tag{C.25}$$

$$u_{y_{n,i+1}} = \frac{\partial \Phi_w}{\partial y_{n,i+1}} = \eta_a \, \omega \, sin(\mu) \, \frac{cosh(k \, (h + z_{n,i+1}))}{sinh(kh)} \, cos(k \, x_{n,i+1} \, cos(\mu) + k \, y_{n,i+1} \, sin(\mu) - \omega \, t) \tag{C.26}$$

$$u_{z_{n,i+1}} = \frac{\partial \Phi_w}{\partial z_{n,i+1}} = \eta_a \, \omega \, \frac{sinh(k \, (h + z_{n,i+1}))}{sinh(kh)} \, sin(k \, x_{n,i+1} \, cos(\mu) + k \, y_{n,i+1} \, sin(\mu) - \omega \, t) \tag{C.27}$$

$$\dot{u}_{x_{n,i+1}} = \frac{\partial \Phi_w}{\partial x_{n,i+1}} = \eta_a \, \omega^2 \, cos(\mu) \, \frac{cosh(k \, (h + z_{n,i+1}))}{sinh(kh)} \, sin(k \, x_{n,i+1} \, cos(\mu) + k \, y_{n,i+1} \, sin(\mu) - \omega \, t) \tag{C.28}$$

$$\dot{u}_{y_{n,i+1}} = \frac{\partial \Phi_w}{\partial y_{n,i+1}} = \eta_a \, \omega^2 \, sin(\mu) \, \frac{cosh(k \, (h + z_{n,i+1}))}{sinh(kh)} \, sin(k \, x_{n,i+1} \, cos(\mu) + k \, y_{n,i+1} \, sin(\mu) - \omega \, t) \tag{C.29}$$

$$\dot{u}_{z_{n,i+1}} = \frac{\partial \Phi_w}{\partial z_{n,i+1}} = \eta_a \, \omega^2 \, \frac{sinh(k \, (h + z_{n,i+1}))}{sinh(kh)} \, cos(k \, x_{n,i+1} \, cos(\mu) + k \, y_{n,i+1} \, sin(\mu) - \omega \, t) \tag{C.30}$$

In the above equations, the discretised positions of the pendulum are expressed by equation (C.31)

$$x_{n,i+1} = x_{n-1,i+1} + L_n cos(\theta_{n,i+1})cos(\phi_{n,i+1})$$
$$y_{n,i+1} = y_{n-1,i+1} + L_n cos(\theta_{n,i+1})sin(\phi_{n,i+1}) \tag{C.31}$$
$$z_{n,i+1} = z_{n-1,i+1} + L_n sin(\theta_{n,i+1})$$

C.4. Newton-Raphson

The set of unknowns per pendulum remains the same for the model of the mussel dropper. The equation vector $F(Y)$ however changes due to the new integration scheme. The new equations vector is described by expressions (C.32) to (C.36).

$$f_{1_n} = \frac{\theta_{n,i+1} - \theta_{n,i}}{dt} - (\gamma \, \dot{\theta}_{n,i+1} + (1 - \gamma) \, \dot{\theta}_{n,i}) = 0 \tag{C.32}$$

$$f_{2_n} = ddx_{A_n} + \gamma(-ddx_{B_{n,i+1}} + T_{n,i+1}cos(\theta_{n,i+1})cos(\phi_{n,i+1})$$
$$- T_{n+1,i+1}cos(\theta_{n+1,i+1})cos(\phi_{n+1,i+1}) + b\,\dot{x}_{n,i+1} - E_{x_{n,i+1}})$$
$$+ (1-\gamma)(-ddx_{B_{n,i}} + T_{n,i}cos(\theta_{n,i})cos(\phi_{n,i}) - T_{n+1,i}cos(\theta_{n+1,i})cos(\phi_{n+1,i})$$
$$+ b\,\dot{x}_{n,i} - E_{x_{n,i}}) = 0 \tag{C.33}$$

$$f_{3_n} = \frac{\phi_{n,i+1} - \phi_{n,i}}{dt} - (\gamma\,\dot{\phi}_{n,i+1} + (1-\gamma)\,\dot{\phi}_{n,i}) = 0 \tag{C.34}$$

$$f_{4_n} = ddy_{A_n} + \gamma(-ddy_{B_{n,i+1}} + T_{n,i+1}cos(\theta_{n,i+1})sin(\phi_{n,i+1})$$
$$- T_{n+1,i+1}cos(\theta_{n+1,i+1})sin(\phi_{n+1,i+1}) + b\,\ddot{y}_{n,i+1} - E_{y_{n,i+1}})$$
$$+ (1-\gamma)(-ddy_{B_{n,i}} + T_{n,i}cos(\theta_{n,i})sin(\phi_{n,i}) - T_{n+1,i}cos(\theta_{n+1,i})sin(\phi_{n+1,i})$$
$$+ b\,\ddot{y}_{n,i+1} - E_{y_{n,i}}) = 0 \tag{C.35}$$

$$f_{5_n} = ddz_{A_n}$$
$$+ \gamma(-ddz_{B_{n,i+1}} - T_{n+1,i+1}sin(\theta_{n+1,i+1}) + T_{n,i+1}sin(\theta_{n,i+1}) + m_n g + b\,\dot{z}_{n,i+1} - E_{z_{n,i+1}})$$
$$+ (1-\gamma)(-ddz_{B_{n,i}} - T_{n+1,i}sin(\theta_{n+1,i}) + T_{n,i}sin(\theta_{n,i}) + m_n g + b\,\dot{z}_{n,i} - E_{z_{n,i}}) = 0 \tag{C.36}$$

The new set of equations for the last pendulum are presented in equations (C.37) to (C.41).

$$f_{1_N} = \frac{\theta_{N,i+1} - \theta_{N,i}}{dt} - (\gamma\dot{\theta}_{N,i+1} + (1-\gamma)\dot{\theta}_{N,i}) = 0 \tag{C.37}$$

$$f_{2_N} = x_N - \sum L_n cos(\theta_{n,i+1})cos(\phi_{n,i+1}) = 0 \tag{C.38}$$

$$f_{3_N} = \frac{\phi_{N,i+1} - \phi_{N,i}}{dt} - (\gamma\dot{\phi}_{N,i+1} + (1-\gamma)\dot{\phi}_{N,i}) = 0 \tag{C.39}$$

$$f_{4_N} = y_N - \sum L_n cos(\theta_{n,i+1})sin(\phi_{n,i+1}) = 0 \tag{C.40}$$

$$f_{5_N} = z_N - \sum -L_n sin(\theta_{n,i+1}) = 0 \tag{C.41}$$

C.5. Time convergence 3D
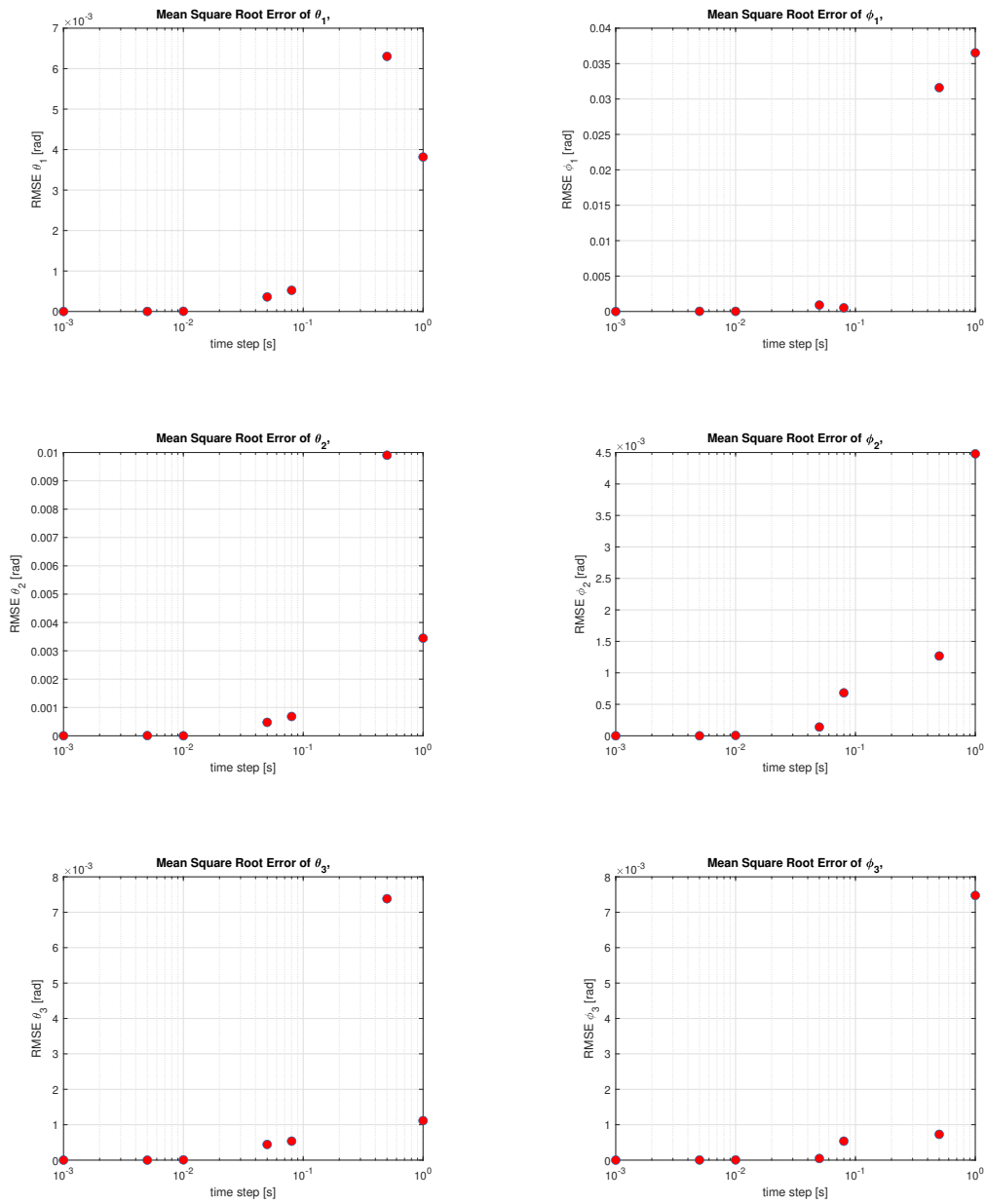
Figure C.1: Time Convergence Analysis for the 3D Model Dropper for the first three polar and azimuth angles.
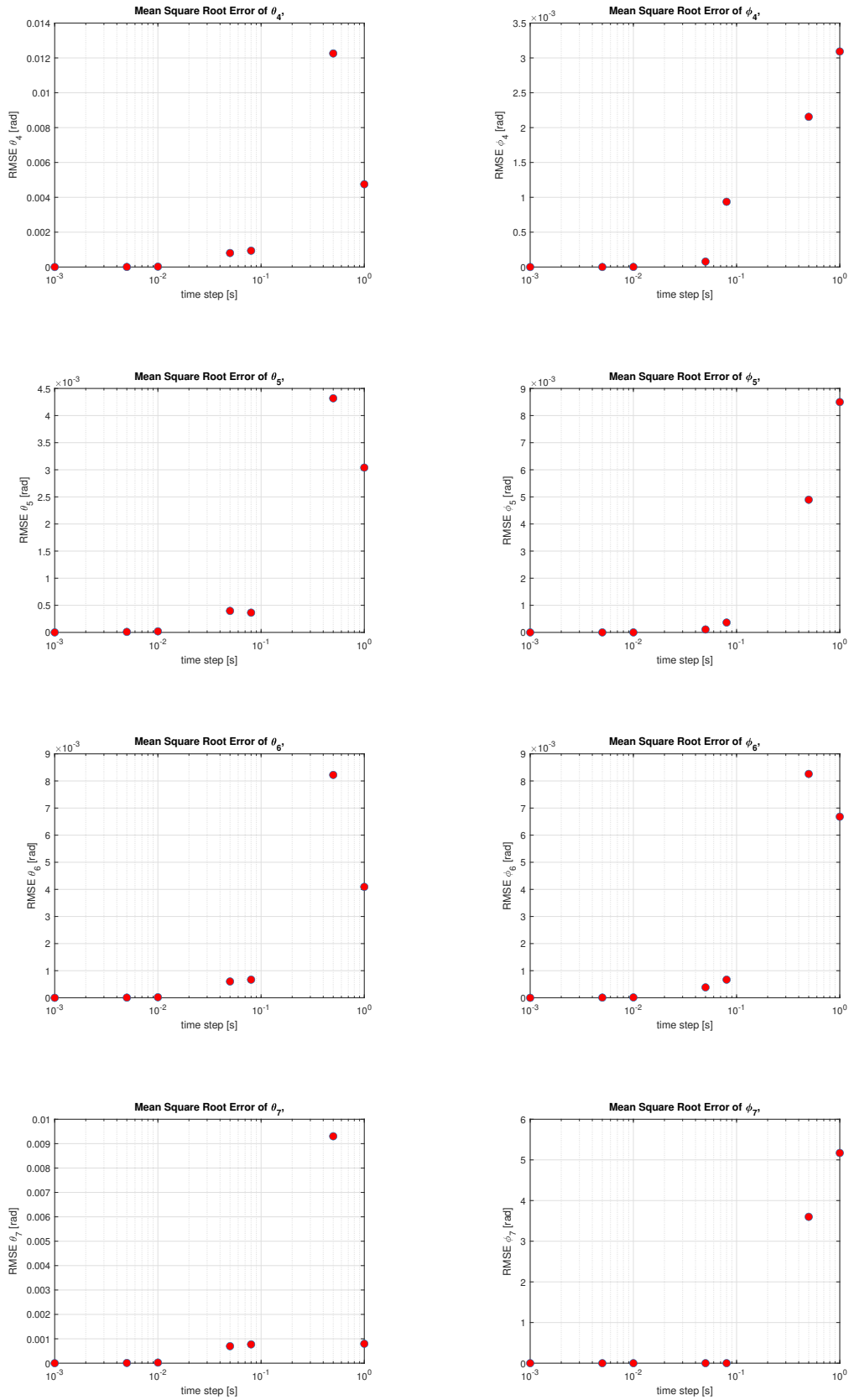
Figure C.2: Time Convergence Analysis for the 3D Model Dropper for the last four polar and azimuth angles.

D

Moment of Inertia

The numerical model is constructed for a simple pendulum, the experiment was however conducted for a compound pendulum. The characteristics of the compound pendulums are described in this appendix.

The moment of inertia for the pendulum of type A and type B, as described in chapter 7, are retrieved from Rhino. The pendulums, bearings and screws were weighted and their weights are denoted in table D.1. Where m_b is the mass of the bearing and m_s is the mass of the screw. The parameter d represents the distance from the pivot point of the pendulum to the point where the screw and bearing are fixed to the pendulum. The parameter y_p is the distance to the neutral line of the pendulum and is retrieved from Rhino.

Parameters of the Compound Pendulum		
I_A	4200562.45	mm^4
I_B	1838492.49	mm^4
m_b	6.2	g
m_s	7.65	g
m_A	19.5	g
m_B	18.6	g
d	150	mm
y_p	75	mm
ρ_p	600	kg/m^3

Table D.1: The values for the parameters of the compound pendulums as used in the experiment.

To obtain the mass moment of inertia for each pendulum the moment of inertia must be multiplied by the density of the material of the pendulum. The pendulums were constructed out of wood, a typical value for the density of wood is used. The total mass moment of inertia for both pendulums is determined by the mass moment of inertia of the pendulum itself and the contribution of the bearing and screw at the end of the pendulum. The calculations for the total mass moment of inertia for each pendulum can be found in (D.1) and (D.2).

$$I_{total,A} = I_A \, \rho_p + (m_b + m_s) \, d^2 \tag{D.1}$$

$$I_{total,B} = I_B \, \rho_p + (m_b + m_s) \, d^2 \tag{D.2}$$

The total equivalent mass of each pendulum is determined by the sum of the mass of the pendulum, the screw and the bearing. The equations for the equivalent masses can be found in (D.3) and (D.4).

$$m_{total,A} = m_A + m_s + m_d \tag{D.3}$$

$$m_{total,B} = m_B + m_s + m_d \tag{D.4}$$

The equivalent length of each pendulum is determined by calculating the neutral axis of each pendulum. The neutral axis is calculated using equation (4.4). This results in the expressions for the neutral axis of pendulum A and B as provided by (D.6) and (D.7).

$$\overline{y} = \frac{\sum y\,m}{\sum m}\text{(4.4)} \tag{D.5}$$

$$y_A = \frac{m_A\,y_p + m_s\,d + m_b\,d}{m_A + m_s + m_d} \tag{D.6}$$

$$y_B = \frac{m_B\,y_p + m_s\,d + m_b\,d}{m_B + m_s + m_d} \tag{D.7}$$

Experimental and Numerical Results

In this appendix, first the two scenarios that were tested, but not used in this thesis are presented E.1, followed by a list of the different combinations of damping coefficients that were tested. Next, a table is presented containing the initial angles of the model dropper at each run and the initial angles of the pendulum in the 2D simulation. Furthermore, all three runs for scenario A are presented in plots for each angle of the model dropper over time. The same is done for scenario B and C. For the last two scenario's, the plot of each pendulum comparing one run to the numerical result with damping is provided.

Scenario D: *Model dropper excited at pendulum 4.*
When the loop is excited at the fourth pendulum, it means that the loop is excited in the vertical direction. This results in a different kind of motion than will be observed in the scenarios before.

Scenario E: *Model dropper excited at pendulum 2 & 3.*
To see whether exciting the loop from 2 pendulums will increase the amplitude of the motion, the loop will be excited at pendulum 2 and 3.

(a) The initial position of the model dropper for scenario D. **(b)** The initial position of the model dropper for scenario E.

Figure E.1: An image of the initial state of the two scenarios that were tested during the experiment, but not used in this thesis.

E.1. Combinations Linear and Quadratic Damping
A listing of the combinations of damping coefficients that were tested in the 2D numerical model and compared with the experimental results.

Combination	b_l in kg/s	b_q in kg
1	0.002	0.500
2	0.002	0.100
3	0.05	0.010
4	0.01	0.010
5	0.004	0.500
6	0.004	0.100
7	0.05	0.030
8	0.01	0.030
9	0.001	0.500
10	0.001	0.100
11	0.05	0.001
12	0.01	0.001
13	0.002	0.010
14	0.004	0.030
15	0.001	0.050

Table E.1: Input for reconstructing experimental scenario A run 2.

E.2. Scenario A
E.2.1. Initial Angles
The external force applied to the 2D numerical model in order to obtain the right initial conditions is shown in equation (E.1)

$$E(2, 1, :) = +min(max(0.094 * (t - 3), 0), M * g) \tag{E.1}$$

The initial angles of each pendulum for run 1, run 2, run 3 and the simulation are presented in table E.2.

Angle [rad]	Run 1	Run 2	Run 3	Model
θ_1	0.1559	0.1528	0.1635	0.1577
θ_2	1.4463	1.4518	1.4513	1.4490
θ_3	1.3535	1.3616	1.3532	1.3606
θ_4	0.8355	0.8410	0.8380	0.8666
θ_5	-1.1678	-1.1545	-1.1591	-1.1492
θ_6	-1.3835	-1.3818	-1.3828	-1.3909
θ_7	-1.4650	-1.4646	-1.4649	1.4571

Table E.2: Table containing the initial angles of the model dropper for the three experiments conducted for scenario A and the initial angles of the reconstruction of scenario A by the 2D numerical model.

E.2.2. Comparison of the Runs
The three runs are compared with each other and plotted per pendulum.
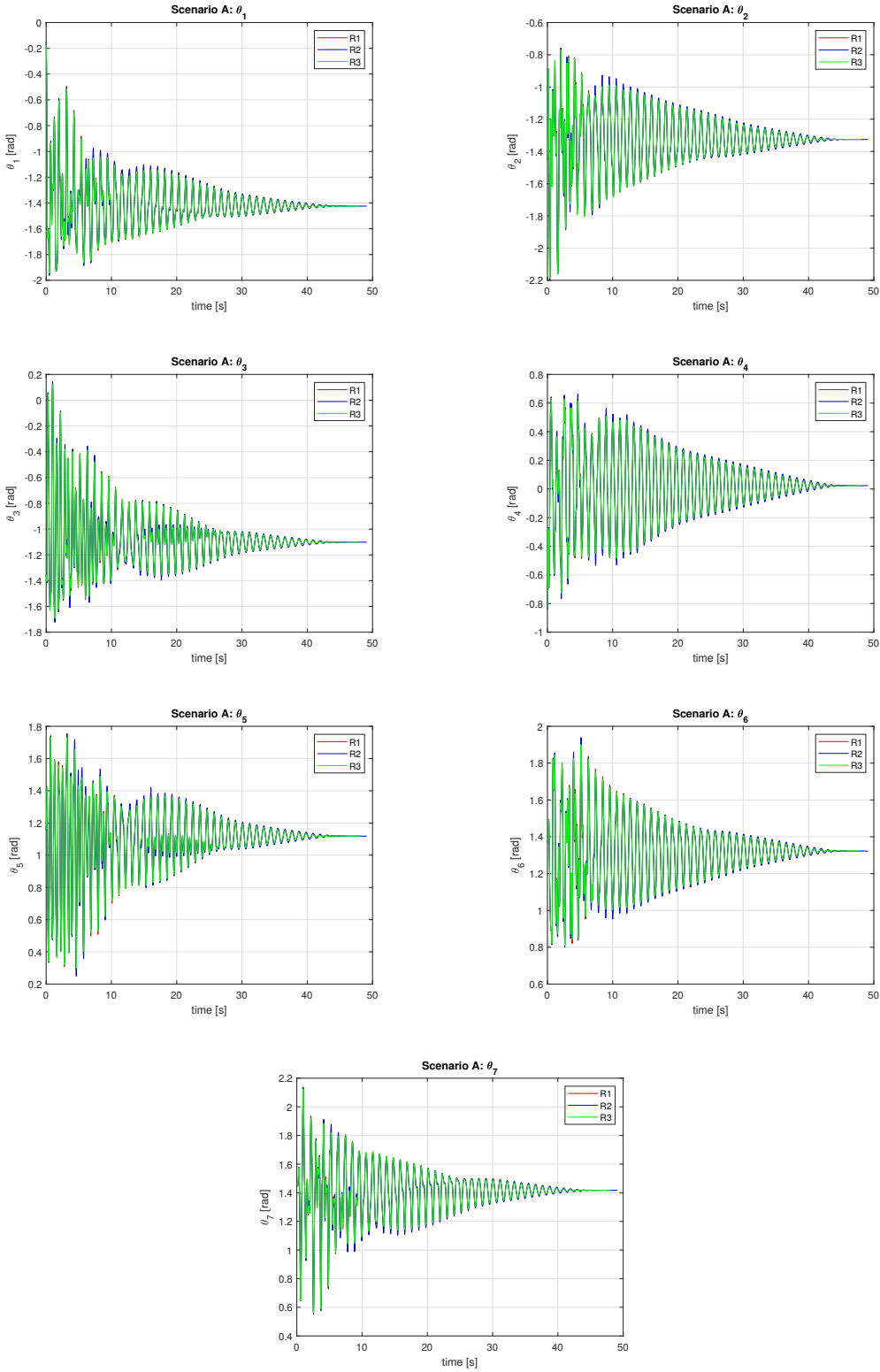
Figure E.2: A plot for every angle of the model dropper over time for scenario A, comparing the angles of the first, second and third run.

E.3. Scenario B

E.3.1. Initial Angles
The external force applied to the 2D numerical model in order to obtain the right initial conditions is shown in equation (E.2)

$$E(2, 1, :) = +min(max(0.065 * (t - 3), 0), M * g) \tag{E.2}$$

The initial angles of each pendulum for run 1, run 2, run 3 and the simulation are presented in table E.3.

Angle [rad]	Run 1	Run 2	Run 3	Model
θ_1	-1.2615	-1.2500	-1.2560	-1.3264
θ_2	-0.2561	-0.1974	-0.2135	-0.2358
θ_3	-1.3867	-1.3887	-1.3883	-1.3713
θ_4	-0.8218	-0.9031	-0.8823	-0.8197
θ_5	1.2719	1.2335	1.2379	1.2286
θ_6	1.4152	1.4141	1.4146	1.4166
θ_7	1.4875	1.4872	1.4871	1.4752

Table E.3: Table containing the initial angles of the model dropper for the three experiments conducted for scenario B and the initial angles of the reconstruction of scenario B by the 2D numerical model.

E.3.2. Comparison of the Runs
The three runs are compared with each other and plotted per pendulum.
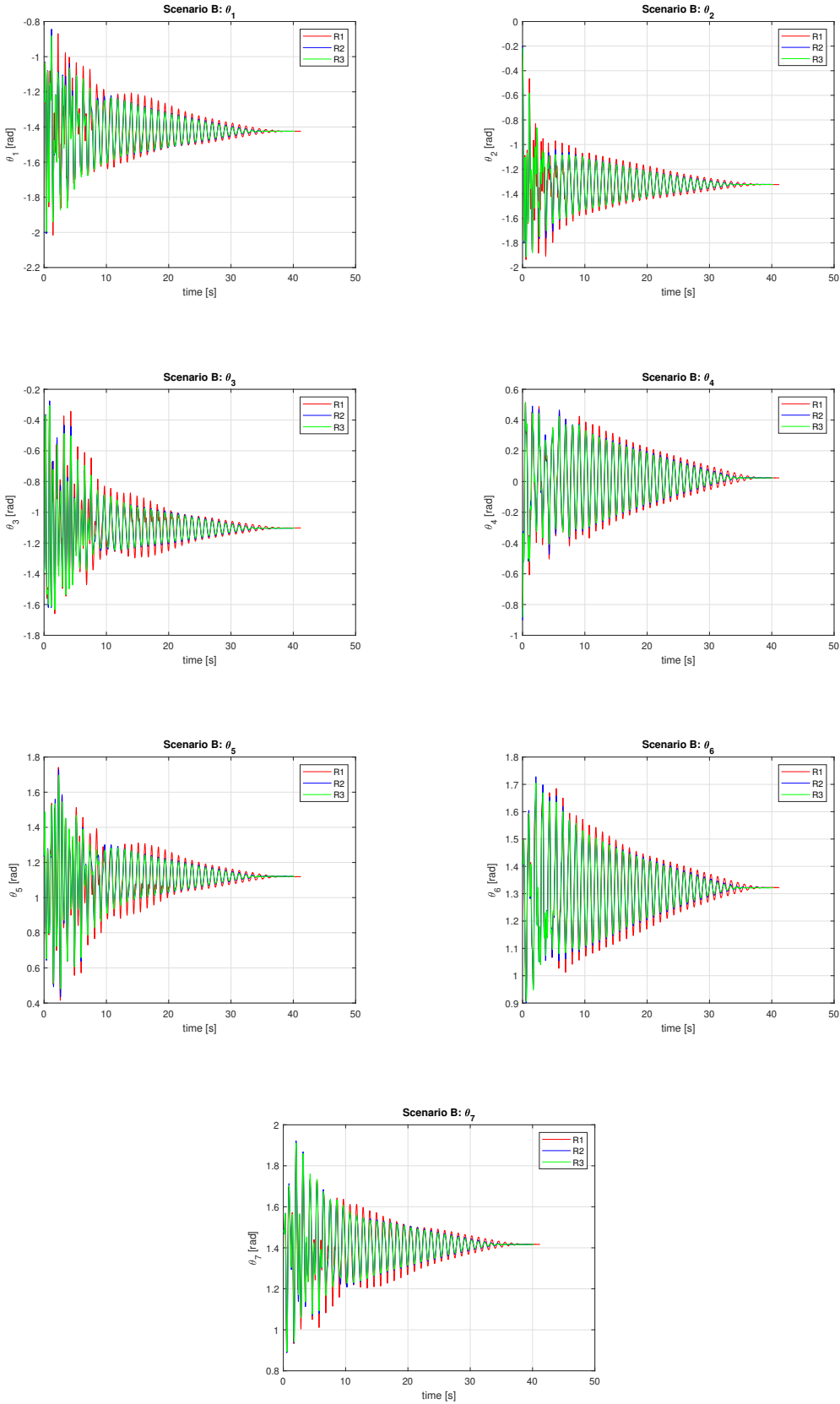
Figure E.3: A plot for every angle of the model dropper over time for scenario B, comparing the angles of the first, second and third run.

E.3.3. Comparison Run with Simulation

Run 1 for scenario B is compared with the results from the 2D model which reconstructed scenario B. The damping coefficients as determined in chapter 8 are applied.
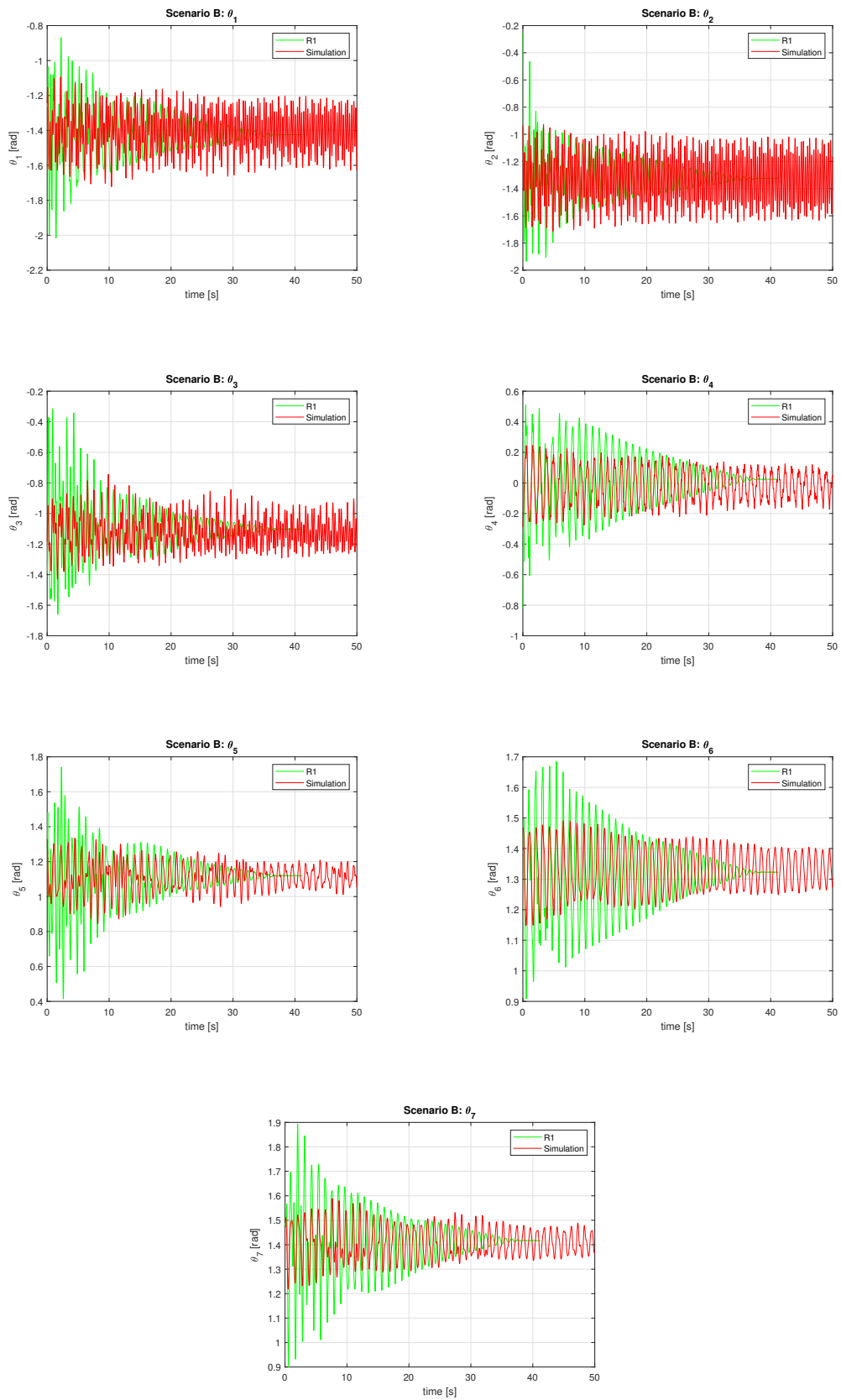
Figure E.4: A plot for every angle of the model dropper over time for scenario B run 1 compared with the results form the 2D simulation with damping coefficients $b_l = 0.002$ kg/s and $b_q = 0.001$ kg.

E.4. Scenario C

E.4.1. Initial Angles

The external force applied to the 2D numerical model in order to obtain the right initial conditions is shown in equation (E.3)

$$E(2, 1, :) = +min(max(0.065 * (t - 3), 0), M * g) \qquad (E.3)$$

The initial angles of each pendulum for run 1, run 2, and the simulation are presented in table E.4.

Angle [rad]	Run 1	Run 2	Model
θ_1	-1.3977	-1.4023	-1.4288
θ_2	-1.1133	-1.1189	-1.2475
θ_3	0.8640	0.8762	0.8729
θ_4	-1.4191	-1.4233	-1.3243
θ_5	0.1358	0.1193	0.1956
θ_6	1.3880	1.3791	1.3396
θ_7	1.4847	1.4748	1.4526

Table E.4: Table containing the initial angles of the model dropper for the three experiments conducted for scenario C and the initial angles of the reconstruction of scenario C by the 2D numerical model.

E.4.2. Comparison of the Runs

The two runs are compared with each other and plotted per pendulum.
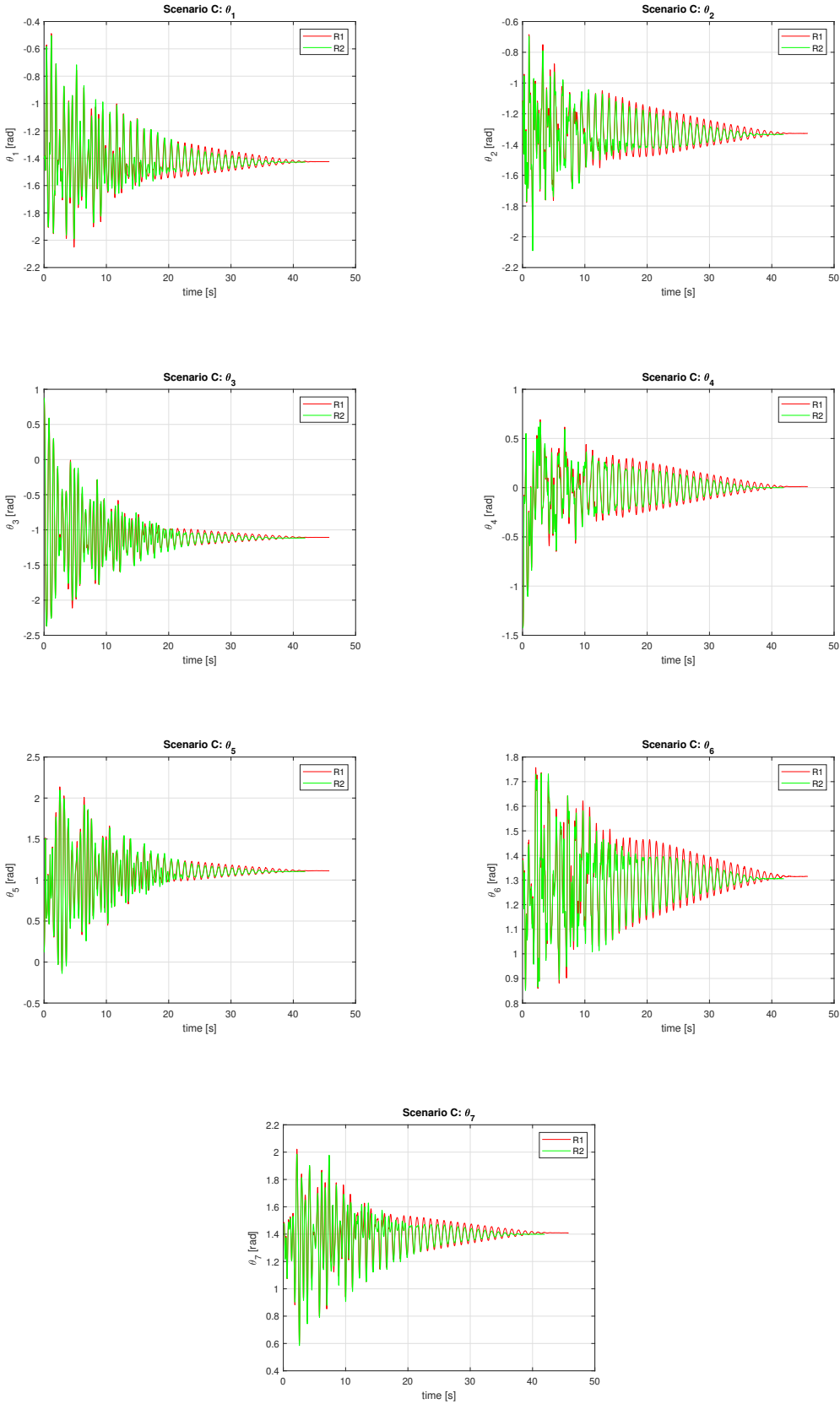
Figure E.5: A plot for every angle of the model dropper over time for scenario C, comparing the angles of the first and second run.

E.4.3. Comparison Run with Simulation

Run 2 for scenario C is compared with the results from the 2D model which reconstructed scenario C. The damping coefficients as determined in chapter 8 are applied.
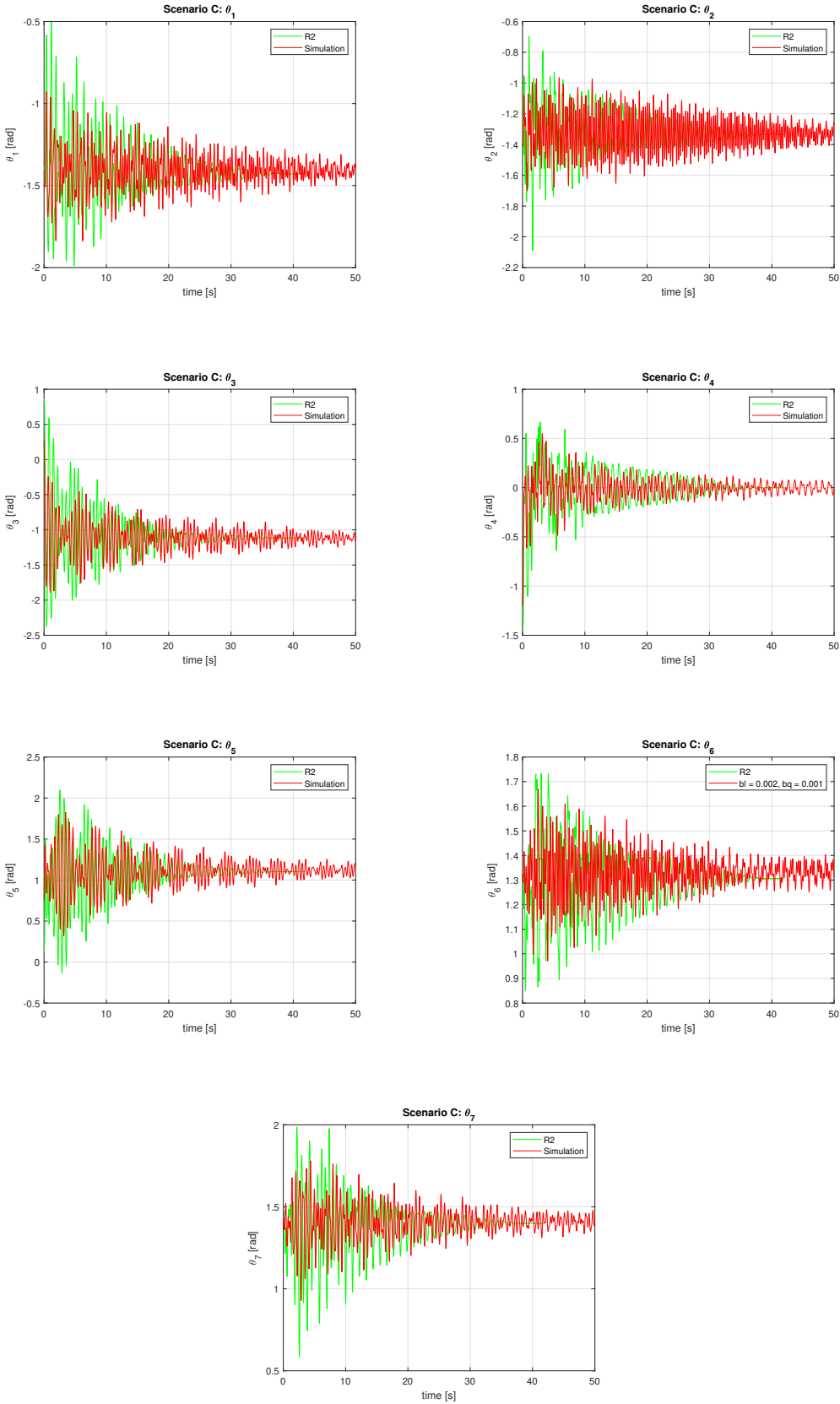
Figure E.6: A plot for every angle of the model dropper over time for scenario C run 2 compared with the results form the 2D simulation with damping coefficients $b_l = 0.002$ kg/s and $b_q = 0.001$ kg.

F

Phase Space Plots

In this appendix the phase space plots for each polar and azimuth angle for the 2D and 3D simulation with and without damping are provided.

F.1. Phase Space Plots for 2D Simulation of scenario A
F.1.1. No damping
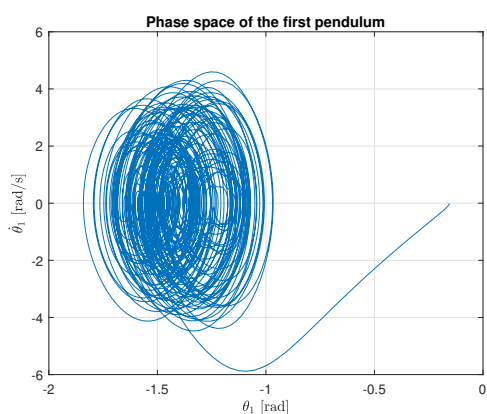
(a) Phase space plot of the polar angle of the first pendulum for the simulation without damping.
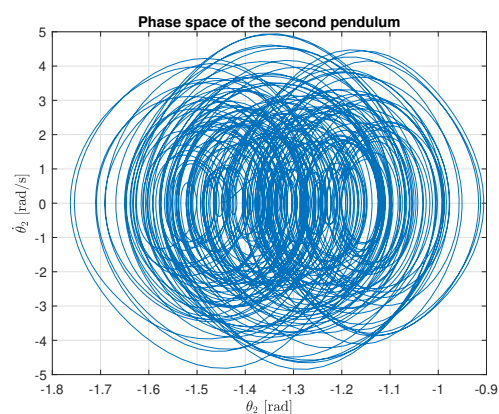
(b) Phase space plot of the polar angle of the second pendulum for the simulation without damping.
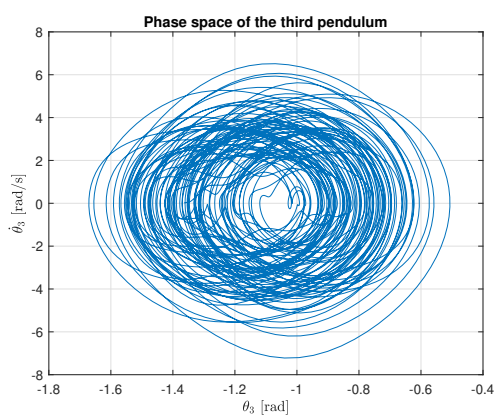
(c) Phase space plot of the polar angle of the third pendulum for the simulation without damping.
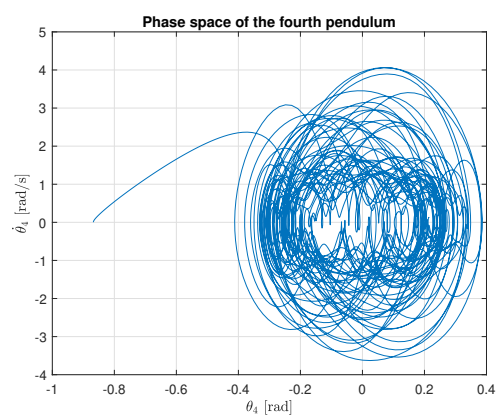
(d) Phase space plot of the polar angle of the fourth pendulum for the simulation without damping.
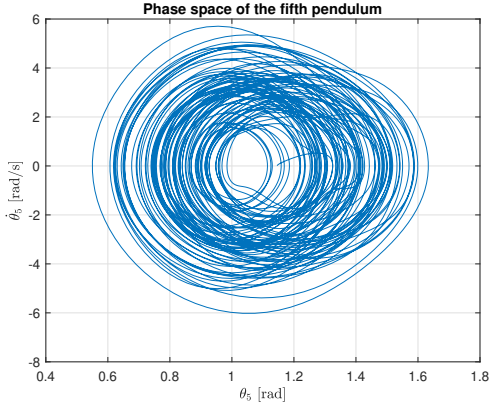
(e) Phase space plot of the polar angle of the fifth pendulum for the simulation without damping.
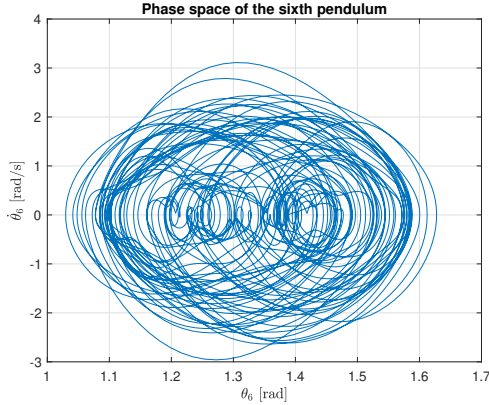
(f) Phase space plot of the polar angle of the sixth pendulum for the simulation without damping.
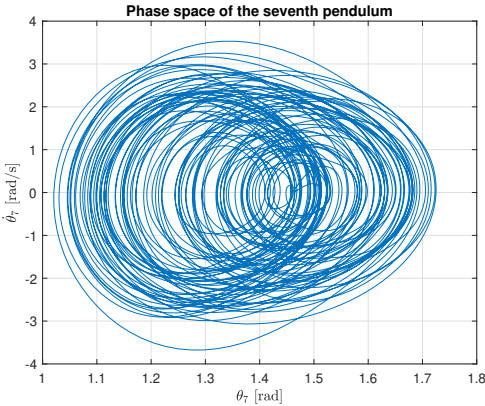
(g) Phase space plot of the polar angle of the seventh pendulum for the simulation without damping.

F.1.2. With Damping
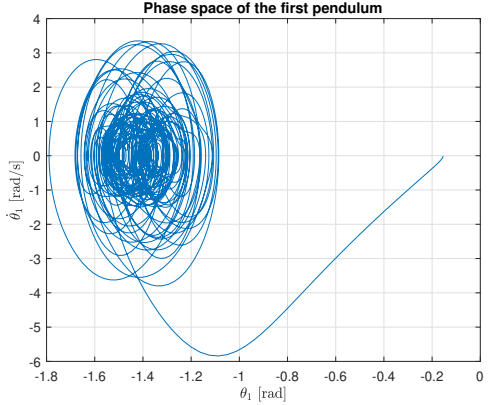
(a) Phase space plot of the polar angle of the first pendulum for the simulation with damping.
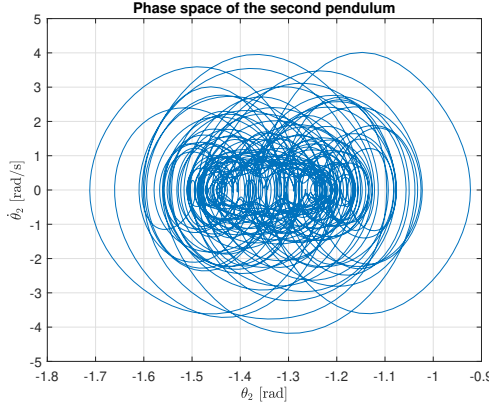
(b) Phase space plot of the polar angle of the second pendulum for the simulation with damping.
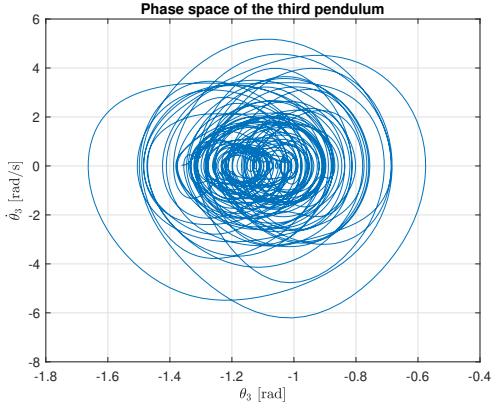
(c) Phase space plot of the polar angle of the third pendulum for the simulation with damping.
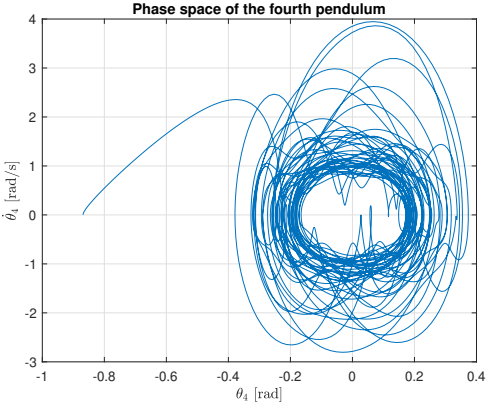
(d) Phase space plot of the polar angle of the fourth pendulum for the simulation with damping.
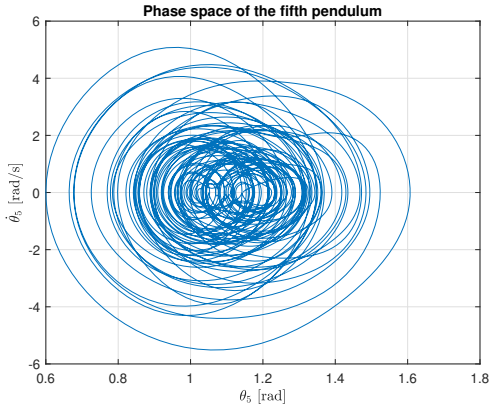
(e) Phase space plot of the polar angle of the fifth pendulum for the simulation with damping.
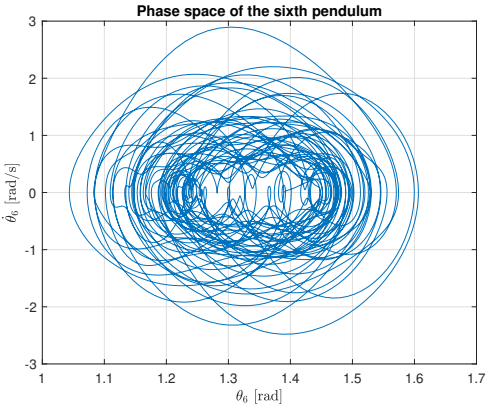
(f) Phase space plot of the polar angle of the sixth pendulum for the simulation with damping.
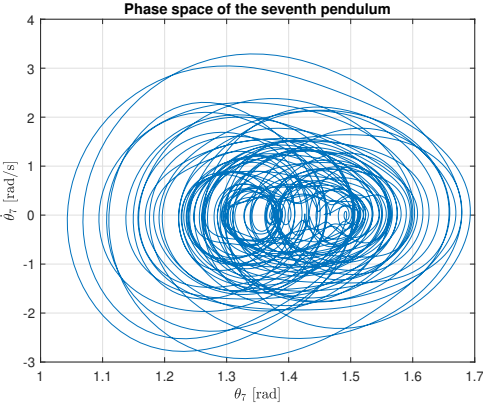
(g) Phase space plot of the polar angle of the seventh pendulum for the simulation with damping.

G

Wave Characteristics

T_i	ζ_i	ϵ_i
2.094	0.010	5.905
2.101	0.010	0.749
2.108	0.010	1.999
2.116	0.010	1.664
2.123	0.010	5.466
2.130	0.010	3.398
2.137	0.010	3.658
2.144	0.010	3.854
2.152	0.010	1.611
2.159	0.010	5.233
2.167	0.011	5.290
2.174	0.011	2.615
2.182	0.011	4.160
2.189	0.011	2.200
2.197	0.011	4.840
2.205	0.011	4.159
2.212	0.011	2.882
2.220	0.011	2.828
2.228	0.011	3.816
2.236	0.011	0.750
2.244	0.012	1.484
2.252	0.012	4.457
2.260	0.012	1.313
2.268	0.012	5.939
2.277	0.012	3.995
2.285	0.012	4.266
2.293	0.012	4.069
2.302	0.012	4.049
2.310	0.012	2.675
2.319	0.013	3.434
2.327	0.013	4.294
2.336	0.013	3.620
2.344	0.013	0.572
2.353	0.013	1.806
2.362	0.013	1.185
2.371	0.013	4.810
2.380	0.013	1.691
2.389	0.013	5.764
2.398	0.013	1.526
2.407	0.013	4.640
2.417	0.013	1.205
2.426	0.014	3.816
2.435	0.014	2.143
2.445	0.014	0.960
2.454	0.014	2.975

**Figure G.1:** Part 1 of the table containing the wave characteristics used to simulate the 3D dropper in waves.

T_i	ζ_i	ϵ_i
2.464	0.014	4.535
2.474	0.014	1.105
2.483	0.015	0.225
2.493	0.015	2.962
2.503	0.015	4.931
2.513	0.015	2.026
2.523	0.015	4.839
2.534	0.015	2.896
2.544	0.015	2.666
2.554	0.016	2.906
2.565	0.016	0.007
2.575	0.016	5.755
2.586	0.016	2.430
2.596	0.016	3.784
2.607	0.016	0.042
2.618	0.016	4.243
2.629	0.016	4.904
2.640	0.016	2.164
2.651	0.017	5.305
2.662	0.017	4.196
2.674	0.017	1.408
2.685	0.017	1.601
2.697	0.017	0.427
2.708	0.017	4.368
2.720	0.017	4.221
2.732	0.018	1.816
2.744	0.018	4.248
2.756	0.018	1.512
2.768	0.018	6.017
2.780	0.018	4.007
2.793	0.019	5.929
2.805	0.019	3.255
2.818	0.019	5.500
2.830	0.019	2.874
2.843	0.019	3.312
2.856	0.020	2.765
2.869	0.020	1.766
2.882	0.020	0.965
2.895	0.020	1.674
2.909	0.020	0.571
2.922	0.021	2.661
2.936	0.021	4.893
2.950	0.021	3.839
2.964	0.021	0.664
2.978	0.021	2.043

Figure G.2: Part 2 of the table containing the wave characteristics used to simulate the 3D dropper in waves.

T_i	ζ_i	ϵ_i
2.992	0.022	3.338
3.006	0.022	6.086
3.021	0.022	4.514
3.035	0.022	5.152
3.050	0.022	2.561
3.065	0.023	4.112
3.080	0.023	3.336
3.095	0.023	2.008
3.110	0.023	0.432
3.126	0.023	0.211
3.142	0.024	4.012
3.157	0.024	4.398
3.173	0.024	4.373
3.189	0.025	2.959
3.206	0.025	3.761
3.222	0.025	0.592
3.239	0.026	2.657
3.256	0.026	1.123
3.272	0.026	1.015
3.290	0.026	1.965
3.307	0.027	2.672
3.324	0.027	0.141
3.342	0.027	3.734
3.360	0.028	1.638
3.378	0.028	5.138
3.396	0.028	5.527
3.415	0.029	5.695
3.433	0.029	0.677
3.452	0.030	3.670
3.471	0.030	2.161
3.491	0.030	4.588
3.510	0.031	6.174
3.530	0.031	5.180
3.550	0.032	1.667
3.570	0.032	3.877
3.590	0.032	1.825
3.611	0.033	1.582
3.632	0.033	3.663
3.653	0.034	2.417
3.674	0.034	1.421
3.696	0.035	3.704
3.718	0.035	0.758
3.740	0.036	3.029
3.762	0.036	2.691
3.785	0.037	1.200

Figure G.3: Part 3 of the table containing the wave characteristics used to simulate the 3D dropper in waves.

T_i	ζ_i	ϵ_i
3.808	0.037	2.364
3.831	0.038	4.051
3.855	0.038	5.375
3.879	0.039	0.983
3.903	0.039	6.168
3.927	0.040	2.895
3.952	0.040	2.318
3.977	0.041	1.197
4.002	0.041	4.205
4.028	0.042	5.541
4.054	0.043	3.526
4.080	0.043	0.205
4.107	0.044	1.075
4.134	0.045	6.277
4.161	0.045	0.804
4.189	0.046	1.119
4.217	0.047	4.188
4.245	0.047	4.386
4.274	0.048	3.387
4.304	0.049	4.187
4.333	0.049	4.405
4.363	0.050	1.894
4.394	0.050	6.177
4.425	0.051	2.625
4.456	0.052	5.923
4.488	0.053	3.442
4.520	0.053	2.657
4.553	0.054	1.691
4.586	0.055	4.636
4.620	0.056	0.331
4.654	0.057	5.783
4.689	0.058	5.979

Figure G.4: Part 4 of the table containing the wave characteristics used to simulate the 3D dropper in waves.

T_i	ζ_i	ϵ_i
4.724	0.059	2.133
4.760	0.060	3.077
4.796	0.061	1.245
4.833	0.062	2.340
4.871	0.063	0.667
4.909	0.064	1.050
4.947	0.065	6.183
4.987	0.066	0.097
5.027	0.067	2.712
5.067	0.068	1.835
5.108	0.069	3.946
5.150	0.070	4.127
5.193	0.071	2.619
5.236	0.072	3.088
5.280	0.073	0.602
5.324	0.074	1.781
5.369	0.075	0.835
5.415	0.076	1.186
5.462	0.077	0.897
5.510	0.078	1.234
5.559	0.079	2.732
5.609	0.080	0.179
5.660	0.081	2.416
5.712	0.083	1.675
5.765	0.084	1.158
5.820	0.085	0.447
5.875	0.086	1.728
5.932	0.087	0.916
5.990	0.089	0.049
6.050	0.090	0.870
6.111	0.091	1.393
6.174	0.092	1.158

Figure G.5: Part 5 of the table containing the wave characteristics used to simulate the 3D dropper in waves.

T_i	ζ_i	ϵ_i
6.238	0.093	2.480
6.304	0.095	0.693
6.371	0.096	0.237
6.440	0.097	0.612
6.510	0.099	1.262
6.583	0.100	0.380
6.658	0.102	0.438
6.735	0.104	1.055
6.814	0.105	0.529
6.895	0.107	1.335
6.978	0.109	1.564
7.064	0.111	0.425
7.153	0.113	0.508
7.245	0.115	0.723
7.340	0.117	0.871
7.439	0.119	0.983
7.541	0.122	0.598
7.647	0.124	1.108
7.757	0.126	1.264
7.873	0.129	0.220
7.994	0.131	0.814
8.121	0.134	1.509
8.256	0.137	0.447
8.401	0.139	1.479
8.558	0.143	0.303
8.732	0.146	0.288
8.930	0.150	0.918
9.164	0.154	0.374
9.456	0.159	0.731
9.874	0.165	0.611
10.592	0.171	0.165
12.135	0.181	0.137

Figure G.6: Part 6 of the table containing the wave characteristics used to simulate the 3D dropper in waves.

G.1. Plots for the response of the mussel dropper
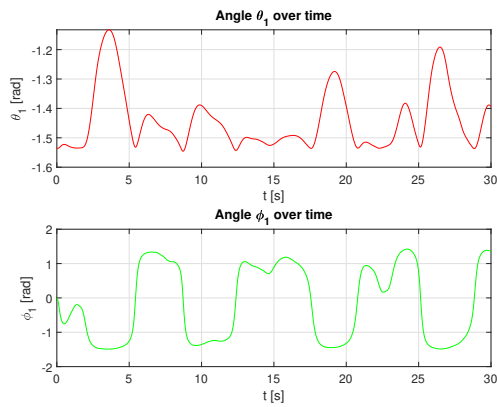
(a) A plot of the polar angle (top figure) and the azimuth angle (bottom figure) of the first pendulum in the 3D mussel dropper over the simulated period of time.
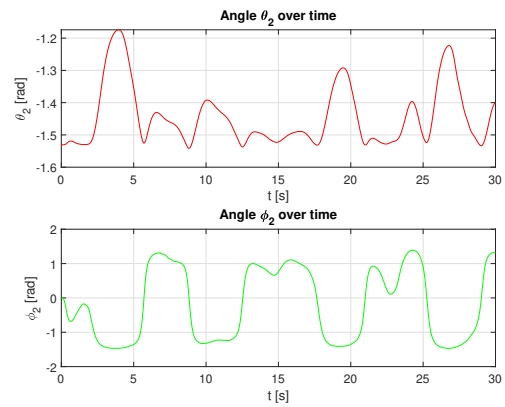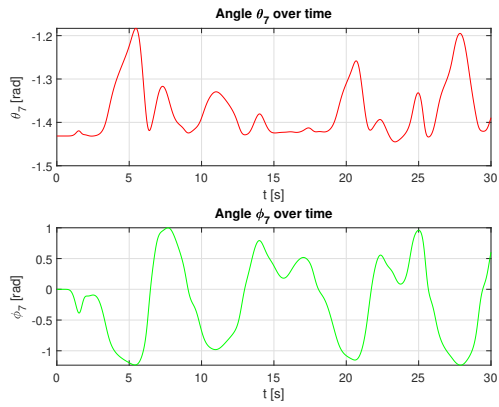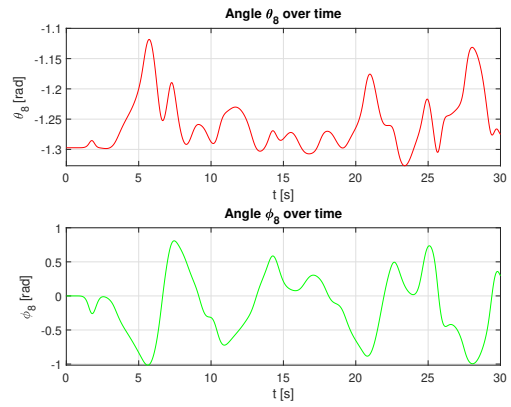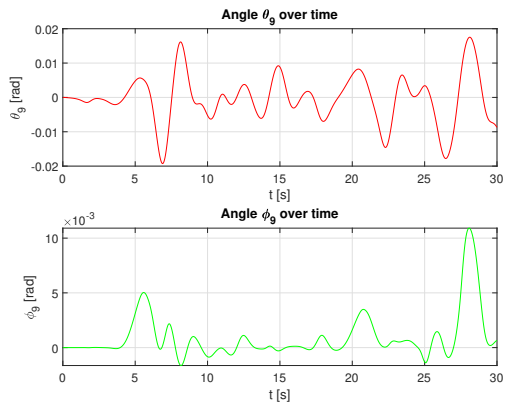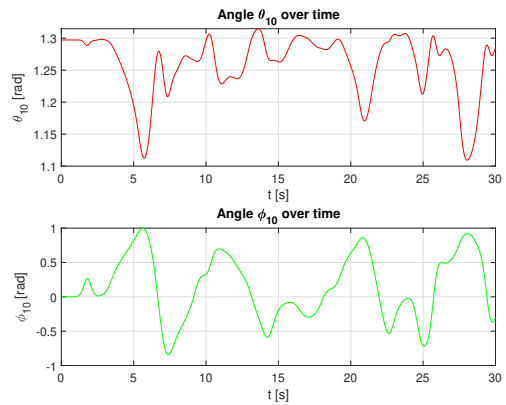
(b) A plot of the polar angle (top figure) and the azimuth angle (bottom figure) of the second pendulum in the 3D mussel dropper over the simulated period of time.
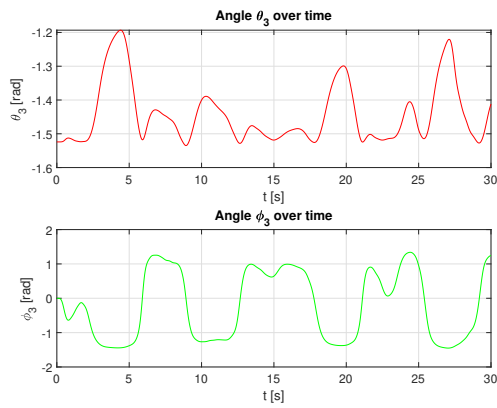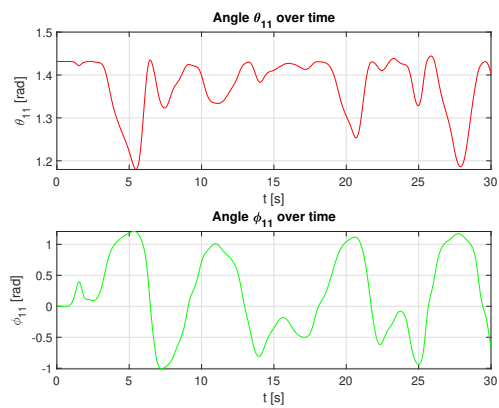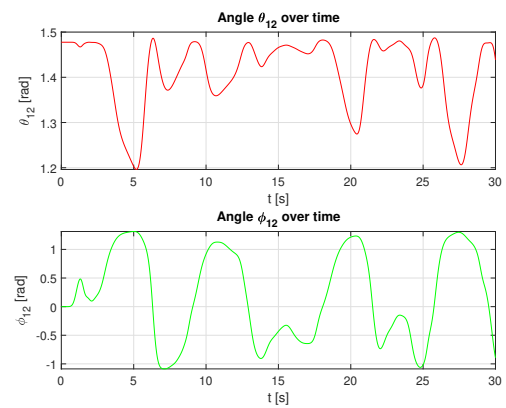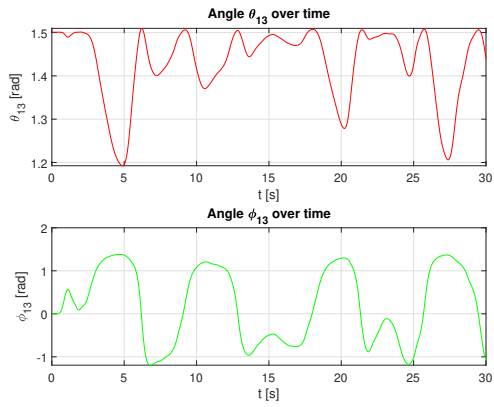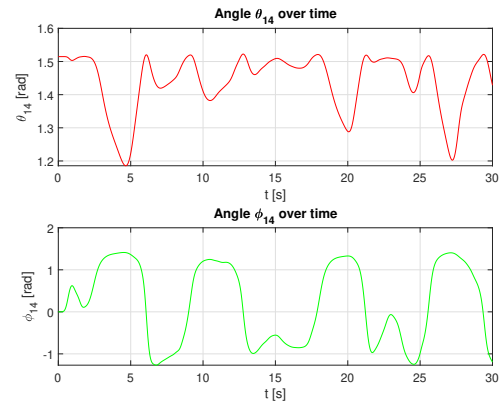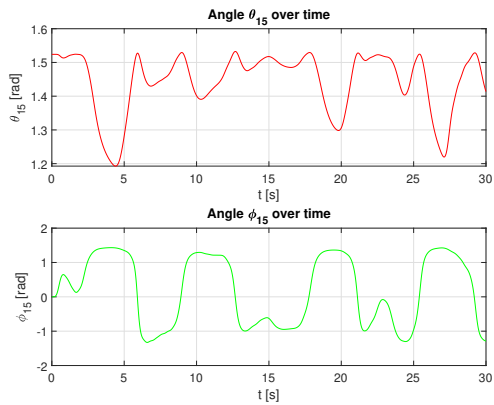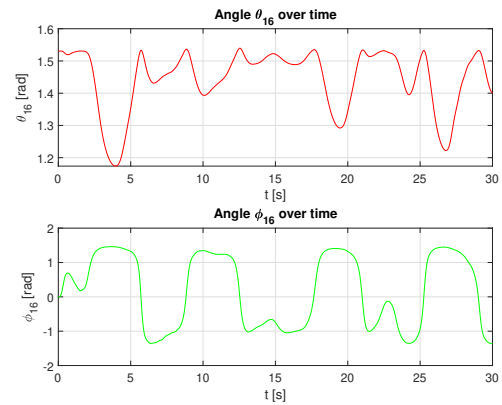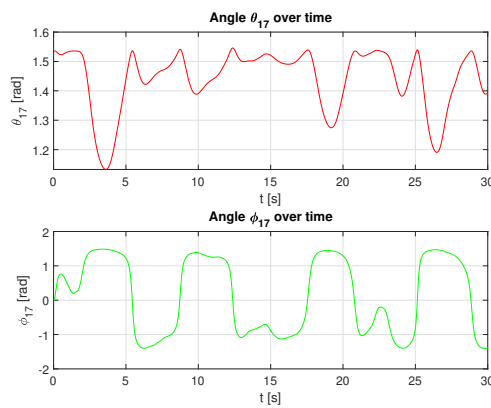
(c) A plot of the polar angle (top figure) and the azimuth angle (bottom figure) of the third pendulum in the 3D mussel dropper over the simulated period of time.
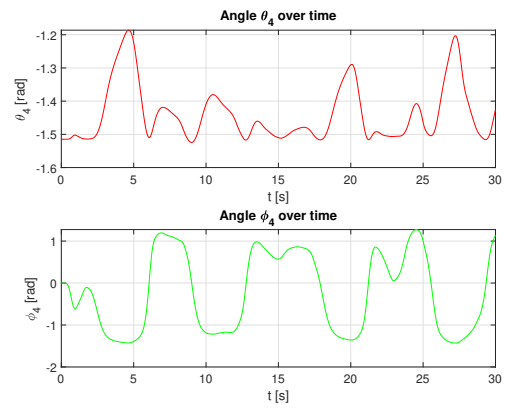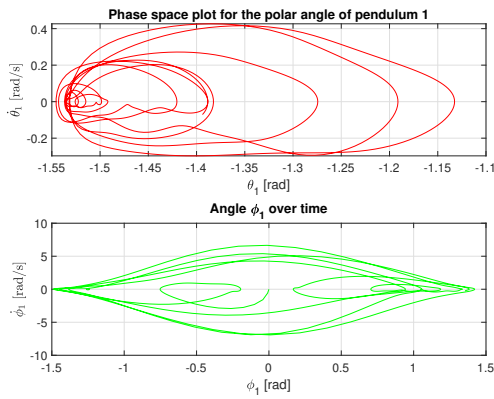
(d) A plot of the polar angle (top figure) and the azimuth angle (bottom figure) of the fourth pendulum in the 3D mussel dropper over the simulated period of time.
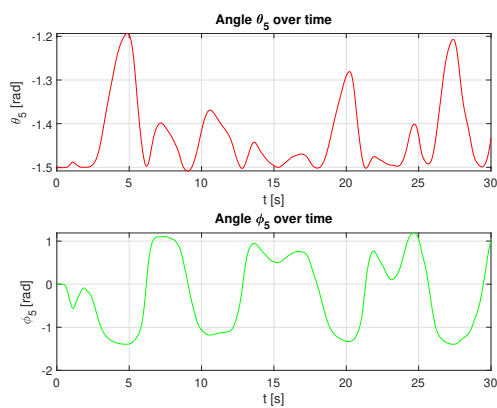
(e) A plot of the polar angle (top figure) and the azimuth angle (bottom figure) of the fifth pendulum in the 3D mussel dropper over the simulated period of time.
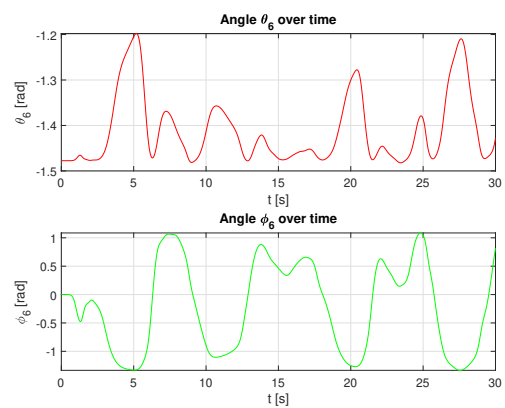
(f) A plot of the polar angle (top figure) and the azimuth angle (bottom figure) of the sixth pendulum in the 3D mussel dropper over the simulated period of time.

(g) A plot of the polar angle (top figure) and the azimuth angle (bottom figure) of the seventh pendulum in the 3D mussel dropper over the simulated period of time.
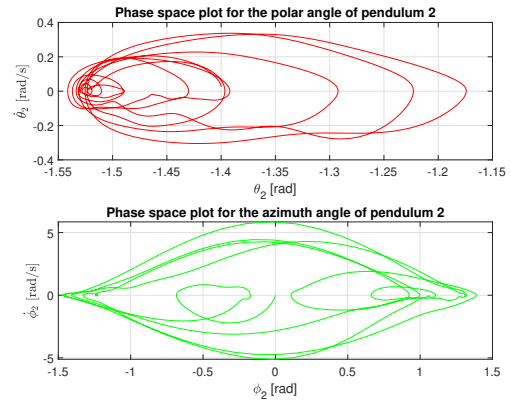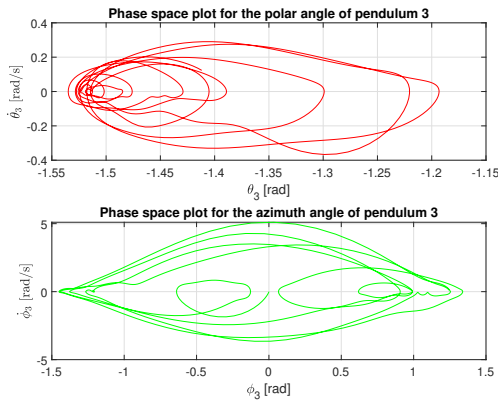
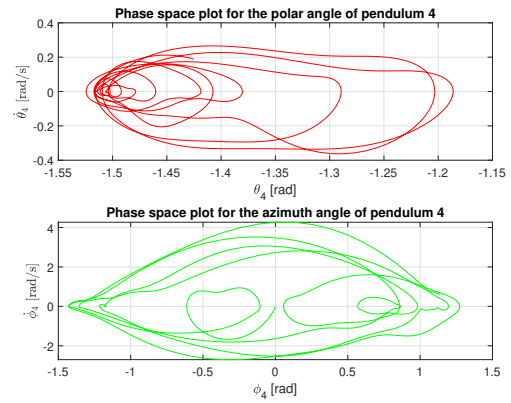**(h)** A plot of the polar angle (top figure) and the azimuth angle (bottom figure) of the eighth pendulum in the 3D mussel dropper over the simulated period of time.

(i) A plot of the polar angle (top figure) and the azimuth angle (bottom figure) of the ninth pendulum in the 3D mussel dropper over the simulated period of time.
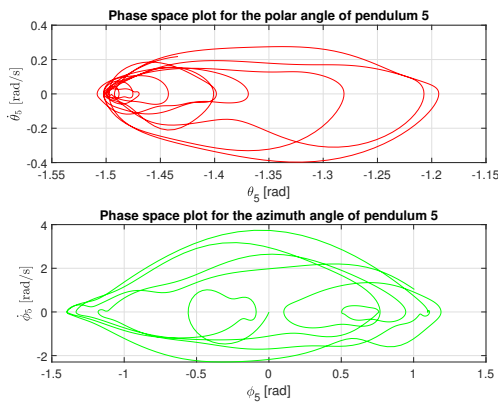
(j) A plot of the polar angle (top figure) and the azimuth angle (bottom figure) of the tenth pendulum in the 3D mussel dropper over the simulated period of time.

(k) A plot of the polar angle (top figure) and the azimuth angle (bottom figure) of the eleventh pendulum in the 3D mussel dropper over the simulated period of time.

(l) A plot of the polar angle (top figure) and the azimuth angle (bottom figure) of the twelfth pendulum in the 3D mussel dropper over the simulated period of time.

(m) A plot of the polar angle (top figure) and the azimuth angle (bottom figure) of the thirteenth pendulum in the 3D mussel dropper over the simulated period of time.
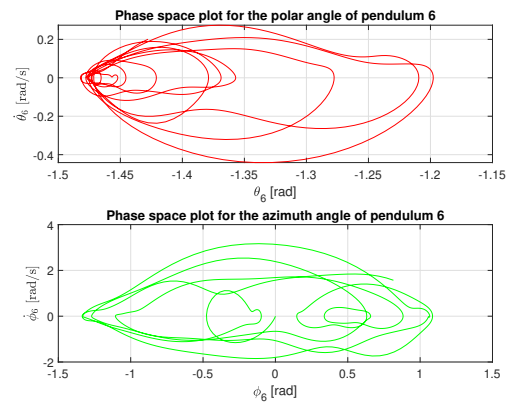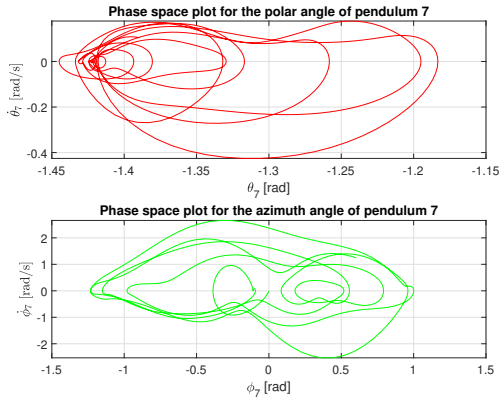
(n) A plot of the polar angle (top figure) and the azimuth angle (bottom figure) of the fourteenth pendulum in the 3D mussel dropper over the simulated period of time.

(o) A plot of the polar angle (top figure) and the azimuth angle (bottom figure) of the fifteenth pendulum in the 3D mussel dropper over the simulated period of time.

(p) A plot of the polar angle (top figure) and the azimuth angle (bottom figure) of the sixteenth pendulum in the 3D mussel dropper over the simulated period of time.

(q) A plot of the polar angle (top figure) and the azimuth angle (bottom figure) of the seventeenth pendulum in the 3D mussel dropper over the simulated period of time.
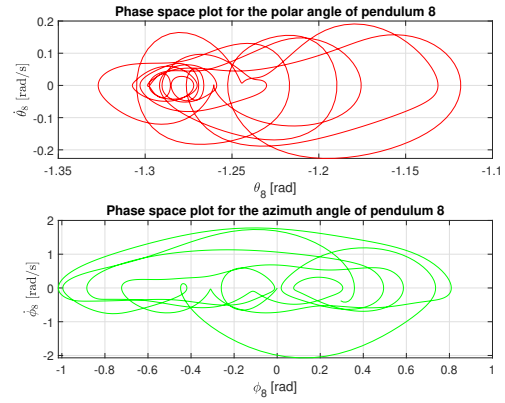
G.2. Phase space plots for the mussel dropper

(a) A phase space plot of the polar angle (top figure) and the azimuth angle (bottom figure) of the first pendulum in the 3D mussel dropper over the simulated period of time.
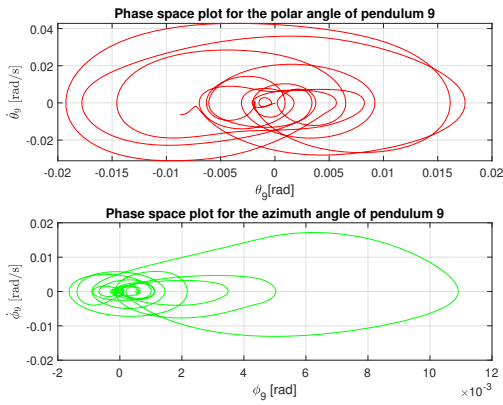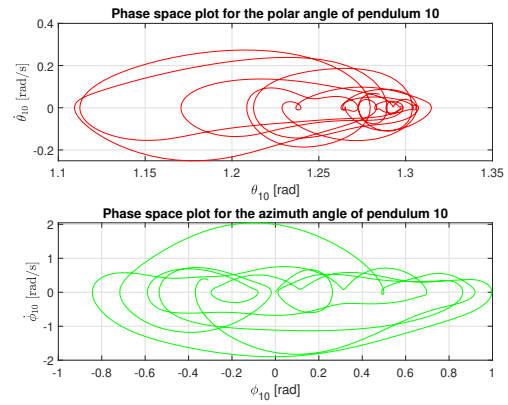

(b) A phase space plot of the polar angle (top figure) and the azimuth angle (bottom figure) of the second pendulum in the 3D mussel dropper over the simulated period of time.

(c) A phase space plot of the polar angle (top figure) and the azimuth angle (bottom figure) of the third pendulum in the 3D mussel dropper over the simulated period of time.

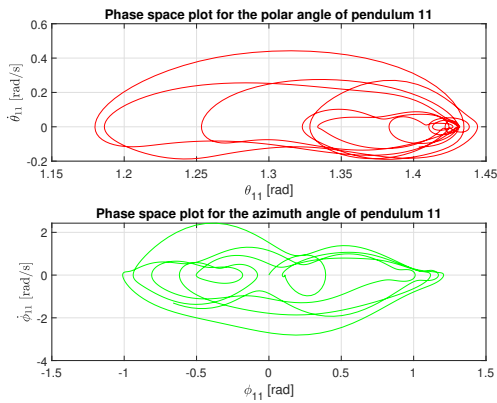

(d) A phase space plot of the polar angle (top figure) and the azimuth angle (bottom figure) of the fourth pendulum in the 3D mussel dropper over the simulated period of time.

(e) A phase space plot of the polar angle (top figure) and the azimuth angle (bottom figure) of the fifth pendulum in the 3D mussel dropper over the simulated period of time.
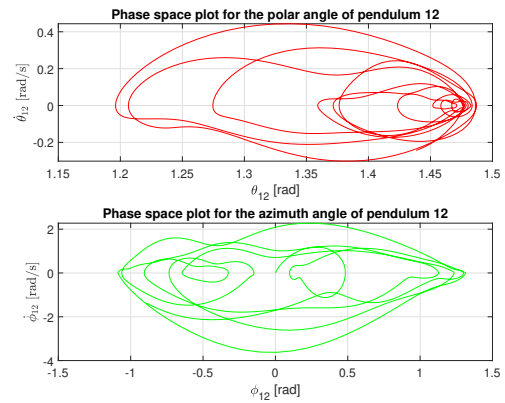

(f) A phase space plot of the polar angle (top figure) and the azimuth angle (bottom figure) of the sixth pendulum in the 3D mussel dropper over the simulated period of time.
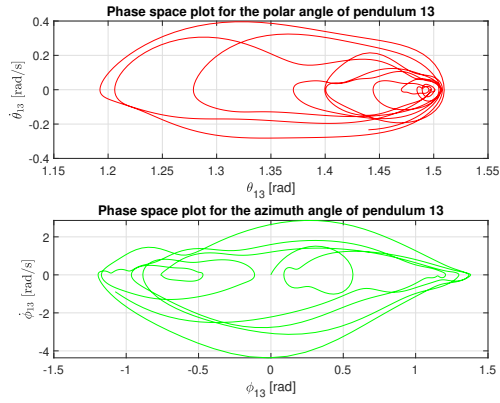
(g) A phase space plot of the polar angle (top figure) and the azimuth angle (bottom figure) of the seventh pendulum in the 3D mussel dropper over the simulated period of time.

(h) A phase space plot of the polar angle (top figure) and the azimuth angle (bottom figure) of the eighth pendulum in the 3D mussel dropper over the simulated period of time.

(i) A phase space plot of the polar angle (top figure) and the azimuth angle (bottom figure) of the ninth pendulum in the 3D mussel dropper over the simulated period of time.

(j) A phase space plot of the polar angle (top figure) and the azimuth angle (bottom figure) of the tenth pendulum in the 3D mussel dropper over the simulated period of time.
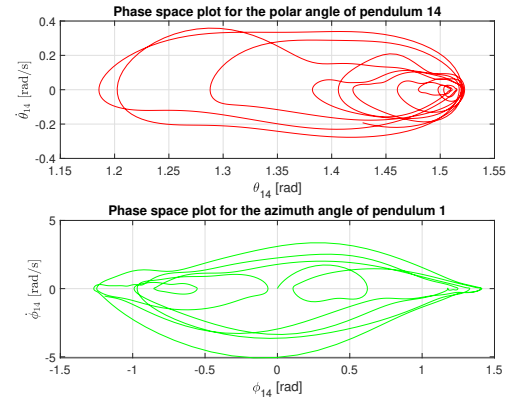
(k) A phase space plot of the polar angle (top figure) and the azimuth angle (bottom figure) of the eleventh pendulum in the 3D mussel dropper over the simulated period of time.
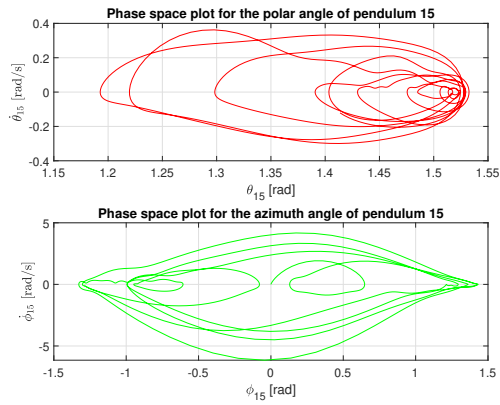
(l) A phase space plot of the polar angle (top figure) and the azimuth angle (bottom figure) of the twelfth pendulum in the 3D mussel dropper over the simulated period of time.
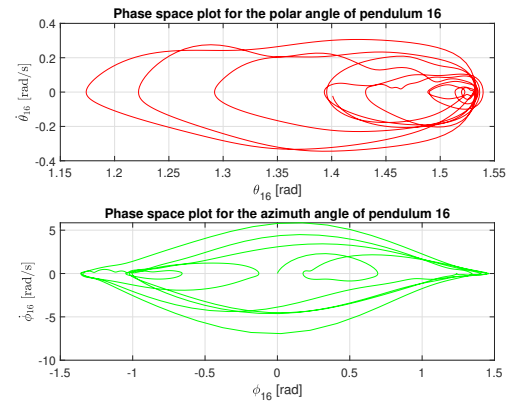
(m) A phase space plot of the polar angle (top figure) and the azimuth angle (bottom figure) of the thirteenth pendulum in the 3D mussel dropper over the simulated period of time.
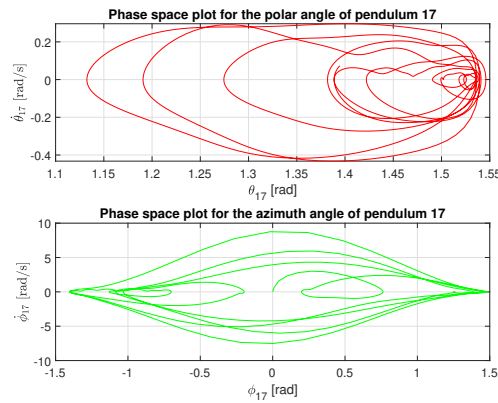
(n) A phase space plot of the polar angle (top figure) and the azimuth angle (bottom figure) of the fourteenth pendulum in the 3D mussel dropper over the simulated period of time.

(o) A phase space plot of the polar angle (top figure) and the azimuth angle (bottom figure) of the fifteenth pendulum in the 3D mussel dropper over the simulated period of time.

(p) A phase space plot of the polar angle (top figure) and the azimuth angle (bottom figure) of the sixteenth pendulum in the 3D mussel dropper over the simulated period of time.

(q) A phase space plot of the polar angle (top figure) and the azimuth angle (bottom figure) of the seventeenth pendulum in the 3D mussel dropper over the simulated period of time.